CZECH TECHNICAL UNIVERSITY IN
PRAGUE

Faculty of Nuclear Sciences and Physical
Engineering

Department of Physics

Diploma thesis

Study of jet production in Au+Au collisions in the STAR experiment

Bc. Martin Kocmánek

Supervisor: RNDr. Jana Bielčíková, Ph.D.

Consultant: Ing. Jan Rusňák

Prague, 2017

ČESKÉ VYSOKÉ UČENÍ TECHNICKÉ
V PRAZE

Fakulta Jaderná a Fyzikálně Inženýrská

Katedra Fyziky

Diplomová práce

Studium produkce jetů v Au+Au srážkách v experimentu STAR

Bc. Martin Kocmánek

Školitel: RNDr. Jana Bielčíková, Ph.D.

Konzultant: Ing. Jan Rusňák

Praha, 2017

NASCANOVAT PODEPSANE ZADANI A
ULOZIT DO DVOU EPS SOUBORU
ZADANI1.EPS a ZADANI2.EPS

NASCANOVAT PODEPSANE ZADANI A
ULOZIT DO DVOU EPS SOUBORU
ZADANI1.EPS a ZADANI2.EPS

Prohlášení:

Prohlašuji, že jsem svou diplomovou práci vypracoval samostatně a použil jsem pouze podklady (literaturu, software, atd.) uvedené v přiloženém seznamu.

Nemám závažný důvod proti užití tohoto školního díla ve smyslu 60 Zákona .121/2000 Sb., o právu autorském, o právech souvisejících s právem autorským a o změně některých zákonů (autorský zákon).

V Praze dne

Title:
Study of jet production in Au+Au collisions in the STAR experiment

Author: Bc. Martin Kocmánek

Specialization: Experimental nuclear and particle physics

Sort of project: Diploma thesis

Supervisor: RNDr. Jana Bielčíková, Ph.D.
                  Nuclear Physics Institute, Czech Academy of Sciences

Consultant: Ing. Jan Rusňák, Ph.D.
                  Nuclear Physics Institute, Czech Academy of Sciences

Abstract: Ultra-relativistic heavy-ion collisions enable us to create the quark-gluon plasma, extremely hot and dense strongly interacting matter predicted by the QCD. During hard scattering, partons of incoming nuclei undergo fragmentation and hadronisation which results in jets, collimated sprays of hadrons. Due to interaction of hard partons with QGP, the energy of partons is reduced in comparison with p+p collisions. This phenomenon is referred to as a jet quenching and provides important information about properties of nuclear matter. This diploma thesis presents the analysis of charged and fully reconstructed jets produced in Au+Au collisions at $\sqrt{s_{NN}}=$ 200 GeV from the 2014 RHIC run recorded by the STAR detector. The anti-k_T jet algorithm was applied on data as a function of centrality, the resolution parameter R and cut on p_T of the leading hadron in the jet. Charged jet spectra presented with the estimate of systematic uncertainties were corrected by the Bayesian unfolding utilizing the response matrix that contains information about fluctuating background and detector effects.

Key words: quark-gluon plasma, jet, jet algorithm, STAR experiment

Názov práce:

Štúdium produkcie jetov v Au+Au zrážkach v experimente STAR

Autor: Bc. Martin Kocmánek

Špecializácia: Experimentálna jadrová a časticová fyzika

Druh práce: Diplomová práca

Školiteľ: RNDr. Jana Bielčíková, Ph.D.
        Ústav jaderné fyziky, Akademie věd České republiky

Konzultant: Ing. Jan Rusňák, Ph.D.
        Ústav jaderné fyziky, Akademie věd České republiky

Abstrakt: Ultra-relativistické zrážky ťažkých iónov umožňňujú vytvoriť kvark-gluónovú plazmu, extrémne horúcu a hustú silne interagujúcu hmotu. Počas tvrdého rozptylu zrážajúcich sa partónov v jadrách dochádza k ich fragmentácii a hadronizácii, čo vedie k tvorbe jetov, kolimovaných spŕšok hadrónov. Z dôvodu interakcie tvrdých partónov s kvark-gluónovou plazmou, energia partónov je v porovnaní s p+p zrážkami redukovaná. Tento jav sa nazýva zhášanie jetov a poskytuje dôležité informácie o jadrovej hmote.

Táto diplomová práca prezentuje analýzu nabitých a plne rekonštruovaných jetov produkovaných v Au+Au zrážkach pri energii $\sqrt{s_{NN}}$= 200 GeV zaznamenaných v roku 2014 na urýchľovači RHIC experimentom STAR. Anti-k_T jetový algoritmus bol aplikovaný na dáta ako funkcia centrality zrážky ako aj rozlišovacieho parametru R a hodnoty hybnosti p_T na vedúci hadrón v jete. Nabité spektrá jetov, prezentované spolu s odhadom systematických chýb, boli korigované Bayesovskou metódou dekonvolúcie, pričom sa využila matica odozvy, ktorá obsahuje informáciu o fluktujúcom pozadí a efektoch detektora.

Kľúčové slová: quark-gluónová plazma, jet, jetový algoritmus, experiment STAR

Acknowledgement

Contents

List of Figures

List of Tables

Preface

Currently one of the hottest topics in the field of high-energy physics is the study of a new state of strongly interacting matter, referred to as a quark-gluon plasma (QGP). QGP is a hot and dense nuclear matter, consisting of deconfined partons (quarks and gluons) and it is expected to be formed at the initial stage of heavy-ion collisions at the ultra-relativistic energies. A heavy-ion collision is a dynamical process with large energy transfer which lasts only few femtoseconds. QGP is theoretically predicted by Quantum Chromodynamics and exists only at extremely high temperature and density. Such conditions are achieved at experiments at Relativistic Heavy Ion Collider (RHIC) at Brookhaven National Laboratory and at the Large Hadron Collider (LHC) at CERN.

During early hard scattering, partons of incoming nuclei undergo fragmentation and hadronization which results in jets, collimated sprays of hadrons. Due to interaction of hard partons with surrounding medium, the energy of partons is reduced in comparison to elementary proton-proton collisions that is referred to as a jet quenching. Jet quenching is a unique tool to study QGP, because measurement of modifications of jets traversing the nuclear matter provides important information on properties of hot and dense nuclear matter.

Presented thesis deals with the topic of jet production in heavy-ion collisions and jet reconstruction using modern sequential recombination algorithms. The main aim of the thesis is the reconstruction of full and charged jet spectra and correction of charged jet spectra on fluctuating background and detector effects. The first chapter of this work gives a brief introduction to the physics of heavy-ion collisions. This part that is focused on quark gluon plasma, shortly describes phase diagram of nuclear matter, time evolution of QGP in heavy-ion collision and some of the most important signatures of QGP such as suppression of high p_T particles, elliptic flow, strangeness enhancement, quarkonia suppression, etc.

The STAR experiment located at RHIC, dedicated to study behavior and properties of the strongly interacting nuclear matter is described in the Chapter 2. The STAR detector consists of several different types of detection subsystems that are responsible for measuring and identifying products of the collision.

The third chapter is dedicated to jet physics, jet algorithms and briefly summarizes some results from measurements of spectra of charged and fully reconstructed jets and jet nuclear modification factor R_{AA} in $\sqrt{s_{NN}} = 200$ GeV in Au+Au collisions at STAR or in $\sqrt{s_{NN}} = 2.76$ TeV Pb+Pb collisions at ALICE. The first part of this chapter defines a jet and describes one of the most important probe of QGP jet quenching. This is followed by presentation of jet algorithms and their properties and tools for jet analysis.

The main results of this work, whose topic is reconstruction of charged and fully reconstructed jet spectra in Au+Au collisions at $\sqrt{s_{NN}} = 200$ GeV collected in RHIC Run 14 by the STAR detector are presented in the last 4th Chapter. First of all, suitable events and tracks are selected and study of data quality assurance of towers, response of the BEMC and its time stability is performed. This is followed by application of the anti-k_T jet algorithm as a function of centrality as well as the resolution parameter R and cut on p_T of the leading hadron in jet to reconstruct full and charged jet spectra. Jet spectra are corrected on estimated mean background energy density and reasonable jet area cut. Obtained charged jet spectra are corrected by the Bayesian unfolding. Unfolding process utilizes response matrix containing informations about detector effects and fluctuating background that was determined by embedding of single particles into real events. This chapter concludes with resulting unfolded charged jet spectra with the first estimation of systematic uncertainties.

Chapter 1

Physics of high energy nucleus collisions

In modern nuclear and particle physics, many experiments focus on the research of basic structure of matter and forces between elementary particles. The long-lasting effort of scientists to describe and understand fundamental constituents lead to the formulation of the Standard model, whose current formulation was developed in 1970s by three physicists: Sheldon Glashow, Steven Weinberg and Abdus Salam. The Standard model is a quantum field theory that incorporates current theoretical knowledge of all known elementary particles and it is able to describe three from four fundamental interactions except gravitational: weak, strong and electro-magnetic.

A theory describing interaction that is responsible for binding quarks and gluons in hadrons and protons and neutrons in nucleus is Quantum Chromodynamics (QCD) formulated within the Standard Model. QCD is a non-Abelian gauge theory of the strong interactions with symmetry group SU(3).

The strong interaction between quarks and anti-quarks is mediated by gluons. The key property of the strong interaction is color that is the QCD analog of the electric charge in quantum electrodynamics. The color charge is carried by all fundamental particles in the strong interaction and each of them can carry one of three color charges: red, green, blue or their conjugate anticolors. Quarks are constituent particles from which composite particles such as color-neutral hadrons are formed. Hadrons are divided into two groups according to number of constituents: mesons consisting of a pair of quark-antiquark (pion) and baryons consisting of three quarks or antiquarks.

The strength of the strong interaction is governed by the QCD coupling constant α_S:

$$\alpha_S \sim \frac{1}{\ln\left(\frac{Q^2}{\Lambda_{QCD}^2}\right)} \tag{1.1}$$

where Q is the momentum transfer in the interaction and Λ_{QCD} is the QCD scale. Figure 1.1 summarizes result of several measurement of the coupling constant.

At normal conditions that corresponds to $Q^2 \to 0$, quarks and gluons are very tightly bound in colorless hadronic matter. The potential $V(r)$ between quarks and
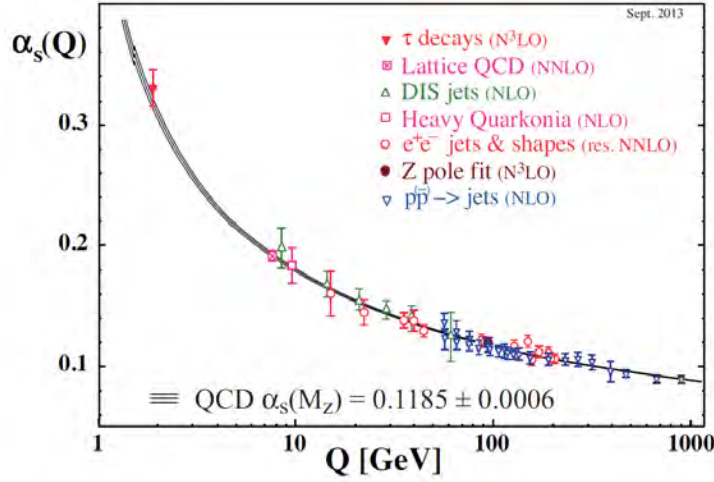
Figure 1.1: The overview of measurements of the coupling constant α_S as a function of the energy scale Q [1].

anti-quarks can be expressed as a function of their mutual distance r by:

$$V(r) = -\frac{4}{3}\frac{\alpha_S}{r} + kr \qquad (1.2)$$

where k is a string tension and it is an empirical value which represents the strength of quark confinement force. This formula shows, that the potential increases with increasing distance and it is impossible to separate quarks from each other, because when potential is high enough the hypothetical string between quarks breaks and a new quark-antiquark pair is created from the vacuum. Therefore it is not possible to observe free quarks. This feature of the QCD is referred to as a color confinement.

When momentum transfer Q^2 is increasing and distance between quarks is decreasing, the coupling constant α_S also decreases. It means that bond between quarks becomes asymptotically weaker and quarks behave almost as free particles. This phenomenon is referred to as an asymptotic freedom and it was described in 1970s by David Politzer, Frank Wilczek and David Gross.

1.1 Quark-gluon plasma

The quark-gluon plasma is a new state of hot and dense nuclear matter consisting of free partons - quarks and gluons. It is theoretically predicted from the asymptotic freedom concept that predicts transition from confined matter to matter with "free partons". QGP exists only at extreme high temperature T and baryonic density μ_B in the order of 10^{12} K and 10^{12} kg.cm^{-1} [2], when quarks and gluons are deconfined. Considering these conditions, QGP can be found in three places: in the first microseconds after the Big Bang, in the center of compact stars and finally in ultra-relativistic heavy-ion collisions.

Experiments at Relativistic Heavy Ion Collider (RHIC) at Brookhaven National Laboratory (BNL) and at the the Large Hadron Collider (LHC) at the European

Centre for Nuclear Research (CERN) are dedicated to achieve extreme conditions by collisions of accelerated heavy-ions to ultra-relativistic velocities very close to the speed of light in vacuum. The maximal collision energies of heavy ions $\sqrt{s_{NN}}$ that can be achieve by current accelerators are 5 TeV at the LHC and 200 GeV at RHIC. When the Lorentz contracted nuclei collide, they are almost immediately stopped that results in the release of enormous amount of energy and formation of a fireball - hot and dense nuclear matter. Immediately after the collision, the fireball starts to expand and new particles are produced which are eventually measured by detectors. The relativistic heavy-ion collision is a dynamic process with a typical size and time scale of the order of 10 fm and 10 fm/c. At these extremely high values of energy and nucleon densities, QGP is supposed to be formed.

Although first hints of a new state of strongly interacting matter were already observed at the Super Proton Synchrotron (SPS) at CERN in 2000, the first direct experimental evidence of QGP was observed at the Relativistic Heavy-Ion Collider (RHIC) at the BNL[3]. This result was later independently verified also by the Large Hadron Collider (LHC).

In Figure 1.2 we can see current understanding and theoretical expectations about the phase diagram of nuclear matter that is one of the main subjects of current research. The phase diagram describes phase transition between the state of ordinary hadronic matter and deconfined nuclear matter - QGP as a function of temperature T and baryon chemical potential μ_B. In the region of low T and μ_B, the matter is in a state of hadron gas. Low T and relatively high μ_B represent normal conditions, under which the matter is confined. By increasing T or μ_B, binding energy between quarks and gluons weakens, hadron gas transforms to deconfined nuclear matter QGP. The white curve symbolizes the first order phase transition. This curve ends at a specific point, referred to as a critical point. From this point the crossover region starts, where the phase of the second order transition occurs. The intensive search for the critical point is currently carried out in a dedicated Beam Energy Scan (BES) program at RHIC using measurements at different energies of Au+Au collisions. Similar experiments dedicated to the research of deconfned matter and the search of the critical point will be conducted in future experiments at FAIR (Facility for Antiproton and Ion Research) at GSI in Germany and NICA (Nuclotron-based Ion Collider fAcility) at JINR in Russia.

1.2 Space-time evolution of nuclear collision

Immediately after the ultra-relativistic heavy-ion collision (in the order of femtoseconds) the region of a fireball undergoes several different phases. These phases are not completely understood yet and they are of the main interest in current research. The space-time evolution of a nuclear collision from the initial to final stage is depicted in Figure 1.3 and can be described with the increasing time τ as follows:[2]

- $0 < \tau < \tau_0$
  The time $\tau = 0$ expresses the beginning of a collision. In the very first moments of a collision two colliding nuclei traverse each other, they release a large amount of energy and hard processes take place. Eventually these processes lead to production of high p_T particles, jets and heavy flavour - c and b quarks.
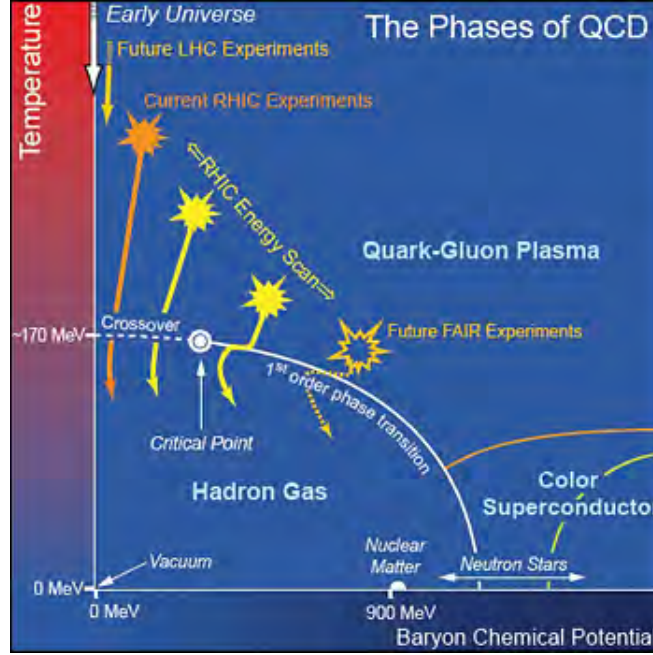
Figure 1.2: A schematic QCD phase diagram of nuclear matter [4].

Immediately after that the hot and dense medium of nuclear matter called fireball is formed. The stage of pre-equilibrium is achieved, when the partons are created. This system tends to the state of thermal equilibrium. The system expands promptly and the temperature and pressure are decreasing. At the time τ_0 the system might eventually reach thermal equilibrium. The duration of this process is estimated to be about $\tau = 1$ fm/c.

- $\tau_0 < \tau < \tau_f$
  If thermalization is fast enough, then hot and dense nuclear matter, eventually QGP is formed and it reaches a state of local equilibrium. By the stage of thermal equilibrium, the medium behaves as an ideal liquid and the theory of relativistic hydrodynamics can be used for describing this stage and its subsequent progress. After some time of progress of the medium the process of hadronization begins and the medium starts to convert to the hadron gas. Pressure gradients present in the medium cause expansion and decreasing of the system temperature.

- $\tau = \tau_f$
  Free quarks and gluons start to confine to hadrons. It happens at the time of τ_f, when the temperature of QGP falls to the critical value $T_f = 170$ MeV [5]. This effect is also called freeze-out and phase transition between QGP and hadronic matter occurs. There are two kinds of freeze-out: chemical, which comes first and occurs at a higher temperature than the later one, thermal freeze-out, which is also called kinetical freeze-out. During chemical freeze-out particles undergo mutual elastic collisions until the thermal freeze-out comes. In this stage, new particles are not produced anymore and their number stabilizes at

certain equilibrium with a constant baryochemic potential and temperature. Finally, when the thermal freeze-out takes place, particles fly away from the region of the collision, because the mean free path is increasing to the value when it is almost identical to the size of the system.

- $\tau_f < \tau$
  After the time τ_f evolution of the medium ends, decoupling starts, hadrons recede each other and leave the region of the collision.
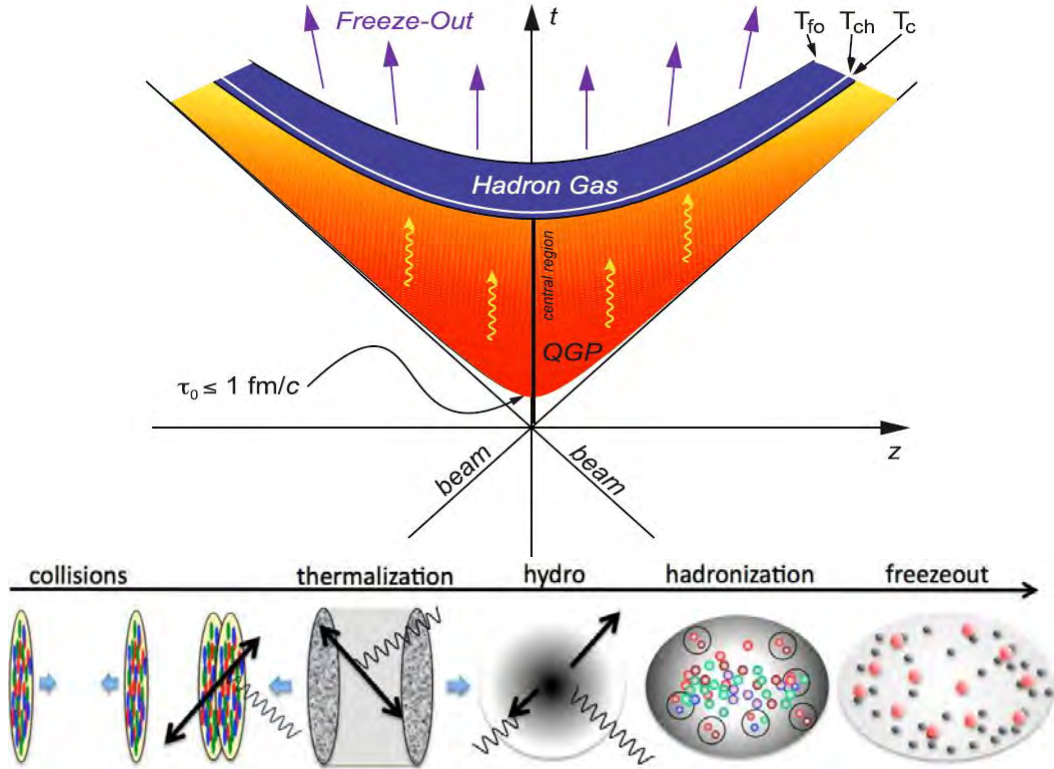
Figure 1.3: Space time evolution of a relativistic heavy-ion collision with the illustration of individual stages[4][6].

1.3 Geometry of nuclear collision

Centrality is a quantity that characterizes a collision of two nuclei and it is related to the impact parameter b. Impact parameter represents the minimal distance between centers of interacting nuclei in the transverse plane. It has a value from 0 to $R_1 + R_2$ [7], where R_1 and R_2 are radii of the colliding nuclei. According to the value of the impact parameter, collisions can be categorized to distant ($b > 2R$, where R is a radius of nucleus), peripheral ($b < 2R$) and central ($b \approx 0$), which illustrated by Figure 1.4. As the impact parameter decreases, colliding nuclei overlap more and consequently more nucleon-nucleon collisions happen. If a nucleon is involved in a collision with another one, it is referred to as a participant. Nucleons, which do not

participate in the collision are referred to as spectators and they continue in the longitudinal direction after the collision.

Centrality is connected with centrality classes that are defined as percentile of the total geometric cross section in the event according to the impact parameter. Common centrality classes, which are also depicted in Figure 1.5 are: 0-5% (the most central), 5-10% (central), 10-20% (semi-central), 20-40%(semi-peripheral), 40-80% (peripheral).

Experimentally, centrality of a heavy-ion collision or the impact parameter, cannot be measured directly. But the impact parameter is determined from the Glauber model (see next subsection) and transverse energy or the number of spectator nucleons (measured by "zero-degree calorimeter" ZDC) [5]. Centrality is calculated from particle multiplicity that represents a total number of produced particles. In the case of the central nucleus-nucleus collision with low impact parameter, more nucleons interact among themselves and more particles are produced, which means that multiplicity is higher. Moreover multiplicity is proportional to the energy released in the collision, if the energy of collision is higher then also multiplicity increases. The alternative definition of centrality and its relation to other variables e.g. multiplicity of particles is illustrated in Figure 1.5.
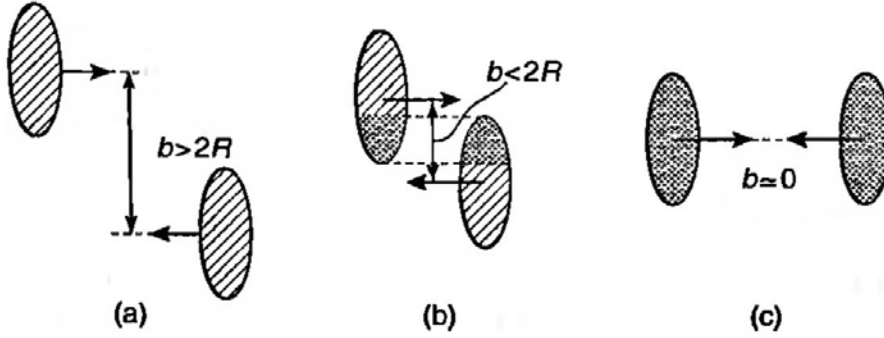
Figure 1.4: Geometry of a nuclear collision according to the value of the impact parameter: (a) - distant collision, (b) - peripheral collision and (c) - central collision. [2]

1.3.1 Glauber model

The Glauber model is used for description of a high-energy heavy-ion collision and calculation of basic variables of the collision such as the number of participant nucleons N_{part} and binary nucleon-nucleon collisions N_{coll} [9]. The Glauber model has two assumptions. The first is that nucleons travel in straight lines without any deflection after the collision. According to this, the Glauber model is a good approximation at very high energies. Secondly, inelastic cross section σ_{NN}^{in} of the nucleon-nucleon collision is the same as in the vacuum. It means that secondary particle production and excitation of nucleons are not taken into account. A collision is treated as multiple nucleon-nucleon interactions. The geometry of variables used in the Glauber model is shown in Figure 1.6. N_{part} and N_{coll} is computed by the Glauber model as follows [2]:

8
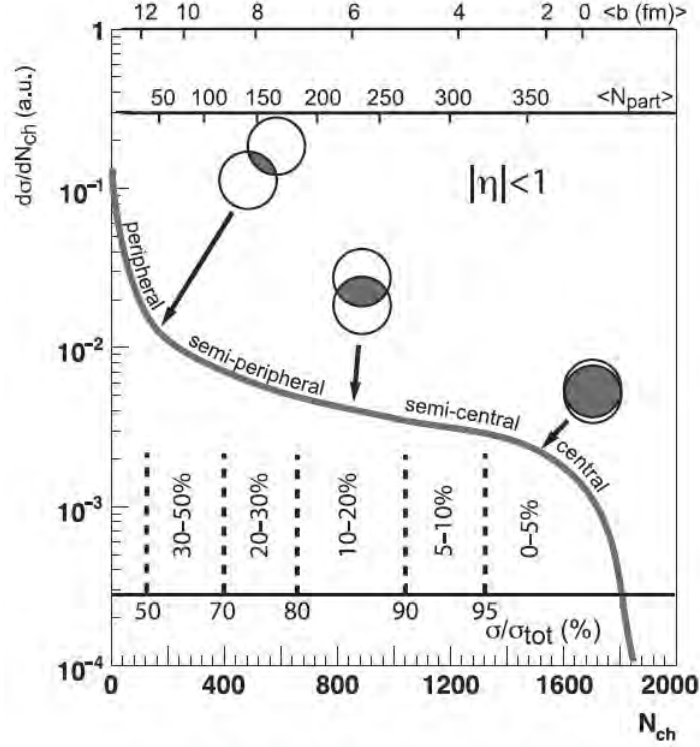
Figure 1.5: Distribution of number of produced charged particles N_{ch}. The graph also depicts the centrality definition from the final-state particle multiplicity and its correlation with the the impact parameter b, the number of participating nucleons N_{part} in the collision, centrality classes and the ratio of cross section σ in the most central collision to total cross section σ_{tot} of produced particles [8].

$$N_{part}(b) = \int d^2s \, T_A(s) \left(1 - e^{-\sigma_{NN}^{in} T_B(s)}\right) + \int d^2s \, T_B(s-b) \left(1 - e^{-\sigma_{NN}^{in} T_A(s)}\right) \quad (1.3)$$

$$N_{coll}(b) = \int d^2s \, \sigma_{NN}^{in} T_A(s) T_B(s - b) \quad (1.4)$$

where T_A is the thickness function defined as $T_A(s) = \int dz \rho_A(z, s)$, z is an axis along the beam, b is the impact parameter, s is a distance in Figure 1.6, σ_{NN}^{in} inelastic cross section and ρ is the nuclear mass number density usually given by Wood-Saxon parametrization and normalized to the mass number A. The average N_{part} for an A+A collision is calculated by equation (1.3). N_{part} for a p+p collision is equal to 2 and for a p+A collision $N_{part} = N_{coll}+1$.

1.4 Signatures of QGP

In a high energy heavy-ion collision QGP might be created and the probability of its formation depends on centrality, the center of mass energy and size of colliding
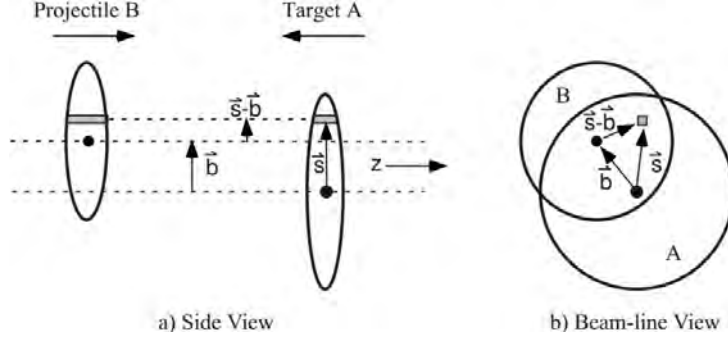
Figure 1.6: A schematic representation of the Glauber model geometry with longitudinal (a) and transverse (b) views [9].

ions. To determine if QGP was present in a collision it is necessary to have sensitive probes which carry information about created medium. The state of a quark gluon plasma created during the collision lasts for a very short time and for this reason its direct detection is very difficult, because only hadrons and leptons in the final state are observable. Thus it is required to find out probes and methods for studying QGP indirectly. Particles that arise from the collision carry important information about properties of QGP and they represent indirect indication of deconfined phase of matter. The most important signatures of presence of QGP in a heavy-ion collision are elliptic flow, suppression of particles with high p_T, jet quenching (described in the 3rd chapter), strangeness enhancement,quarkonium suppression, direct photons, dileptons[5] [?].

1.4.1 Nuclear Modification Factor

A nuclear modification factor is a convenient tool for probing of QGP quantitatively. The nuclear modification factor expressed by formula 1.5 compares a p_T differential yield of high p_T hadrons or jets in a heavy-ion collision to the differential production cross section in a p+p collision at the same center of mass energy:

$$R_{AA}(b, y, p_T) = \frac{1}{\langle T_{AA}(b) \rangle} \frac{\mathrm{d}^2 N_{AA}/(\mathrm{d}y\mathrm{d}p_T)}{\mathrm{d}^2 N_{pp}/(\mathrm{d}y\mathrm{d}p_T)} \tag{1.5}$$

T_{AA} is a nuclear overlap function that accounts for the increased parton flux in A+A collisions compared to p+p collisions and it is related to the number of binary nucleon-nucleon collision N_{coll} that are calculated by the Glauber model [10].

If the nuclear modification factor is equal to 1, then there is no difference in yields between p+p and A+A therefore no effects of medium on particle production are observed. The case when $R_{AA} < 1$ is referred to as a suppression and the number of particles produced in A+A collision is smaller than in p+p. At $R_{AA} < 1$ we observe medium effects on particle production and thus QGP might be eventually present. When $R_{AA} > 1$ it denotes enhancement in particle production, known as the Cronin enhancement. The main source of enhanced hadron production at intermediate p_T (3-6 GeV/c) is mainly partonic scattering at the initial impact and multiple interactions in nuclear matter [11].

Comparison of R_{AA} between d+Au and Au+Au collisions can be seen in Figure 1.7. In Au+Au collisions we can observe suppression, that is associated with the formation of the medium. In this case, production of particles with high p_T exhibits significant suppression by the factor 5. The production of particle was influenced by final state interaction with the dense matter (shadowing and partonic energy loss in dense matter). d+Au collisions exhibits enhancement of particle production due significant role of Cronin effect at $2 << 7$ and the absence of effects of dense medium.
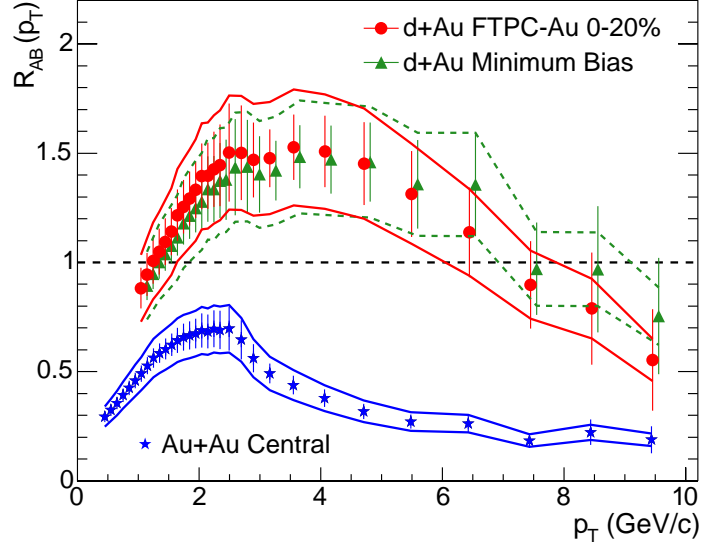
Figure 1.7: The nuclear modification factor R_{AB} for minimum bias (triangles) and central d+Au collisions (circles), and central Au+Au collisions (stars) at $\sqrt{s_{NN}} = 200$ GeV measured by the STAR experiment at RHIC [12].

Example of results for nuclear modification factor R_{AA} for suppression of charged particles as a function of p_T and different collision centralities in Pb+Pb collisions at $\sqrt{s_{NN}} = 200$ GeV measured by ALICE are shown in Figure 1.8

There is also a second possibility to describe influence of the medium on particle production. We can compare collisions with different impact parameters: central and peripheral collisions. For this purpose nuclear modification factor R_{CP} is defined:

$$R_{CP}(y, p_T) = \frac{\langle N_{coll,cent} \rangle}{\langle N_{coll,per} \rangle} \frac{\mathrm{d}^2 N_{cent}/(\mathrm{d}y \mathrm{d}p_T)}{\mathrm{d}^2 N_{per}/(\mathrm{d}y \mathrm{d}p_T)} \tag{1.6}$$

R_{CP} is usually used if data from p+p collisions are not at disposal at the same $\sqrt{s_{NN}}$ as A+A collision or they have too small statistics. Figure 1.9 illustrates nuclear modification factor R_{CP} of charged hadrons and jets at ALICE, charged hadrons at CMS and full jets at ATLAS. We can see strong suppression of jets in range $30 < p_{T,jet} < 100$ GeV/c by a factor of 2 that is comparable to the suppression of charged hadrons.

11
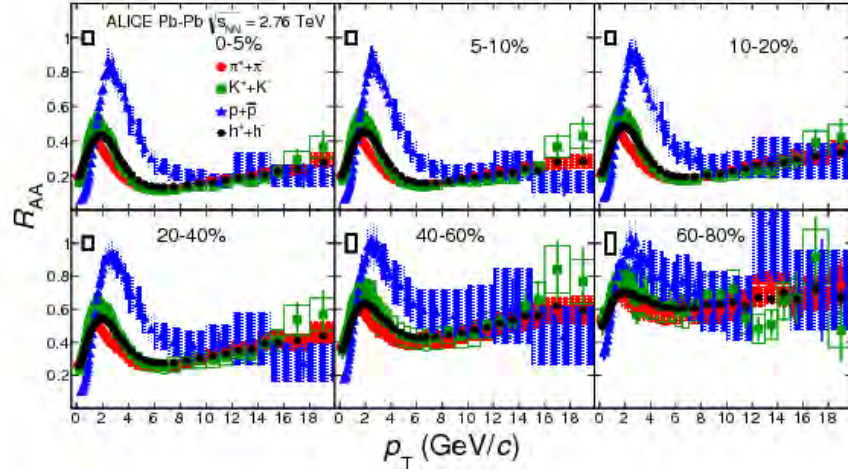
Figure 1.8: The modification factor R_{AA} for suppression of charged particles as a function of p_T and different collision centralities in Pb+Pb collisions at $\sqrt{s_{NN}} = 200$ GeV measured by ALICE [13].
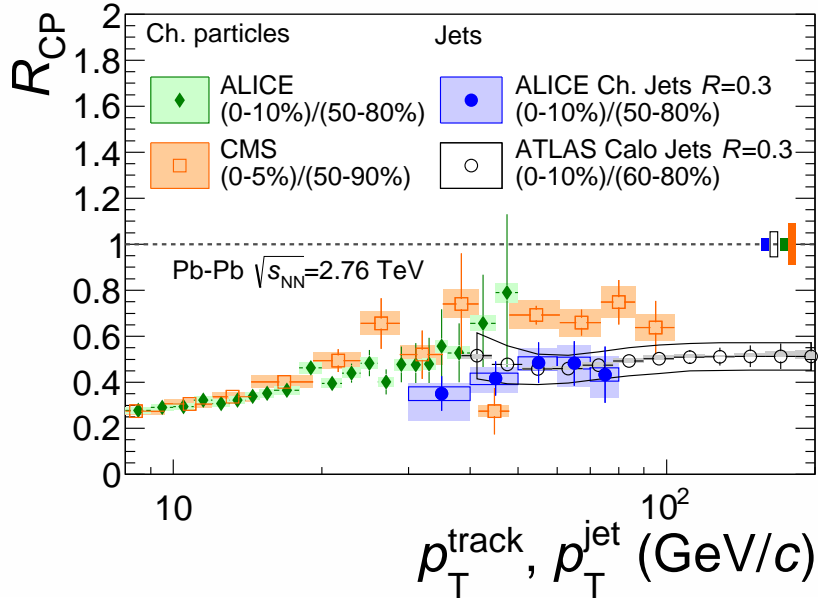
Figure 1.9: The nuclear modification factor R_{CP} measured by the ALICE, the AT-LAS and the CMS experiment for charged hadrons, charged and full jets in central and peripheral Pb+Pb collisions at $\sqrt{s_{NN}} = 2.76$ TeV[14].

1.4.2 Elliptic flow

When a collision is non-central, the overlap region of nuclei has an ellipsoidal shape. The geometry anisotropy of the primordial interacting zone results in imbalanced pressure gradients and thus collective anisotropic azimuthal emission of hadrons in a plane in the beam direction [5]. This is referred to as an elliptic flow. According

to hydrodynamics pressure gradients are the largest in the direction of the reaction plane and the system will expand mainly in this direction. The largest elliptic flow is measured in non-central collisions and the lowest in central collisions in which there is no asymmetry [2].

Elliptic flow can be expressed mathematically by a parameter v_2 that is derived from a Fourier expansion of hadron production depending on azimuthal angle ϕ to the plane of the collision ψ_r as:

$$E\frac{d^3N}{d^3p} = \frac{d^2N}{2\pi p_T dp_T dy}\left(1 + \sum_{n=1}^{\inf} 2v_n \cos[n(\phi - \psi_r)]\right) \quad (1.7)$$

where E is energy, p momentum, p_T transverse momentum, ϕ azimuthal angle, y rapidity of a particle and ψ_r angle of direction to event plane. The coefficients v_n in the Fourier expansion are calculated by:

$$v_n(p_T, y) = \langle \cos[n(\phi - \psi_r)]\rangle. \quad (1.8)$$

Parameter v_1 denotes direct flow and v_3 triangular flow.
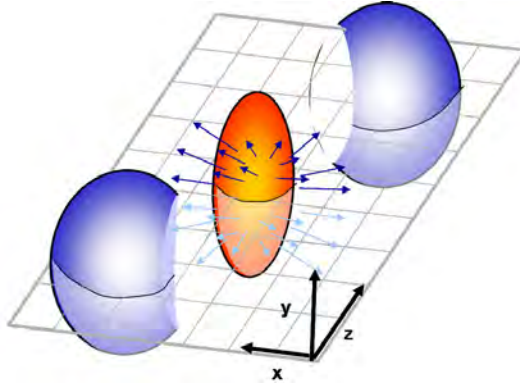
Figure 1.10: A schematic view of the collision zone of two incoming nuclei [15].

1.4.3 Strangeness enhancement

The next signature for possible indication of QGP formation is the enhancement of strangeness production in QGP with respect to p+p collisions. At the initial stage of a heavy-ion collision no valence strange quarks are present because protons and neutrons consists of u and d quark, since the production of strange quark in observed strange particles is the consequence of collision itself. Higher production of strange particles is caused by the fact that the production rate of strange quark and anti-quark pairs via gluon fusion is higher in QGP due to the low energy threshold for dominant QCD processes of $s\bar{s}$ production. In a deconfined state of matter, in which there is a large gluon density, the abundances of parton species quickly reach their equilibrium values, resulting in a higher abundance of strangeness per participant than what is seen in p+p interactions, in which there is higher threshold for strangeness production. [16].

1.4.4 Quarkonium suppression

Quarkonia suppression is the next important signature of QGP and it was proposed by T. Matsui and H. Satz in [17]. Quarkonia are bound states of heavy quark and anti-quark, for example $c\bar{c}$ - charmonium (J/ψ), $b\bar{b}$ - bottomium (Υ). Heavy quarks are produced in hard scattering in the initial stage of a collision and since they experience the whole QGP evolution. If a quarkonium is placed in the QGP with the temperature higher than binding potential of quarkonium, surrounding quarks and gluons will screen the color charge. The screening referred to as Debye screening effectively weakens the interaction between heavy quark and anti-quark and string tension between them vanishes. This leads to dissociation of quarkonia resulting in the suppression of its production in heavy-ion collisions with respect to p+p collisions[18]. Differences in quarkonium binding energies lead to a sequential melting of quarkonia states with increasing temperature. This feature can be used for estimation of temperature of the medium from production measurement of states that survived. At higher energies the expected greater suppression is compensated by quarkonium regeneration through recombination of two independently-produced heavy quarks. [19].

Chapter 2

The STAR Experiment

2.1 RHIC

The Relativistic Heavy Ion Collider (RHIC), shown in Figure 2.1, is the second largest collider in the world currently in operation. It is the first device capable of colliding heavy ions which has begun operation in 2000. RHIC is located at Brookhaven National Laboratory (BNL) on the Long Island near New York. RHIC was built in order to collide relativistic protons and heavy ions to study formation of quark-gluon plasma and spin physics by experiments with polarized protons. RHIC is able to collide various ion species, as well as enables study of asymmetric collisions - beams with unequal masses. So far following systems were measured: p+p, d+Au, ^{3}He+Au, Au+Au, Cu+Cu, Cu+Au, U+U. From the point of varying energies and combination of any colliding nuclei is RHIC a unique accelerator in the world. The maximum energy of beam for collisions of heavy nuclei is $\sqrt{s_{NN}} = 200$ GeV per nucleon pair and $\sqrt{s} = 500$ GeV for p+p collisions. For Beam Energy Scan are used different energies of Au+Au collisions ranging from $\sqrt{s_{NN}} = 7.7$ to 62 GeV [20].

RHIC consists of two separated storage rings (the yellow and blue beam line) of superconducting magnets, that are 3.8 km long in circumference with six intersection points located on straight sections between 6 arc sections. The superconducting magnets include various types: dipoles, quadrupoles and sextupoles, that are utilized to bend, focus and steer the beams. The total number of magnets is 1740 and they are cooled to temperature of less than 4.6 K. For accelerating heavy ions to the maximum energy it is necessary to utilize accelerator complex. Firstly heavy ions are accelerated to energy of 2 MeV/nucleon by the Electron Beam Ion Source [21]. Ions continue to the Booster Synchrotron, where they are accelerated to 95 MeV/nucleon and then delivered to the AGS where they reach energy up to 10.8 GeV/nucleon. Finally the ions are injected to RHIC via the Beam Transfer Line. Before each section, heavy ions are always partially stripped of electrons. Polarized protons start accelerating at 200 MeV Linac and then they undergo the same accelerating scheme as heavy ions [22]. During physical run, RHIC stores 111 bunches with intensity of 10^9 ions in each storage ring. Initially, RHIC was used for four independent experiments: BRAHMS, PHOBOS, PHENIX and STAR. BRAHMS and PHOBOS were small experiments which concluded their physics program in 2006. BRAHMS was designed and build in order to measure charged hadrons over a wide range of rapidity and transverse momentum (momentum spectroscopy) to study the

reaction mechanisms of the relativistic heavy-ion collisions and the properties of stongly interacting matter (measurement of small-x" and saturation physics) [23] The PHOBOS detector consisted of two spectrometers made of silicon detectors and had the largest pseudrapidity coverage of all RHIC detectors, it had been tailored for bulk particle multiplicity and particle angular-distribution measurement. The PHENIX detector was specialized to detect photons and leptons that are not affected by strong interaction and carry unmodified information about processes within the collision, using a partial coverage detector system (two central arms) in a super-conductively generated axial magnetic field. Nowadays STAR is the only working detector at RHIC, as the PHENIX experiment ended its operation in 2016. However PHENIX detector is currently being rebuilt to a new experiment SPHENIX. SPHENIX will focus on jets, jets corellations and beauty quarkonia physics to determine the temperature dependence of transport coefficients and the color screening length in the QGP.

In the future, a significant upgrade of RHIC to eRHIC is planned; a new 10 GeV high intensity electron/positron beam will be constructed along existing hadron collider. This new project will attempt to answer questions about distribution of sea quarks and gluons, and their spins in space and momentum inside the nucleon; saturation of gluon desities and how does the nuclear environment affect the distribution of quarks and gluons and their interactions in nuclei.[24]
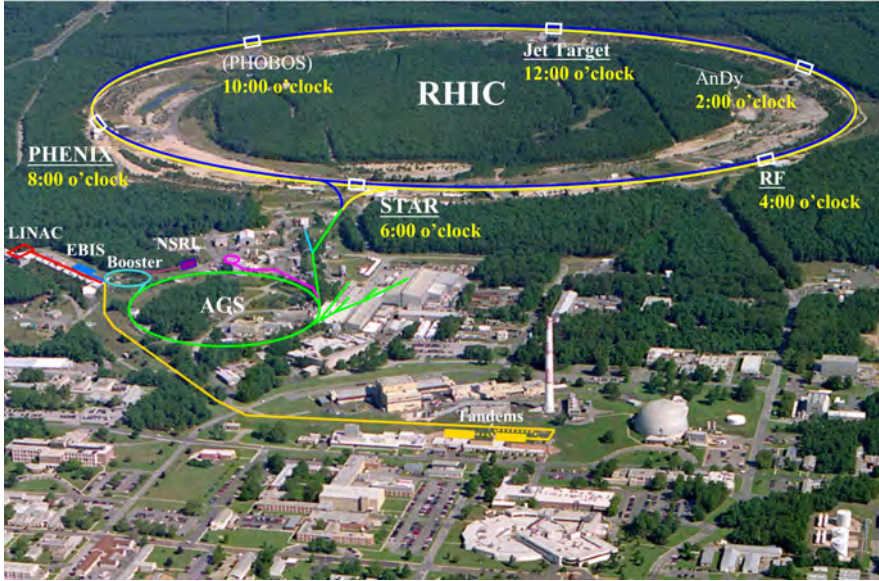
Figure 2.1: Relativistic Heavy Ion Collider [25].

2.2 STAR detector

The STAR detector [26] (Solenoidal Tracker at RHIC), depicted in Figure 2.2, was built in order to study behavior and properties of strongly interacting QCD matter produced at high temperatures and energy densities produced in high energy heavy-ion collisions and also participates in spin physics program with $\sqrt{s} = 500$

GeV p+p collisions. It is a multi-purpose detector able to observe and identify the majority of particles produced in a collision. The STAR detector is located at the intersection point that is at the 6'o clock position of the RHIC collider. It has a shape of a cylinder with detector layers around the beam axis. Most of the detectors are placed at mid-rapidity and have full azimuthal angle coverage. The STAR detector is 6.85 meters long and its radius is 7.32 meters. Around the whole detector is a large solenoidal magnet with magnetic field of 0.5 T. STAR consists of several types of detectors and subsystems which allow tracking, triggering, particle identification and measurement of deposited energy of particles. These detectors are: Time Projection Chamber (TPC), Time Of Flight detector (TOF), Barrel ElectroMagnetic Calorimeter (BEMC), Vertex Position Detector (VPD), Beam Beam Counter (BBC), Muon Telescope Detector (MTD), Zero Degree Calorimeter (ZDC), Heavy Flavor Tacker (HFT, 2014-2016), and others. The main purpose of the STAR experiment is to measure with large spatial acceptance hadrons, leptons and photons arising from proton-proton or heavy-ion collisions.
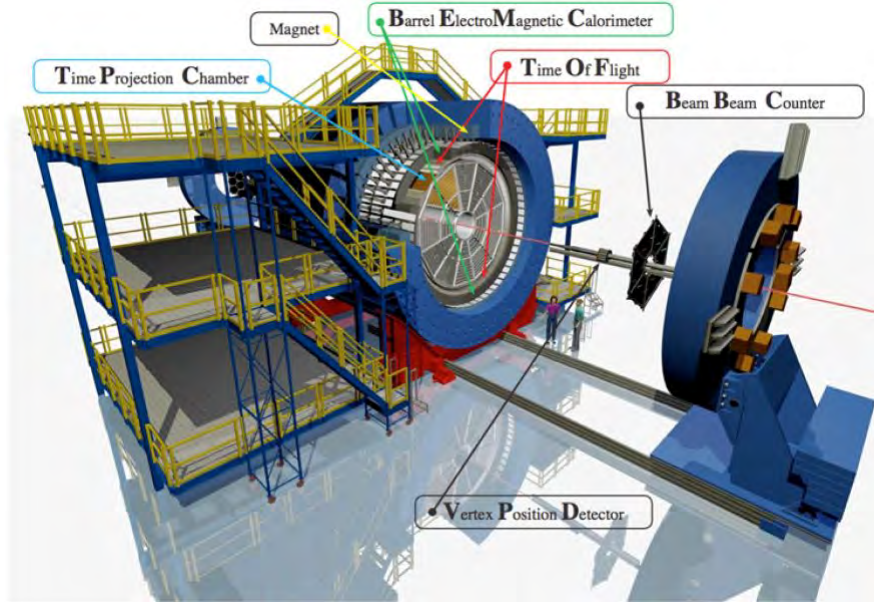
Figure 2.2: STAR detector [27].

2.2.1 Time projection chamber

The Time Projection Chamber (TPC) [28] is the largest detector of STAR. Its main function is track reconstruction of charged particles on the basis of the measurement of specific ionization energy loss and curvature of tracks in the magnetic field of 0.5 T parallel to the beam pipe. The TPC has a cylindrical shape and length 4.2 meters, inner radius is 50 cm and outer radius is 200 cm. It covers full azimuthal angle 2π with pseudorapidity $|\eta| \leq 1$. It is filled with P10 gas regulated at the pressure of 2 mbar larger than atmospheric pressure. Gas P10 is a mixture of two gases: argon (90%) and methane (10%). In order to obtain good detection performance, gas should not influence yield or velocity of electrons. Inert gas does not decelerate

electrons and does not capture them and organic gas prevents propagation of UV rays. The TPC consists of a central cathode and two anodes located at sides. The whole detector is divided into two parts, where in between is a thin carbon coated annulus membrane - High Voltage membrane with 28 kV. The function of this membrane is to form a uniform longitudinal electric field that is parallel to the beam pipe and its value is 135 V/cm. At both ends of the TPC there is a readout system based on multi-wire proportional chambers (MWPC). The end caps contain 12 sectors of anode pads. A scheme of the TPC is depicted in Figure 2.3. The TPC is able to register a maximum of 45 independent points for a charged tracks.

A charged particle going through the TPC ionizes the gas around its track and releases electrons from gas molecules. These kicked out free electrons are accelerated in the electric field and drift with the constant velocity to the anode end caps. Before electrons reach end of the TPC, their velocity is increased by electric field to allow ionization of gas and produce another electrons in the avalanche. The average velocity of an electron is referred to as a drift velocity. The average number of produced electrons is proportional to the energy released in the detector (or energy that particle loses in the TPC). Then the signal of the electron is amplified and recorded. Wires of Multi Wire Proportional Chambers (MWPC) are formed into grid, which allows us to determine two coordinates (x,y) of each part of a track. The longitudinal coordinate z is obtained from the time of drift. This means that the TPC is able to reconstruct tracks in 3 dimensions, therefore we can obtain important information about trajectory of each charged particle passing through the TPC. The spatial resolution in x, y direction is 460 μm and 700 μ in z. Readout time of the TPC (drift time of electrons) is 40 μs.

To calculate energy loss of a particle in material, the Bethe-Bloch formula is used:

$$\frac{dE}{dx} = 4\pi N_A r_e^2 m_e c^2 z^2 \frac{Z}{A} \frac{1}{\beta^2} \left(\frac{1}{2} \ln \frac{2 m_e c^2 \beta^2 \gamma^2 T_{max}}{I^2} - \beta^2 - \frac{\delta}{2} \right) \tag{2.1}$$

where N_A is the Avogadro number, r_e classical electron radius, m mass of particle that loses energy, c speed of light in vacuum, ρ density of material, Z proton number, A nucleon number, W_{max} maximum energy transfer in a single collision, I mean excitation energy and δ density correction. This formula allows to identify particles as can be seen in Figure 2.4 where the $\frac{dE}{dx}$ is shown as a function of momentum of particles measured by the STAR TPC. Momentum of particles is computed from the fit of helix of the tracks that are deflected in the magnetic field.

In the next year, enhancement of TPC permormace is planned by upgrading of inner sectors to increase segmentation of the padplane and renew wires. The new iTPC will provide better dE/dx, particle identification and momentum resolution, improve acceptance at high η and low p_T and reduce systematic uncertainties.

2.2.2 Time of Flight detector

The Time of Flight detector (TOF) of STAR [22] is designed to improve direct identification of hadrons. It is located between the TPC and the BEMC and covers full azimuthal angle and pseudorapidity $|\eta| \leq 1$. The TOF is based on Multi-gap Resistive Plate Chamber (MRPC) technology. The MRPC module is in each tray and there are 120 trays included in the TOF. The TOF detector is activated by a VPD (Vertex Position Detector) and together with momentum obtained from the
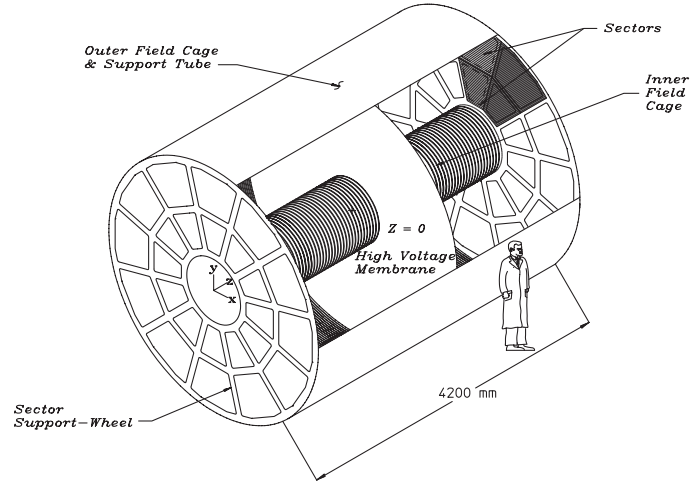
Figure 2.3: A schematic view of a Time Projection Chamber [28].
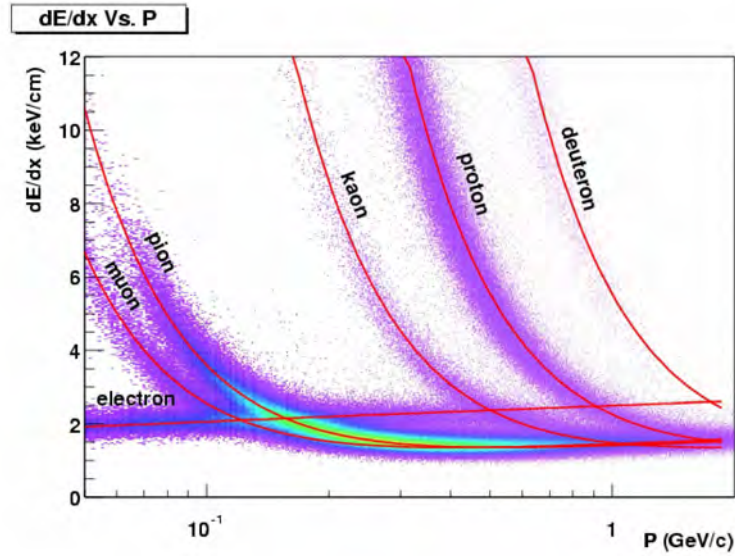
Figure 2.4: The result of energy loss dE/dx distribution measurement in TPC STAR as a function of the transverse momentum p_T. Measurement is used for particle identification [28].

TPC improves precision of particle identification. The time resolution of the TOF is high - 100 ps and allows TOF to effectively distinguish electrons from heavier hadrons with a low momentum. Thus it is possible to identify pions and protons to 7-8 GeV/c, kaons to 3 GeV/c and electrons in the interval of 0.15 - 4 GeV/c

[29]. High momentum particles are determined by other detectors, e.g. the BEMC discussed below. The principle of particle determination or respectively its mass is as follows: the time of flight particles traversing through detector is measured. The starting time t_0 is recorded by the VPD and the TOF measures the end time t_1. From these measurements we can obtain the time-of-flight interval $\Delta t = t_1 - t_0$. Then using the interval Δt and the length s of particle track acquired from the TPC, the value of inverse velocity is computed:

$$\frac{1}{\beta} = \frac{c\Delta t}{s}.$$ (2.2)

Finally from the momentum of the particle and its velocity β we are able to calculate mass according to the formula:

$$m = p\sqrt{\left(\frac{1}{\beta^2}\right)^2 - 1}$$ (2.3)

2.2.3 Barrel Electromagnetic Calorimeter

The STAR Barrel Electromagnetic Calorimeter (BEMC) [30] is located between the TOF detector and the solenoidal magnet. Its distance from the beam pipe is 223.5 cm. It covers full azimuthal angle and has pseudorapidity coverage $|\eta| \leq 1$. Its purpose is to measure energy deposition of high momentum particles such as photons, electrons and hadrons. The BEMC consists of 120 calorimetric modules (in azimuthal angle), each segmented into 40 towers (in pseudorapidity). A view of the BEMC module is illustrated on Figure 2.5. The total number of towers in the BEMC is 4800, where the effective size of the tower as the BEMC resolution is 0.05 x 0.05 = $\Delta\phi$ x $\Delta\eta$.

The BEMC is a sampling calorimeter and the core of each calorimeter module comprises of a lead-scintillator stack and shower maximum detectors (BSMD). It is made of 41 layers, where 21 layers are active scintillators that measure deposited energy of traversing charged particles and between them there are lead absorber plates. As a charged particle traverses these lead layers it produces an electromagnetic shower. This shower is detected by scintillators that convert energy of particle from the shower into the light and according to intensity of light we are able to determine amount of deposited energy of the particle. The actual deposited energy in the calorimeter depends on the type of particle and thus allows its identification.

The thickness of the BEMC detector is approximately 20 radiation lengths for an electron. The radiation length is defined as a distance that a high energy electron has to pass to lose $1/e$ of its original energy by radiation referred to as bremsstrahlung. Energy-momentum ratio E/p for high energy electron is 1. Due to this, it is expected that electrons and photons are completely stopped in the BEMC because they lose their whole kinetic energy. In contrast the cross section of hadrons with lead is much smaller in comparison to electrons. This means that hadrons are less ionizing particles $E/p < 1$. They do not lose their whole energy in the detector and they pass through it. Consequently, it is possible to distinguish high energy electrons form hadrons. By measuring deposited energy of high energy particles in the BEMC and by detecting their produced showers, we are able to study high p_T processes as leading hadrons and jets.
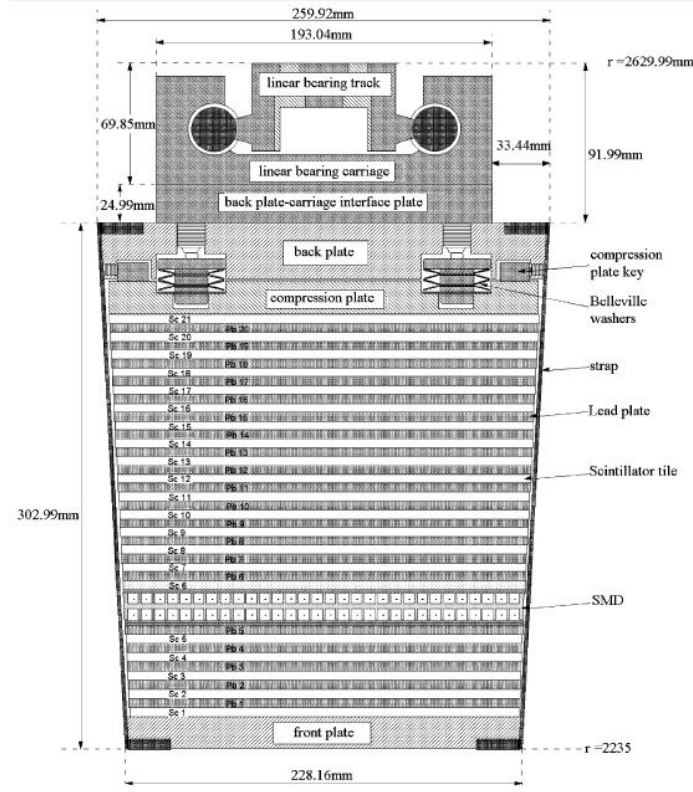
Figure 2.5: A schematic view of the BEMC module [30].

2.2.4 Beam Beam Counter

There are two Beam Beam Counters (BBCs) on both sides of the STAR detector. They are located 3.5 m before the intersection point in STAR and surround the beam pipe. They cover pseudorapidity in the interval of $2.1 < |\eta| < 5.0$. The main function of the BBC is to locate the position of a collisional vertex and determine collision centrality. The BBC consists of two rings of hexagonal scintillators.

2.2.5 Zero Degree Calorimeter

The main capability of Zero Degree Calorimeter (ZDC) is monitoring the luminosity, triggering and especially measuring of detected number of spectators (neutrons) in the forward direction to determine centrality of the collision. The ZDC is located approximately 18 m from the center of the STAR detector on its both sides and consists of several tungsten plates, wavelength-shifters and photomultipliers that detects Cherenkov radiation of neutrons.

2.2.6 Vertex Position Detector

The capability of the Vertex Position Detector (VPD) is determination of z position of the primary vertex - the point of collision. The VPD measures the start time for the TOF. It covers pseudorapidity $4.24 < |\eta| < 5.0$. There are two VPDs (West and

East) located on both sides of STAR in the distance of 5 m from the intersection point and they surround the beam pipe. The VPD consists of 19 detectors, each of them composed of a lead converter followed by a fast plastic scintillator that is read out by a photomultiplier tube (PMT).

2.2.7   Muon Telescope Detector

The Muon Telescope Detector (MTD) [31] enables detection of muon pairs from QGP thermal radiation, quarkonia, light vector mesons and heavy flavor through semileptonic decays. These processes can be studied also through photons or electrons, but in comparison to muons they have larger background. The MTD is situated on the top of the solenoidal magnet. Its location is convenient because there is very low hadronic background and noise. Muons are more penetrating than hadrons therefore mainly muons pass through the whole STAR and reach the MTD. For this reason we are able to distinguish and observe different Υ states. The MTD covers only 45 % of the full azimuth, its pseudorapidity coverage is $|\eta| < 0.5$ and its radius is 4 m. In the MTD there is installed a similar detection system and technology - MRPC as in the TOF.

2.2.8   Heavy Flavor Tracker

The main function of Heavy Flavor Tracker (HFT) [32] is to precisely determine the secondary vertex of mesons that rapidly decay and contain heavy quarks, like D^0 or B^0. The HFT improves analysis of heavy flavor because with the TPC it significantly improves particle identification and momentum resolution of tracks .The HFT is a system of three detectors: two layers of a silicon pixel detector (PXL), an intermediate silicon tracker (IST) and a silicon strip detector (SSD). It is located in the center of STAR and it is first detector of STAR through which a particle passes. The minimal radius of the HFT is only 2.5 cm and hence it tightly surrounds the beam pipe that had to be thiner than in another place at RHIC. The HFT was installed within the STAR detector in 2014 and its operation ended in 2016.

2.2.9   Trigger system

In a typical Au+Au collision at $\sqrt{s_{NN}} = 200$ GeV, a large amount of data is produced, but technically it is not possible to analyze and register all data from all events, because the operating speed of STAR detectors is smaller than collision rate of RHIC. Therefore we need to reduce the rate of readout and for this function a trigger system is used.

The STAR trigger system is divided into four Levels: 0, 1, 2, 3 [33] . It uses information measured by fast detectors and based on knowledge of this decides whether a given event is suitable to trigger on and to be registered. The main fast detectors used for triggering are ZDC, VPD, BBC, TOF and BEMC. Level 0 consists of ZDC, VPD and BBC. Each collision is monitored by detectors of Level 0 that govern if the collision fulfils defined requirements or not.

If the event is evaluated positively then the Level 1 and 2 starts. They are more time-consuming due to complex analysis of the trigger data. The main aim of Level 1 and 2 is to determine if the event fulfils more finely grained criteria. Simultaneously

digitalization process and data transmission phase of the TPC take place and they can be aborted by these two Levels if data do not comply. Level 3 represents on-line analysis preformed by large CPU farms. Produced data are reduced and stored by a Data Acquisition System (DAQ) on tapes using technology of High Performance Storage System (HPSS).

Chapter 3

Jets

3.1 Definition of a jet

One possibility how to study the strong interaction and properties of QGP is observation and analysis of jets which play a crucial role in hard scattering and hadronisation studies that help in establishing the QCD theory. Jets are experimental signatures of partons: quarks and gluons. Jets are narrow conical sprays of particles, which are produced in the hard scattering during very first moments of ultra-relativistic electron, proton or heavy-ion collisions. According to the QCD, initial hard scattering can produce a high p_T parton with large virtuality Q that successively decrease by gluon radiation resulting in the production of quark-antiquark pairs moving along the trajectory of the original leading parton. This is referred to as a fragmentation. New partons are color charged and due to color confinement they cannot remain free. Instead they combine together and form color charge neutral hadrons in the process called hadronisation. This results in a jet which is a collimated shower of particles, mainly hadrons (mostly pions and protons) and posses same kinematic properties as the original parton. Proper analysis and thorough physical interpretation of measured jets allow us to access initial stages of the collision and obtain useful information about medium created in the collision area.

Jets are always created in pairs of opposite direction ($\Delta\phi \approx \pi$) in their center of mass reference frame, because an emerging quark and antiquark that are produced during hadronisation process have to conserve momentum. Such events are called di-jet events. They are the most common in p+p collisions. But also sometimes a quark radiates a gluon before hadronisation. The gluon fragments producing a new jet. Therefore we can also observe three-jet, four-jet... events. Figure 3.1 in the left depicts theoretical interpretation of a jet event, while the right panel shows the illustration of experimental view of the jet event.

According to the parton type, from which a jet originates, we divide jets into several categories, for example a jet originated from a heavy flavor quark b, t, c, light-quark jets or gluon jets. We also distinguish two type of jets: charged and full jets. Charged jets are reconstructed from charged tracks while full jets contain also neutral component from towers in calorimeters.

In the present, QCD calculations and simulations are able to describe jet production in e+e and p+p collisions satisfactory. But on the other hand, a heavy-ion collision is a high-multiplicity environment with fluctuating background and current

theoretical models are limited to describe sufficiently all processes in such collision. Therefore more detailed studies of jet production from the theoretical and experimental point of view are required to better understand what we measure.
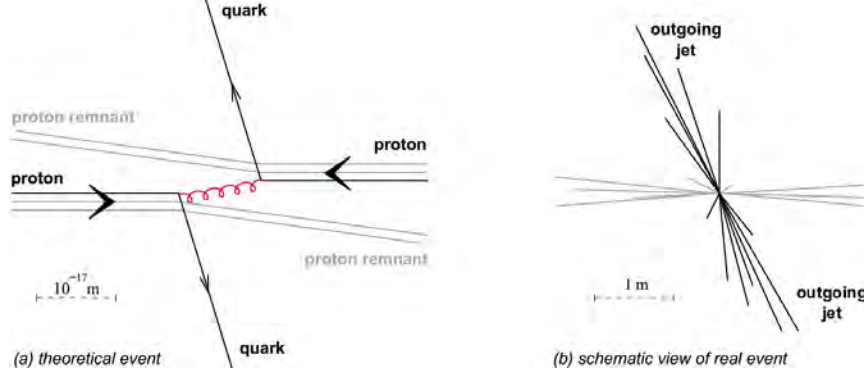
Figure 3.1: (a) Theoretical interpretation of p+p collision, (b) schematic representation of real event [34].

3.1.1 Jet quenching

Hard scattering at the initial stage of heavy-ion collisions occurs before QGP formation and therefore initial jet production originating from recoiled partons is not affected by the medium. But when the medium is produced, partons from the hard scattering have to pass through it. If a high p_T parton (> 2 GeV/c), also referred to as a hard probe propagates through strongly interacting dense medium - QGP, it loses energy by two mechanisms: elastic and inelastic scatterings with the surrounding medium constituents, in other words by collisional (dominant at lower energies) and radiative (dominant at higher energies) energy loss [35]. After subsequent hadronisation the quantity of observed high p_T hadrons might be smaller, because they can be absorbed by medium or their energy strongly attenuated. This effect might cause modification of the spectrum of jets and their properties. This phenomenon is referred to as a jet quenching and its first evidence has been observed in $\sqrt{s_{NN}} =$ 200 GeV Au+Au collisions at RHIC [36] and later at the LHC [37]. Jet quenching is depicted in Figure 3.2. On the left-hand side of the figure there is a di-jet event arising from the p+p collision, where no surrounding medium is present and there is no reason for jets to be modified. From the experimental point of view the size and the momentum of both opposite jets is almost the same due to the conservation of the momentum. Contrary to p+p collision that are used as a reference, the right part of the figure shows a heavy-ion collision, in which the medium is created and jets might be modified or eventually quenched. We assume two jets arising from two recoiled partons created in the peripheral region of the collision. One of the partons has to traverse longer distance through the medium than the other one. Due to more interactions with the medium it loses more energy than the opposite parton that almost immediately emerges from the medium with a minimal change of its size or momentum. Jet quenching provides direct information on the QCD matter and its thermodynamical properties such as temperature, energy or particle densities and

transport properties (viscosity, diffusivity and conductivity coefficients) that can be obtained by comparing the jet production in heavy-ion collisions to proton-proton collisions [35].
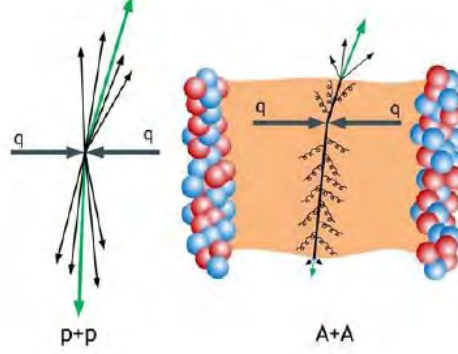
Figure 3.2: Jet quenching [38].

3.2 Jet levels

From the formation to the observation of hadrons that are produced by scattering of two partons of colliding nuclei, a jet undergoes a complicated process. Jet evolution can be divided into three levels [39] and they can be seen in Figure 3.3:

- Parton level - the jet is formed by a cluster of partons. This level is calculated by perturbative Quantum Chromodynamics and it uses two approaches: Leading Order (LO) and Next to Leading order (NLO).

- Particle level - the jet is formed by hadrons in the final state. This level is used for generation data in Monte Carlo simulations.

- Detector level - represents all signals (towers or charged tracks) that are registered by detectors in $\eta - \phi$ plane. To each signal is assigned information about trajectory, energy or momentum and these data are used for jet reconstruction.

3.3 Jet reconstruction

For jet reconstruction several types of jet finding algorithms were developed and currently they are widely used in jet analysis in experiments at the LHC or RHIC. Jet algorithm is a set of procedures and instructions that aim for identifying jets as the observable counterparts of the perturbative concept of partons. The right definition of jet algorithm is crucial for comparison of experimental analysis with theory. The jet-finder can be applied both to perturbatively predicted partonic configurations and to observed hadronic configurations. The main goal of jet algorithms is to cluster a set possible jet constituents in these configurations to a jet. We are focused on jet reconstruction at detector level thus jet-constituent candidates usually comprise
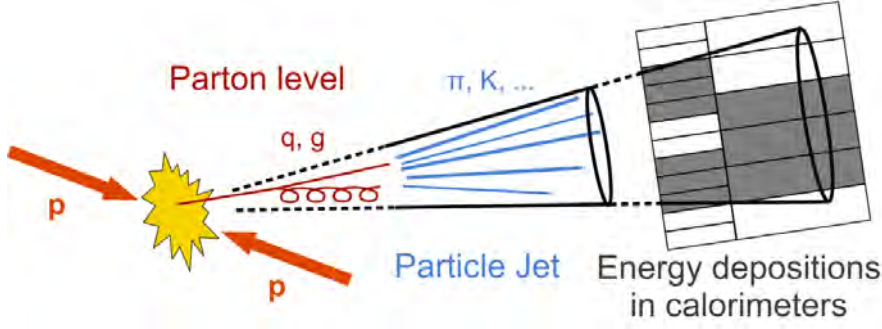
Figure 3.3: Achematic illustration of jet evolution at parton, particle and detector level [40].

of charged tracks and neutral calorimeter towers measured by various detectors in $\eta - \phi$ plane, where η is pseudorapidity and ϕ is azimuthal angle.

At the beginning, the algorithm selects a list of particles, which are typically emitted close to each other in azimuthal and polar angle because jet candidates generally originate from the initial hard parton and have same direction as the original parton. At experimental (detector) level the particles are hadrons and partons in a pQCD calculation or simulation level. During the jet analysis, each jet is assigned a four-momentum $p = (E, \vec{p}) = \sum(E^i, p_x^i, p_y^i, p_z^i)$ and transverse momentum $p_T = \sqrt{p_x^2 + p_y^2}$. The jet algorithm associates momenta of measured candidates according to well-defined rules (depends on algorithm scheme) to form the momentum of a jet. The momentum addition rule is called the recombination scheme.

3.4 Attributes of ideal jet algorithm

An ideal jet algorithm has to fulfill several theoretical and experimental attributes, because there is no unique definition of a jet. The result of the jet reconstruction usually depends on a type of algorithm used. To get a correct result or at least a result, which converges to the right solution and complies with the demands of the study, every reliable jet algorithm has to fulfill following criteria [39]:

- Full specification: jet selection process, jet kinematic variables, specifications for clustering, energy and angle definition, and all details of jet splitting and merging should be clearly and completely defined.

- Detector independence: application of jet algorithm should provide similar results on various types of detectors, which differ from each other in size, cell type, detector segmentation, energy response or resolution.

- Order independence: algorithm behaves equally in pQCD calculations, simulations and data reconstruction (parton, particle and detector level).

- Infrared safety: algorithm should find a solution which is insensitive to any soft radiation in the event - any radiated soft gluons or products of hadronisation

will not influence existence, number, axis direction or shape of a jet. Figure 3.4 illustrates infrared safety of a jet algorithm.
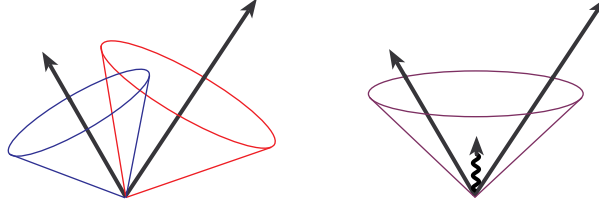
Figure 3.4: Illustration of infrared sensitivity of a jet algorithm [39]. The left side of the figure shows two reconstructed jets. Adding a soft particle (low p_T) into event that can be seen in the right side influenced the result of the jet reconstruction in terms of number, axis direction or shape of jets.

- Collinear safety: Let us assume two particles moving together, which mutual distance is short and have smaller energy than other particles in arising jet. They can be detected together as a one track or in one tower of the detector. In this case detector considers them as one signal and the final jet could be reconstructed incorrectly or not at all. If the jet algorithm is not influenced by this effect, this characteristic is denoted collinear safety.

- Maximal reconstruction efficiency - all relevant jets are reconstructed.

- Efficient use of computer resources and time: Because of the enormous amount of data, especially in heavy-ion collisions, the jet algorithm should provide jet identification with a reasonable computing time.

3.5   Classes of jet algorithms

During the years many types of jet algorithms were developed, which differ from each other in some attributes and in their scheme of jet finding. These attributes are: sequence of steps to find a jet, initial energy and momentum parameters, collinear and infrared safety, boundary sensitivity and sensitivity to non-perturbative effects,
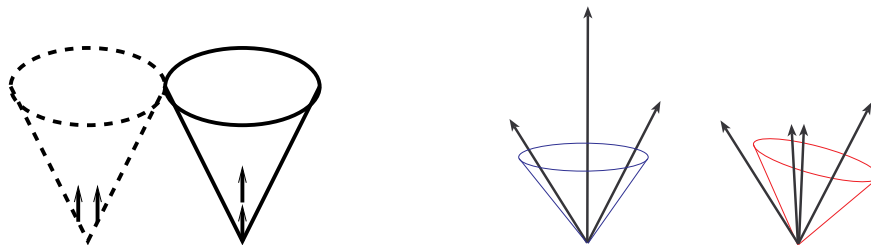
Figure 3.5: Illustration of collinear safety of a jet algorithm. According to the figure, if two particles move together and the distance between them is small the detector can registered them as a one signal instead of two independent signal. This can affect the properties or even existence of jets. [39].

e.g. hadronisation and underlying event contamination. According to the selection of a starting particle, jet algorithms can be classified to seedless and seeded that start by choosing the most energetic particle in the event, which is called a seed. The seedless jet algorithm looks for all stable solutions of jet from all entries without choice of any seed. Moreover, jet algorithms can be divided into two groups: cone and sequential recombination algorithms.

3.5.1 Cone Algorithms

Seed cone Algorithm

The cone algorithm[41] assumes that particles of a jet show up in a cone around a direction of dominant energy flow. The vertex of the cone is in the location of the parton-shower beginning of the original parton. The cone algorithm starts by drawing a circle of a specific radius $R = \sqrt{\Delta\eta^2 + \Delta\phi^2}$ (where R is a radius of a cone, η is pseudorapidity and ϕ is azimuthal angle) in $\eta - \phi$ plane around the highest p_T or the most energetic particle of the collision, which is called a seed. Then the total transverse momentum and energy is computed as the sum of energy and momenta of all particles located inside the circle in $\eta - \phi$ defined by the cone. This leads to the formation of a proto-jet. If a proto-jet does not intersects any other, the proto-jet is proclaimed as a final jet. For the jet it is important that the jet's momentum vector is aligned with the axis of the cone. But if the difference between axis of the cone and jet's momentum vector is larger than determined criterion then it is necessary to recalculate the momentum. Then algorithm checks if it is now aligned with the center of the cone and if not, the process is repeated until they are aligned. This iteration process is called stabilization.

After stabilization of jets, a procedure of splitting or merging is needed to be run, because areas of jets can overlap. Two jets will be merged if the percentage of shared transverse energy of the lower p_T jet is usually larger than 50% (but this value can be defined by the user), otherwise they are split [39].

The cone algorithm is very fast and simple. Although the main disadvantage of the cone algorithm is that it does not behave as a collinear and infrared safe algorithm.

SISCone algorithm

The seedless infrared safe algorithm (SISCone) is the next cone algorithm, which we discuss here, but in comparison to cone, SISCone is infrared and collinear safe. The main aim of this algorithm is also to identify all circular enclosures - cones and test their stability. Its basic steps are described and depicted in Figure 3.6 as follows [42]:

1. A circle of radius R around a point, which represents a particle is put into an event in $\eta \times \phi$ plane.

2. The circle is moved in a random direction and until the edge of the circle hits a point outside the circle.

3. The circle is rotated around the boundary point until another one touches the edge of the circle.

4. The procedure above is repeated until all points in nearby area of starting points are included.

5. All particles defined by pairs of edge points form a jet.
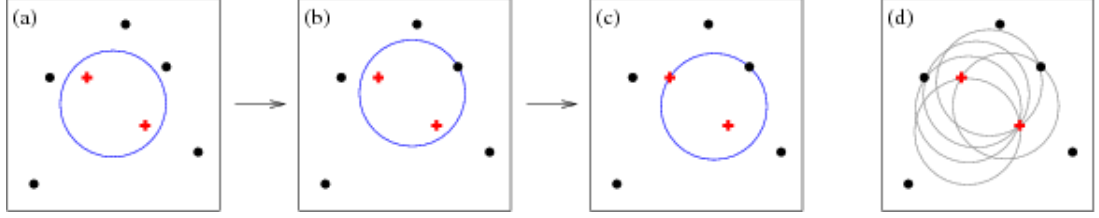
Figure 3.6: Scheme of the SISCone algorithm [42].

3.5.2 Sequential recombination algorithms

The sequential recombination algorithms have become in the last years the main tool for analysing data from high energy collisions. In comparison to the cone algorithms, sequential recombination algorithms are based on specific selection of a starting particle and then sequentially add other particles that are close enough to the arising jet. Their advantage is that they are collinear and infrared safe and thus results are more reliable. But their disadvantage is relative slowness in high multiplicity environment.

   This class of jet algorithms starts with a list of preclusters and empty list of jets. Preclusters are our input to the jet reconstruction and they represents tracks and towers measured by a detector. Initially a vector $(E, \vec{p} = E(1, \cos\phi\sin\theta, \sin\phi\sin\theta, \cos\theta))$ is assigned to each precluster, where E is the energy of the precluster, ϕ is the azimuthal angle and θ is the polar angle with respect to the beam axis. Then the square of transverse momentum p_T^2 is calculated for each precluster.

In order to find final jets from preclusters, the algorithm implements several steps outlined bellow [39]:

1. The sequential recombination algorithm begins with a definition of distances d_i and d_{ij}:

   - For each precluster i in the list, define distance from the beam

   $$d_i = p_{T,i}^{2n} \tag{3.1}$$

   For each pair (i, j) of preclustes $(i \neq j)$, define distance between i and j

   $$d_{ij} = min(p_{T,i}^{2n}, p_{T,j}^{2n})\frac{\Delta_{ij}^2}{D^2} \tag{3.2}$$

   where $\Delta^2 = (y_i - y_j)^2 + (\phi_i - \phi_j)^2$ and p_{Ti}, y_i, ϕ_i are respectively the transverse momentum, rapidity and azimuth of the precluster i. For each particle the transverse momentum is defined as:

   $$p_{Ti} = \frac{E_i}{c}\sin\theta_i \tag{3.3}$$

where θ_i is an angle between the direction of a particle and the beam of colliding nucleons. R is a resolution parameter that represents size of a jet and the minimum distance between two pairs of jets i, j. Typical value of R used in data analysis is 0.2 to 1.0. Larger R of jet covers larger area and more energy of original parton, but it is more sensitive to the background. Parameter n governs the relative power of the transverse momentum versus geometrical (Δ_{ij}) scales. Different values of $n \in -1, 0, 1$ correspond to three sequential recombination algorithms: k_T ($n = 1$), anti-k_T($n = -1$) and Cambridge/Aachen ($n = 0$), which will be discussed later.

2. After computation of all distances d_i, d_{ij} and excluding values below a jet resolution threshold d_{cut}, the minimum of them is found and labeled as d_{min}.

3. The next step of the algorithm depends on the value of d_{min}:

   - If d_{min} is a d_{ij}, preclusters i and j are removed from the list and replaced by a new merged precluster: $p_{ij} = p_i + p_j$ and $E_{ij} = E_i + E_j$

   - If d_{min} is a d_i, the corresponding precluster can not be merged and it is removed from the list of preclusters and add to the list of jets.

4. If any preclusters remain, values d_{min} are calculated again and the whole process of jet finding is repeated. It can happen that a jet overlaps with another one, then the common area is assigned to the jet with higher transverse momentum.

In general, all jet sequential recombination algorithms are infrared and collinear safe.

As was said before, there are three sequential recombination algorithms: k_T, anti-k_T and Cambridge-Aachen and their main characteristics are as follows:

k_T algorithm

The k_T algorithm recombines first particles with low p_T close to each other in space. This fact implies that k_T algorithm prefers soft particles and thus it is sensitive to soft background. Use of the k_T algorithm in heavy-ion collisions might cause problems because if we compare jet reconstruction in a hard event without background to an event with added soft particles, resulting jets will be different. Not only the energy of jets is higher due to energy of soft background, but also jet shapes are changed and are less regular. This feature is called back reaction [43]. Therefore the k_T algorithm is usually used for estimation of background. A scheme of k_T algorithm jet reconstruction is depicted in Figure 3.7.

anti-k_T algorithm

The anti-k_T jet finding algorithm belongs to a class of jet sequential recombination algorithms, where the the parameter $n = -1$ in equation (1). It acts as an idealized cone algorithm [43], because reconstructed jet shapes are regular and quite circular. Unlike the k_T algorithm, the anti-k_T algorithm is resilient to the soft background, since it clusters first particles with the highest p_T. Soft particles are connected to
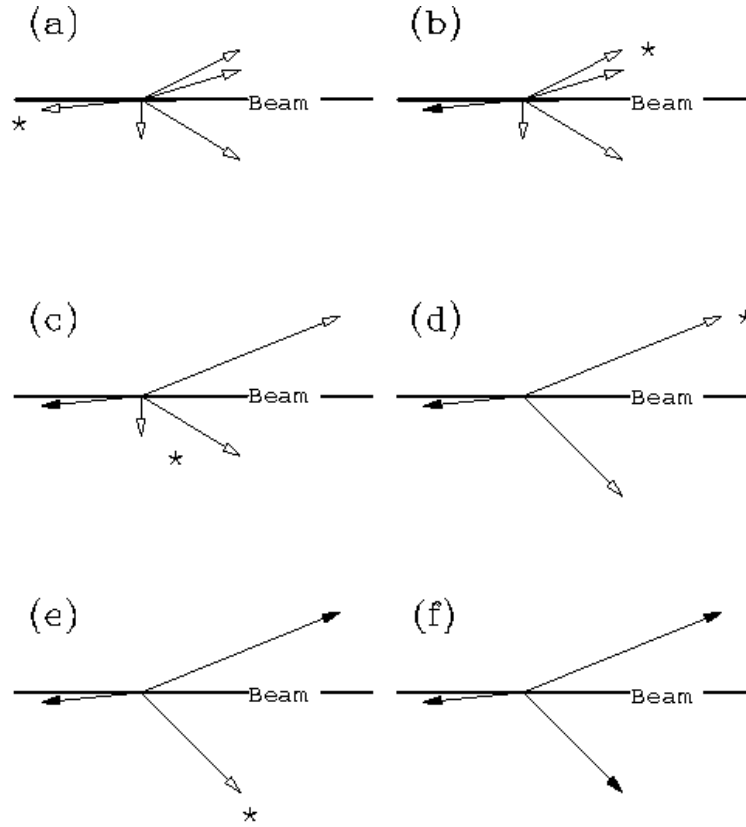
Figure 3.7: A scheme of k_T algorithm [39]

hard one before recombination among themselves. This leads to the high suppression of the effect of the back reaction. The anti-k_T algorithm is currently the most used for jet analysis.

Cambridge/Aachen algorithm
For this algorithm value of the parameter n in equation (1) is 0. It means that momentum of particles is not taken into consideration at all, therefore recombination is based only on spatial separation.

It is also important to mention, that each algorithm has specific computing time. Comparison of speed, infrared and collinear safety of jet algorithms is given in Table 3.1. We can see that the fastest algorithm is the Cone, but in comparison to other algorithms its disadvantage is infrared and collinear unsafety. SISCone and sequential recombination algorithms are slower, but they are effective and reliable in data analysis. Computation time of jet algorithms is compared in Figure 3.8.

3.6   Jet areas

Jet area is a measure of susceptibility of a jet to soft radiation (underlying event, pileup), that is uniformly distributed in rapidity and azimuth around the jet. Jet

Algorithm	Speed	Infrared safety	Collinear safety
Cone	N	no	no
SISCone	$N^{3/2}$	yes	yes
k_T	$N \ln N$	yes	yes
anti-k_T	$N \ln N$	yes	yes
Cambridge-Aachen	$N \ln N$	yes	yes

Table 3.1: Comparison of speed, infrared and collinear safety of jet algorithms, where N is a number of reconstructed particles in the event [44].
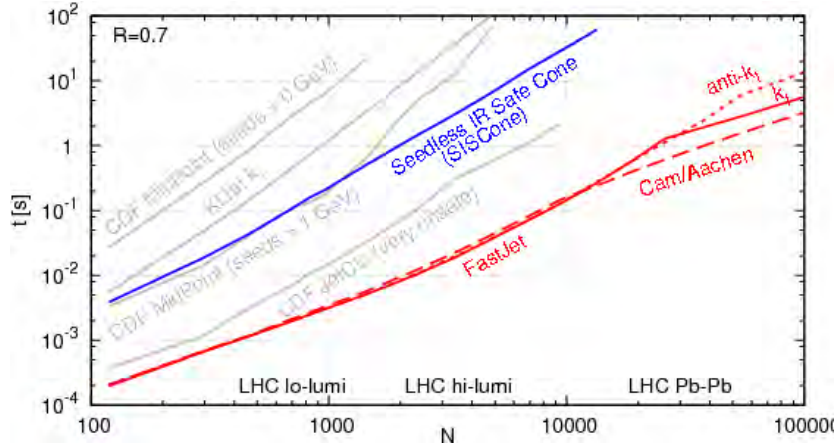
Figure 3.8: Timings for the clustering of a simulated 50 GeV di-jet event as a function of number of particles in the event with Monte Carlo simulator PYTHIA) [44].

areas are used for subtraction of the jet contamination by soft radiation. There are two main definitions of jet area: passive and active [45]:

- **Passive area**: it is a measure of the susceptibility of the jet to pointlike radiation. To determine the passive area a single ghost particle is added to the event. Then the region in which a single ghost is clustered within a jet is defined as a passive area. The passive area geometrically equals to πR^2.

- **Active area**: a dense coverage of soft ghosts g_i each with an infinitesimal p_T, randomly distributed in rapidity and azimuth with density distribution per unit area ν_g is added to the event. Ghosts might cluster with each other and also with hard particles. Because of infrared insensitivity of jet algorithm, the addition of ghosts does not influence the shape or the momenta of the final jet. The number of ghosts in a jet is used as a measure of jet area. In comparison to the passive area, which has shape of a circle, the structure of the active area is more complicated.

In Figure 3.9 different area structures of the same event reconstructed by 3 sequential recombinations algorithms k_T, anti-k_T, Cambridge/Aachen and SISCone can be
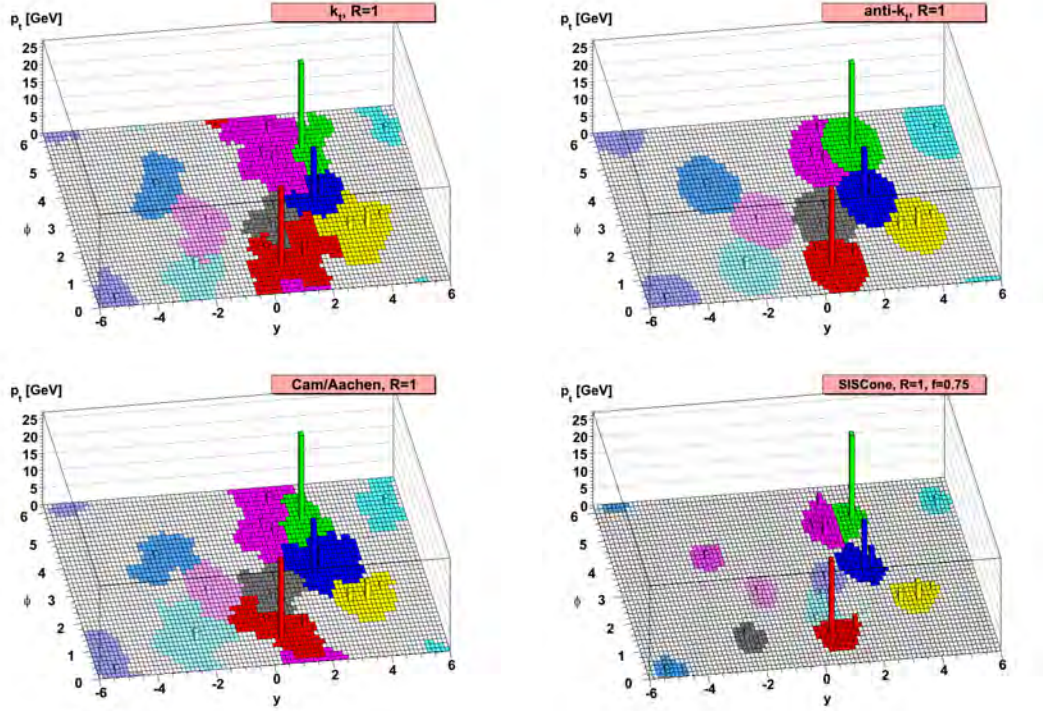
Figure 3.9: Comparison of jet areas in the same event reconstructed by k_T, anti-k_T, Cambridge/Aachen and SISCone algorithm. [43]

seen. Area of anti-k_T jets is circular, because jets are reconstructed in the radius R around the high p_T particle. k_T jets has irregular shape, due to first reconstruction of high number of close low p_T particles.

3.7 FastJet

The FastJet package [46] is a powerful software package used for jet analyses. It has been written in C++ by Matteo Cacciari, Gavin Salam and Gregory Soyez and includes a broad range of jet analysis tools. FastJet provides implementations of all commonly used jet sequential recombination algorithms such as k_T, anti-k_T and Cambridge/Aachen jet finders. It can be extended by SISCone and other cone algorithms via plugin. FastJet also includes tools for calculating jet areas, performing background estimation of pileup and underlying events, background subtraction and for jet substructure analyses [46].

3.8 Jet background

A critical issue of each jet analysis is the background, mainly in high multiplicity environment of heavy-ion collisions. A large amount of soft (low p_T) particles is produced which do not originate from the initial hard scattering and during jet reconstruction they might end up in a jet and modify jet p_T [44]. These low p_T particles are roughly uniformly distributed in η-ϕ space and they originate in several

sources [47]:

- Underlying event - products of interactions between hadron remnants that are produced in heavy-ion collisions. Underlying event also includes multi-parton interactions and initial and final state radiations.

- Pileup - multiple nucleon-nucleon interactions created by crossing bunches of particles in an event.

To acquire true jet p_T, it is important to subtract soft component of p_T from jets. The process when a background is subtracted from measured jets is called decontamination of a jet and it is carried out after all jets are found. The transverse momentum density of background ρ is estimated by using concept of active jet areas [48] as follows [10]:

$$\rho = \text{median}\left(\frac{p_{T,i}}{A_i}\right) \tag{3.4}$$

where i runs over all reconstructed jets with transverse momentum $p_{T,i}$ and area of jet A_i in the event. For the median of background energy density ρ calculation the k_T algorithm is used for jet finding, because it is infrared safe and more sensitive to soft particles than anti-k_T algorithm.

Then an event-by-event correction is provided for each jet with p_T from which the median of jet energy density multiplied by the jet area A is subtracted:

$$p_{T,corr} = p_{T,uncorr} - A\rho \tag{3.5}$$

3.9 Jet reconstruction at STAR and ALICE

Jet identification in heavy ion collisions at RHIC is extremely challenging task due to background fluctuations which are comparable to signal. In comparison to jet reconstruction at the LHC, jet identification at the LHC is simpler, because jets dominate over the background and especially at high p_T it is possible to clearly identify a jet.

One of the first attempts to perform full jet reconstruction in the environment of heavy-ion collisions was in the analysis of central Au+Au collisions at $\sqrt{s_{NN}} = 200$ GeV collected in the 2007 RHIC run. Total number of analyzed minimum bias events was 7.6 M. Jets were reconstructed from jet constituents (charged tracks and neutral energy towers) with p_T higher than $p_{T,min} = 0.2$ GeV. After jet reconstruction, background mean energy density in each event was estimated to $\rho = 75$ GeV and this energy was subtracted from each jet according formula: $p_{T,corr} = p_{T,uncorr} - A\rho$, where A is jet area and jet spectra corrected for background was obtained [49]. The left part of Figure 3.10 presents differential cross section for fully reconstructed inclusive jet production in the most central (0-10%) Au+Au collisions. Figure 3.10 shows the jet R_{AA} which is the ratio of the jet production in the most central (0-10%) Au+Au and jet production in p+p collisions (collected in Run 6) scaled by binary collisions. Measured jet R_{AA} for $R = 0.2$ jets is more suppressed than R_{AA} for $R = 0.4$ which is compatible with the unity, within large systematic uncertainties. This fact could indicate jet broadening in heavy-ion collisions. There is a difference between algorithms due to their different response to the heavy-ion background.The

anti-k_T algorithm is more resilient to the background than the k_T. This result is inconclusive and for its improvement higher statistics is necessary to suppress the uncertainties.
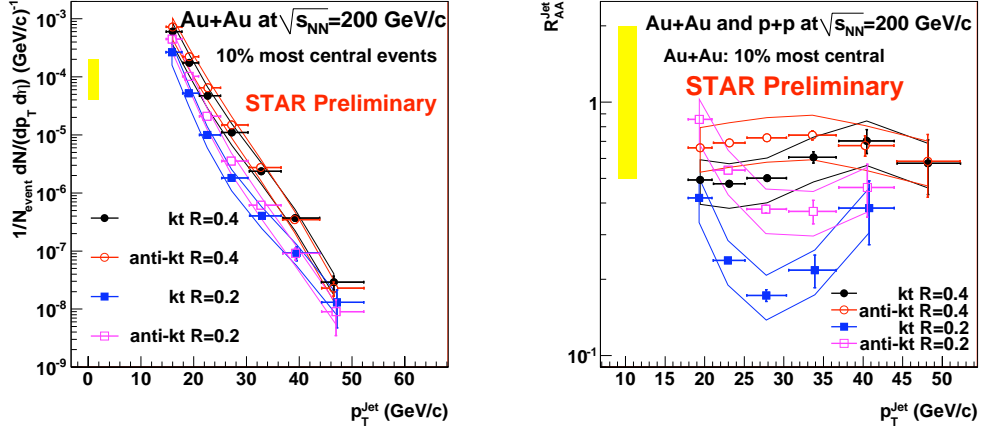
Figure 3.10: Cross section for inclusive jet production (left) and jet R_{AA} (right) in Au+Au collisions at $\sqrt{s_{NN}}$= 200 GeV [49].

The RHIC Run 11 in comparison to previous runs provides higher statistics, therefore results are more promising due to the suppression of systematics errors. Figure 3.11 presents the first quantitative comparison of jet quenching at RHIC and the LHC. It shows corrected charged semi-inclusive recoil jet spectrum for central 0-10% and peripheral collisions 60-80%. In each event, one trigger hadron was randomly selected from all charged tracks with $p_T > 9\,\mathrm{GeV}/c$. The cut for maximum track p_T was 30 GeV/c. Jets were reconstructed by the anti-k_T algorithm with the resolution parameter $R = 0.3$ and the jet area cut $A > 0.2$. Jet acceptance is $|\eta| < 1 - R$. Background was subtracted by the method described in the previous section.

Figure 3.11 mainly compares the jet nuclear modification factor for central and peripheral Au+Au collisions at $\sqrt{s_{NN}} = 200$ GeV for the jet resolution parameter $R = 0.4$ with the result which was carried out by the ALICE collaboration in Pb+Pb collisions at $\sqrt{s_{NN}} = 2.76$ TeV for $R = 0.4$. The lower panel on the left side shows I_{CP} which is the ratio of central to peripheral distributions. At low p_T the I_{CP} is close to 1. But for $p_{T,jet} > 10$ GeV/c, significant jet yield suppression $I_{CP} \approx 0.2$ can be observed in central collisions. The $p_{T,jet}$ shift between central and peripheral collisions is -6.3 $\pm$ 1.4 GeV/c in the range $10 < p_{T,jet} < 20$ GeV/c. This means that jet spectrum in central collision contains more hard jets than in peripheral collision. The suppression at STAR is larger in comparison to the LHC energy at $\sqrt{s_{NN}} = 2.76$ TeV [50], where the nuclear modification factor I_{AA} is approximately 0.6 and $p_{T,jet}$ shift is about -8 $\pm$ 2 GeV/c in the range $60 < p_{T,jet} < 100$ GeV/c. The low right panel shows ΔI_{AA} which is the ratio of the yield of recoil charged jets in Pb+Pb collisions to that in PYTHIA p+p collisions. It is important to mention that analysis was performed with slightly different measurement techniques.

Figure 3.12 [52] presents corrected and unfolded spectrum of inclusive charged
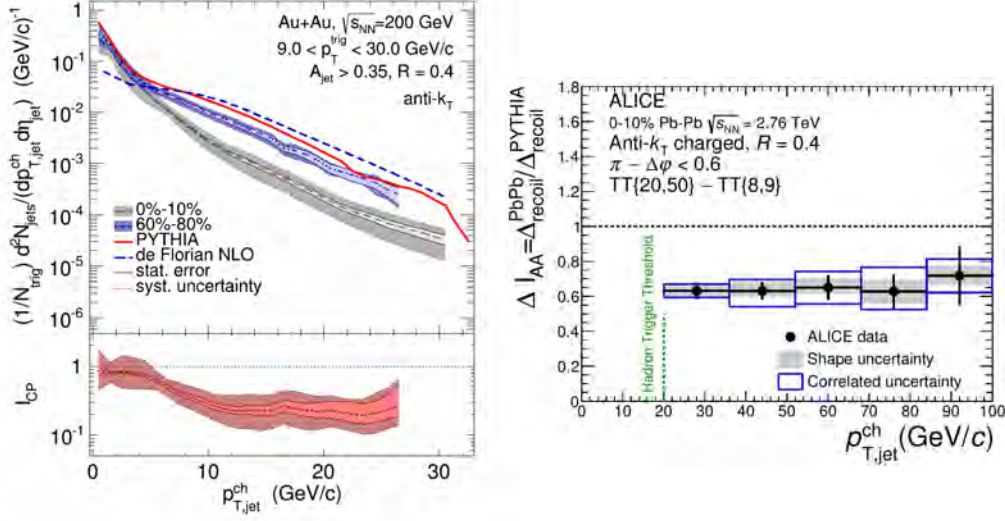
Figure 3.11: Left: Charged recoil jet spectrum for central and peripheral collisions $R = 0.4$ together with the nuclear modification factor I_{CP} [51]. Right: ΔI_{AA}, the ratio of recoil jet yields Δ_{recoil} in Pb+Pb and PYTHIA p+p collisions at $\sqrt{s} = 2.76$ TeV for $R = 0.4$ [50].

jets for R=0.2 and 0.3 in central 0-10% Au+Au collisions at $\sqrt{s_{NN}} = 200$ GeV in Run 11. Jets were reconstructed by the anti-k_T algorithm which used charged tracks from the STAR TPC. Track cut $p_T > 200$ MeV/c was applied. Jet acceptance is $|\eta| < 1 - R$, jet area cut for the resolution parameter $R = 0.2$ is $A > 0.09$ and for $R = 0.3$ is $A > 0.2$ and cut on p_T of the leading hadron in jet is 5 GeV/c. Background was subtracted by the method mentioned in the previous section and jet spectrum is corrected to detector effects.

The result of the analysis of full jets carried out at the ALICE experiment can be found in Figure 3.13 which presents unfolded spectra of $R = 0.2$ jets with a leading track requirement of 5 GeV/c in p+p and 0-10% and 10-30% central Pb+Pb collisions. Cut on p_T of the leading track was applied in order to suppress jets constructed from the combinatorial background. Jets were reconstructed by anti-k_T using charged tracks detected by ITS and TPC and neutral energy towers of EMCal as jet constituent candidates. Jet spectra were corrected to mean background energy, background fluctuations and detector effect. Background fluctuations were determined by (1) embedding a single particle in the event and inspecting the anti-k_T jet that contains the embedded particle, and by (2) random-cone method in which the scalar sum of the p_T of all particles found in a cone randomly placed in the event was taken. The second method was used for calculation of the response matrix that was then multiplied with the detector matrix and resulting matrix was used in unfolding procedure. Unfolding methods utilized for correction of full spectra are SVD unfolding and χ^2 minimization method.

Figure 3.14 shows the nuclear modification factor R_{AA} that is defined as a ratio of full jet spectra in Pb+Pb and p+p collisions taken as a reference. R_{AA} was found
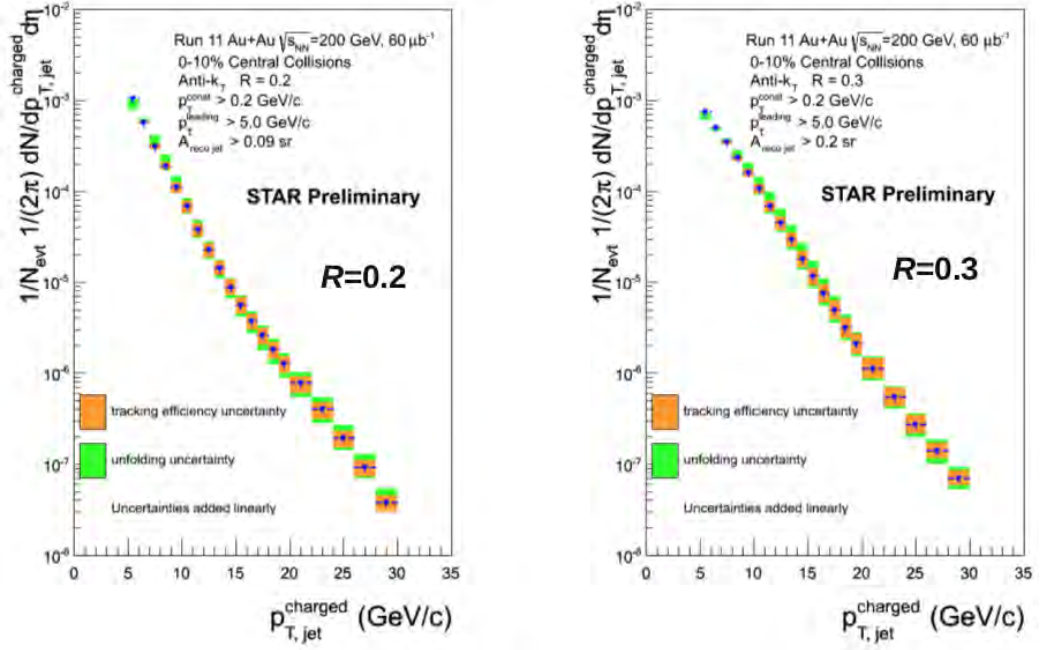
Figure 3.12: The corrected spectrum of inclusive charged jets in central Au+Au collisions at $\sqrt{s} = 200$ GeV for R=0.2 and 0.3 [52].

to be 0.28 ± 0.04 in 0-10% and 0.35 ± 0.04 in 10-30% collisions, independent of jet p_T within the uncertainties of the measurement. These results qualitatively agree with the suppression obtained from measurements using charged-particle jets and are consistent with the R_{AA} measured by the ATLAS experiment.

Analysis of jets presented in the next chapter is very similar with last two analyses described above and uses almost same procedures and techniques for obtaining corrected jet spectra. The charged jet analysis in [52] is parallel to the analysis of charged and full jets in 2014 RHIC run, which is the main part of this diploma thesis. The RHIC Run 14 in comparison to Run 11 provides approximately 5 times higher statistics, therefore results will be more promising. The increase of statistics enables more precise study of the jet R_{AA} as a function of centrality, it also suppresses systematics errors and can provide new insights to background fluctuations in high multiplicity environment of high energy heavy-ion collision.
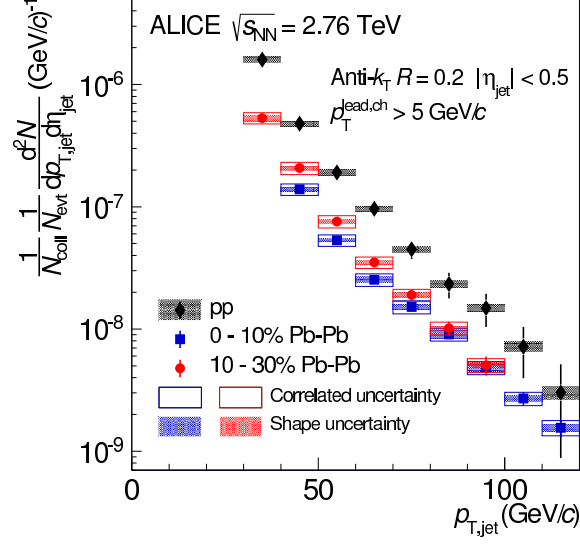
Figure 3.13: Jet spectra of $R = 0.2$ jets with a leading track requirement of 5 GeV/c in 0-10% and 10-30% central Pb+Pb collisions scaled by $1/N_{coll}$ and in inelastic p+p collisions at $\sqrt{s_{NN}} = 2.76$ TeV [53].
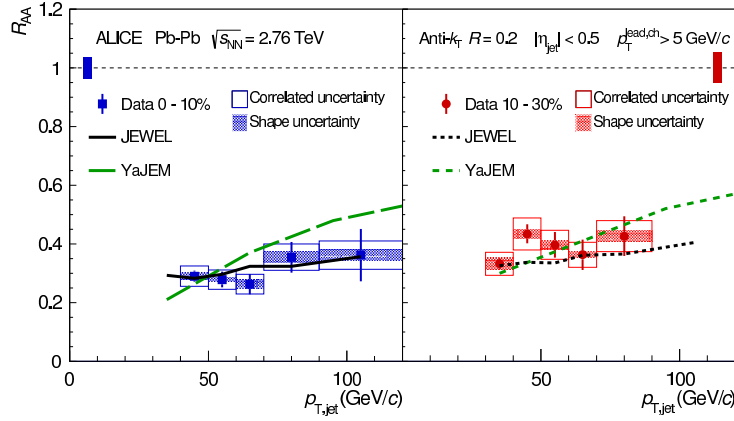
Figure 3.14: R_{AA} for $R = 0.2$ jets with the leading track p_T cut of 5 GeV/c in $0-10\%$ (left) and 10-30% (right) central Pb+Pb collisions at $\sqrt{s} = 2.76$ TeV compared to calculations from YaJEM and JEWEL [53].

Chapter 4

Analysis of jets

The main aim of this diploma thesis is the reconstruction of charged and full jet spectra produced in Au+Au collisions at the center of mass energy $\sqrt{s_{NN}}$= 200 GeV and study of their properties. From our point of view the term "charged jets" means that we reconstruct jets using charged tracks (pions, kaons, protons) while "full jets" are composed from charged tracks (pions, kaons, protons) and signal of towers in the calorimeter.

Charged tracks were measured by the Time Projection Chamber (TPC) and energy deposited in towers by Barrel ElectroMagnetic Calorimeter (BEMC) of the STAR detector. The analysis consists of following steps:

- Event selection

- Track quality cuts

- Study of data quality assurance, response of the BEMC and its time stability

- Application of sequential recombination algorithm anti-k_T on data as a function of the centrality as well as the resolution parameter R to create uncorrected jet spectra

- Background subtraction and the study of its influence on the jet spectra

- Jet area cut study

- Comparison of uncorrected charged and fully reconstructed jet spectra in different centralities, for different resolution parameters R and with p_T cuts on leading hadron of the jet

- Embedding a single particle into real event to determine background fluctuations, evaluation of δp_T

- Construction of response matrix using background and detector matrix

- Bayes' unfolding

4.1 Data sample and event selection

Data used for this analysis are from Au+Au collisions at $\sqrt{s_{NN}} = 200$ GeV. The data sample was collected in 2014 in RHIC Run 14 by the STAR detector in about 13 weeks resulting in approximately 2 billion events. Raw data measured directly by detectors are after processing transformed to muDST files. MuDST files contain all data that were produced and are available and suitable for data analysis. But their analysis is more time-consuming due to their large size. Therefore the size of muDST files is reduced by creating of picoDST files. PicoDST are smaller data files containing only information interesting for our analysis e.g. selected events with required triggers or information from the TPC, the BEMC, the VPD, etc. Each event is labeled by a set of trigger numbers that summarizes properties of an event. We select only minimum bias events that are events with as little bias as possible. In total, about 1.6 billion events with minimum bias (MB) trigger were recorded. Trigger identification numbers (ID) for minimum bias events are 450005, 450015, 450025, 450050 and 450060.

Listed triggers are labeled with an attribute "protected" that means we use only events without pile-up of other events. Pile-up is a contamination of products of one event in another one and the reason of its origin is a fact that the frequency of collisions was higher than TPC readout time. For further analysis we use only 1.1 billion evens; almost 300 million events are not taken into account due to the initial problems with HFT tracking that influenced properties of tracks and the relevant correction is not yet available. The second reason of excluding first days of data taking is an increased rate of non-functional BEMC sectors than later in the rest of physics runs in 2014. In Run 14 approximately 1600 of physics runs (time of data taking when detectors are calibrated and its set-up should remain stable) are available. About 400 of them were however labeled as bad runs and excluded from the analysis due to problems mentioned above or they did not pass our imposed quality requirements.

Figure 4.1 shows a distribution of the z-position of the primary vertex of all events. The primary vertex is a point where a collision happens and it is determined from fitting of TPC charged global tracks. For the analysis we selected only events for which the longitudinal distance (z-axis direction) between the primary vertex and the center of the detector is less than 6 cm and difference in determination of z-vertex by TPC and VPD is less than 3 cm as indicated by vertical lines in Figure 4.1. Position of the primary vertex in perpendicular plane to the beam direction is restricted to be 2 cm from the center of the STAR detector: $\sqrt{x_{vertex}^2 + y_{vertex}^2} < 2$ cm.

According to measured reference multiplicity of charged particles N_{ch} in $|\eta| < 0.5$, events are sorted into several centrality bins. The centrality was determined using the StRefMultCorr class. The relation between the value of charged-particle reference multiplicity within $|\eta| < 0.5$ and centrality of a collision can be found in Table 4.1 as well as in Figure 4.2, in which we can see also the relation between number of events and the value of reference multiplicity or centrality class.
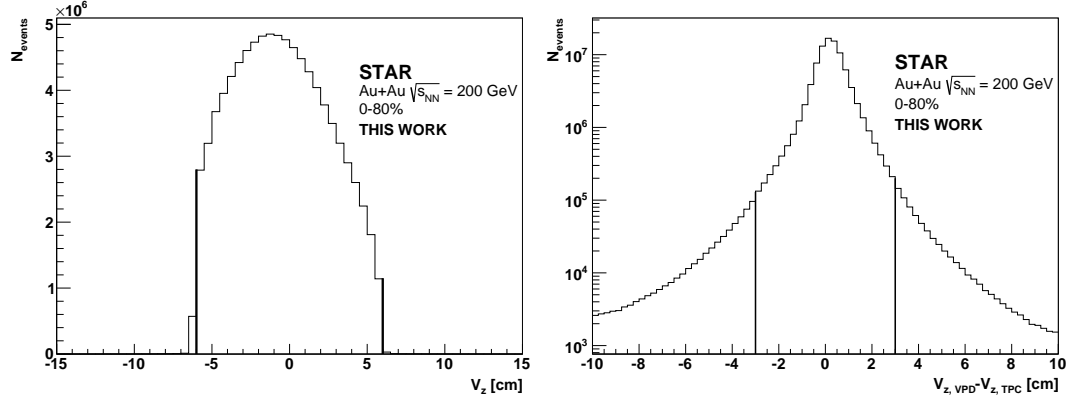
Figure 4.1: Left: Distribution of the z-position of the primary vertex of all events with the cut $|V_z| < 6$ cm. Right: Distribution of the difference between determination of the primary vertex by the VPD and the TPC with cut $|V_{z,VPD} - V_{z,TPC}| < 3$ cm.

Centrality class	Fraction of $\sigma/\sigma_{\mathbf{geo}}$	Reference multiplicity $\mathbf{N_{ch}}$ in $|\eta| < 0.5$
most central	0-10 %	>376
central	10-20 %	266-376
semi central	20-40%	119-266
semi peripheral	40-60%	41-119
peripheral	60-80%	10-41

Table 4.1: Centrality classes and centrality bins as a fraction of σ/σ_{geo} in Au+Au collisions at $\sqrt{s_{NN}} = 200$ GeV according to charged-particle reference multiplicity N_{ch} in Run 14.

4.2 Charged track quality selection

This analysis uses global charged tracks measured by the TPC of the STAR detector. Global tracks are determined from helix fit of track points in the TPC and the HFT (if it is available). STAR tracking software also produces primary tracks that are tracks fitted with additional point of the primary vertex of a collision. Usage of primary tracks for jet analysis would be more physically correct because we are restricted only to tracks originated mainly from the hard scattering while global track list in the event includes also tracks originating from secondary vertices of decaying particles. Figure 4.5 shows a comparison of primary and global track p_T distributions. Unfortunately, decrease of primary-track p_T spectrum is more rapid than global track p_T spectrum. The number of global tracks is always larger than primary track number in each event, but we would expect this in number of low-p_T particles. Number of high-p_T tracks should be unchanged, all of them originate in the hard scattering in the primary vertex. Usage of primary tracks would significantly reduce statistics of jets at high p_T, therefore we use only global tracks. As was
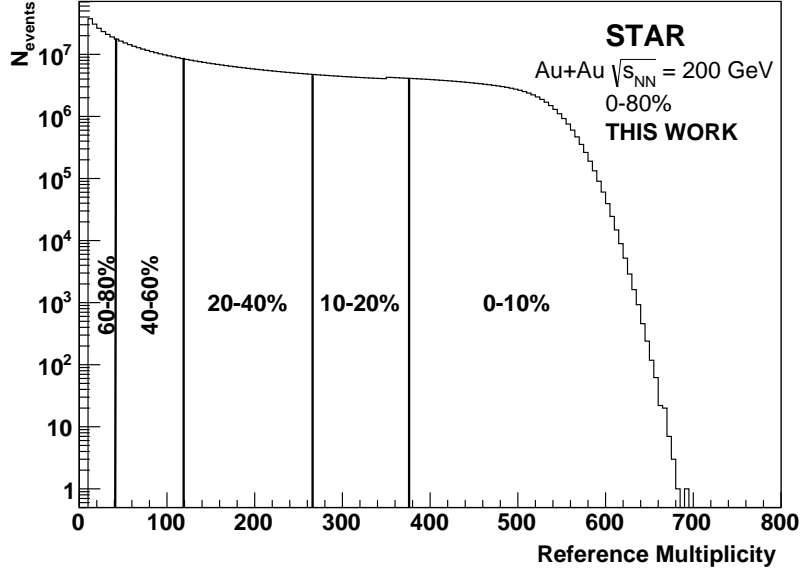
Figure 4.2: Distribution of the charged-particle multiplicity for $|\eta| < 0.5$ in Au+Au collisions at $\sqrt{s_{NN}} = 200$ GeV in Run 14 are together with centrality classes definition defined by vertical lines.

said before, tracking algorithm uses information from the TPC and the HFT if it is available. This causes a problem, because in the unfolding procedure and detector matrix response construction we need to know also the HFT efficiency to correct jet spectra, which is not yet available. In Figure 4.5 we can see the difference between tracking using only the TPC and the TPC with the HFT. The efficiency of the TPC with the HTF is slightly lower than the efficiency of the TPC only.

For our analysis following track cuts are imposed:

- distance of the closest approach of the track to primary vertex: DCA < 1.0 cm, depicted in Figure 4.3 in the left.

- number of track fit points $N_{fit} \leq 15$. Maximum number of fit points in the TPC is 45 (eventually 49 if all layers of the HFT are available).

- ratio of number of track points in the TPC to maximum number of track points: $\frac{N_{fit}}{N_{max}} = 0.52$.

- pseudorapidity selection $\eta < 1.0$

For this analysis only tracks above $p_T = 200$ MeV/c are taken into jet reconstruction, because hadron tracking efficiency is very low below this value. Estimated single hadron tracking efficiency in central Au+Au collisions for Run 11 is depicted in Figure 4.6. We assume that the performance of the TPC during Run 14 is the same as in Run 11. The tracking efficiency was determined via embedding of simulated tracks into real events. Embedding is a technique for estimation of track momentum resolution. A simulated track with known p_T is created and put into real event -

high track density environment and momentum smearing effects on embedded track are studied. We use this approach to correct tracks because full simulation (e.g. in GEANT) of the TPC instrumental response is not available.

The TPC algorithm approximates tracks by function of helix shape with a precision that is inversely proportional to the transverse momentum p_T of the particle. Trajectories of particles with increasing momentum in the magnetic field are more straight (curvature decreases), since helix parameters of each track are calculated with the larger uncertainties. Due to this fact, an upper p_T cut of 30 GeV/c for tracks is imposed. Measured track momentum is distributed around the true value with standard deviation σ that is estimated from following formula:

$$\frac{\sigma}{p_T} \simeq 0.01 \cdot p_T \tag{4.1}$$

The left panel of Figure 4.3 shows DCA distribution of accepted tracks. Peak in the first bin contains tracks with very low DCA, because they were determined very precisely with the HFT. The right side of Figure 4.3 depicts track p_T distribution in all Au+Au events which fulfill all above mentioned selection criteria. Figure 4.4 presents distributions of tracks in $\eta - \phi$ space in the TPC. There is one almost empty sector around position 5-6 rad in ϕ and -0.4-1 in η.
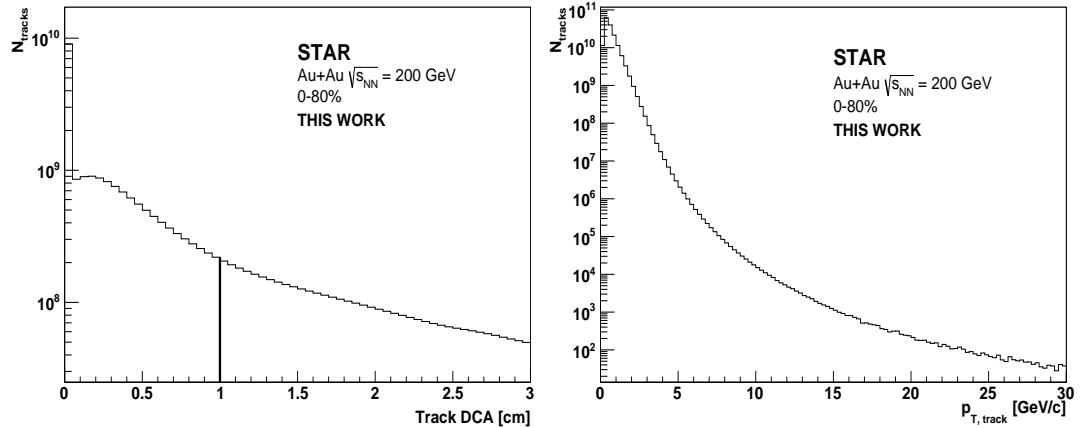
Figure 4.3: Charged track DCA cut (left) and global track p_T distribution (right) in Au+Au collisions at $\sqrt{s_{NN}} = 200$ GeV.

4.3 BEMC data quality assurance

The next step of the analysis is the study of data quality assurance of the BEMC response and its time stability. The total number of towers in the BEMC is 4800, the effective size of each tower (BEMC resolution) is 0.05 x 0.05 = $\Delta\phi$ x $\Delta\eta$. First of all η - ϕ distribution of tower E_T was studied. E_T is energy of a tower projected to the transverse direction and it is equal to p_T when $c = 1$. Runs or events in which the BEMC did not take any data or with many non-functional BEMC sectors were excluded. The first problem was found in 3 runs of all 1108 accepted physics runs of Au+Au data. Figure 4.7 shows comparison of η - ϕ distribution of tower
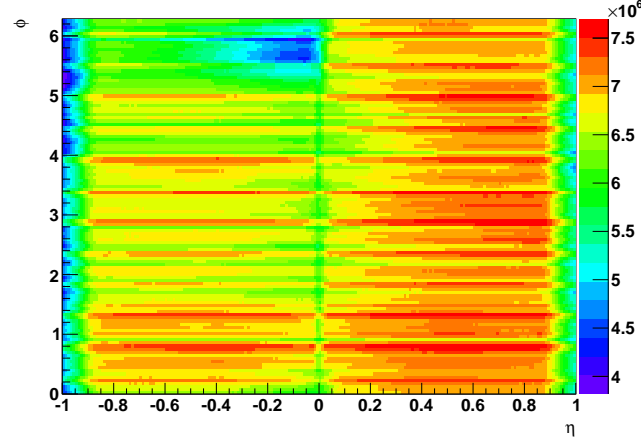
Figure 4.4: $\eta - \phi$ distribution of track position during whole Run 14
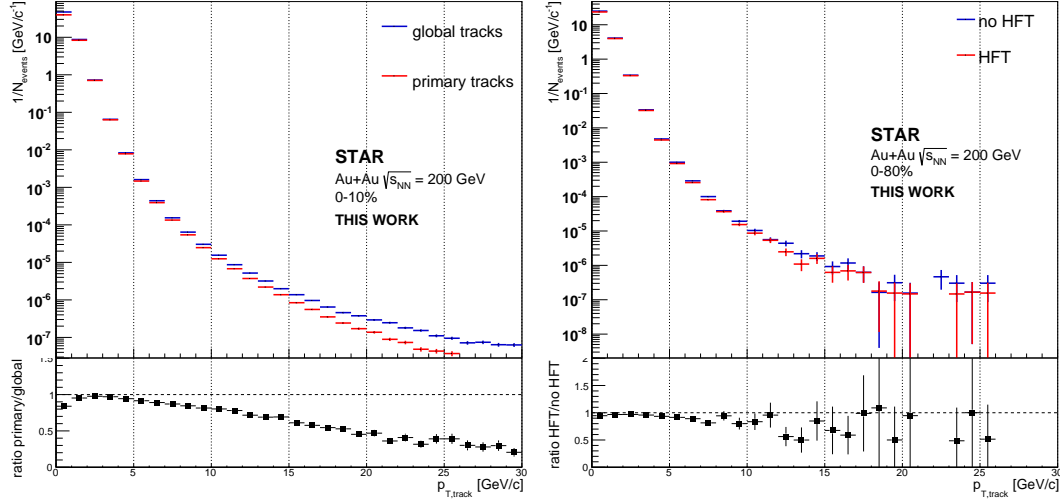
Figure 4.5: Left: Comparison of uncorrected global and primary track p_T distribution. Right: Comparison of uncorrected track p_T distributions with TPC tracking when the HFT is included or not.

E_T in the first days of Run 14 with a sample of η - ϕ distribution of tower E_T in day which is included in the analysis. Two sectors on the right side of the figure are non-functional during whole period of data-taking.

In each run, approximately 4-5% of all towers are not functional. Some towers show higher deposited energy than the mean energy of all towers in a specific period of time. Such towers are referred to as hot towers and they have to be excluded from further analysis to avoid reconstruction of jets with abnormal high E_T. Figure 4.8 shows an example of the E_T distribution for hot (left) and good tower (right).

Figure 4.9 shows energy distribution in all towers (left) and total energy deposit of all towers (right) during Run 14 before exclusion of hot towers. This figure

46
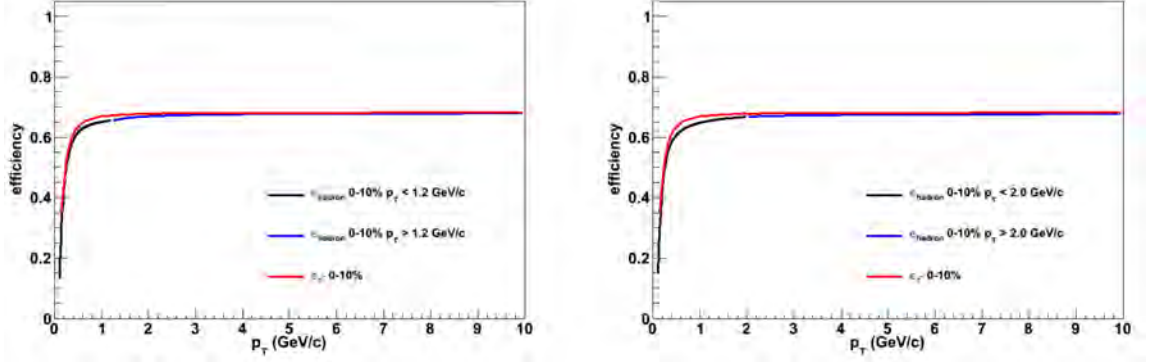
Figure 4.6: Single hadron tracking efficiency for central Au+Au collisions. Two different assumptions about proton/kaon/pion ratios were made: pp-like (left) and Au+Au-like (right) [54].
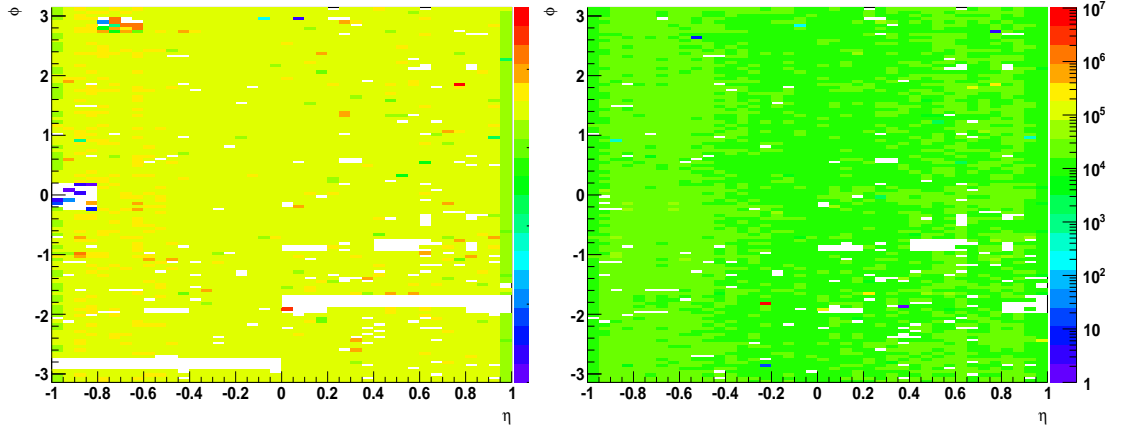
Figure 4.7: $\eta - \phi$ distribution of total tower E_T during first days of Run 14 (left) which are excluded from the analysis and a sample of $\eta - \phi$ distribution of total tower E_T (right) during day which is included in the analysis.

represents input for our BEMC performance study. We can see that the spectrum of tower energies is shifted to higher values and it contains strange peak at 30 GeV. To obtain only towers with "normal" values of energy, we use a method in which are towers in each run ordered according to their total energy deposit. The left panel of Figure 4.10 shows the distribution of all towers according to their total deposited energy during one randomly selected run with the cut on hot towers. The distribution was fitted by a Gaussian.

Then we studied several cuts on mean value of deposited energy from which the majority of hot towers is removed with a minimum losses of good-working towers. The best cut for hot tower removal was determined to be about 2.5σ of the mean total energy distribution of all towers. 4.10. For higher values of total deposited energy that correspond to 2.5σ in each run, there are more towers with higher energy
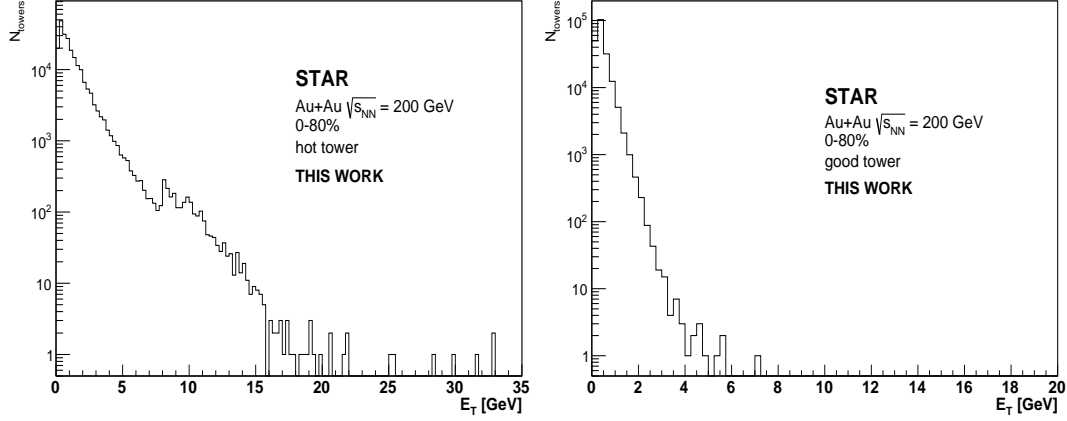
Figure 4.8: E_T distribution of hot tower (left) and good tower (right) in Au+Au collisions at $\sqrt{s_{NN}} = 200$ GeV in one physics run.
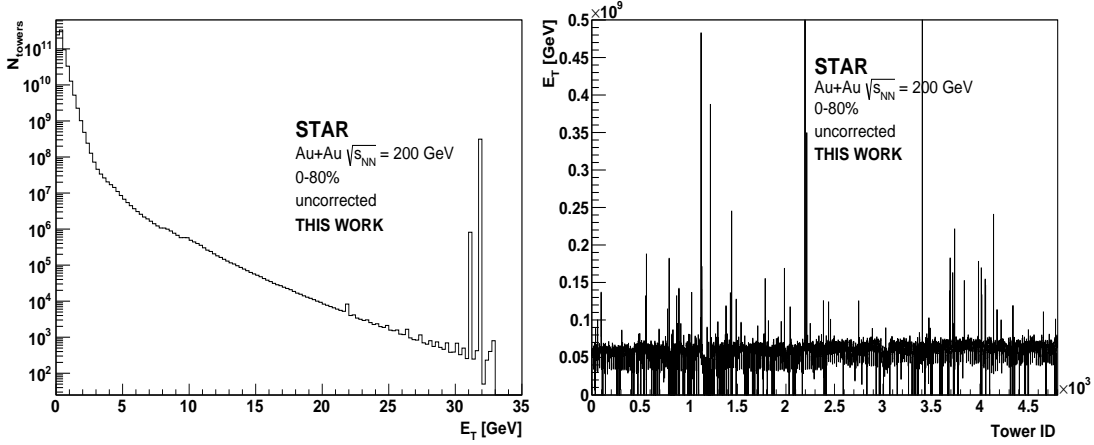
Figure 4.9: Tower E_T distribution (top) and total energy deposit in each tower (bottom) in Au+Au collisions at $\sqrt{s_{NN}} = 200$ GeV during run 14 before (left) and after (right) exclusion of hot towers.

deposit than it would be expected. Therefore towers with energy deposit above 2.5σ were labeled as hot towers and excluded from analysis. The right panel of Figure 4.10 expresses the number of physics runs, in which an individual tower was labeled as a hot tower. In other words this figure represents time stability of hot towers in all runs. Total number of physics runs is 1105 and several towers are hot during whole Run 14.

Considering the fact that each event contains different number of hot towers - the number of good and hot towers is fluctuating event by event and the list of hot towers for each run was created. The average number of removed towers in each run is usually varying from 80 to 130.

48
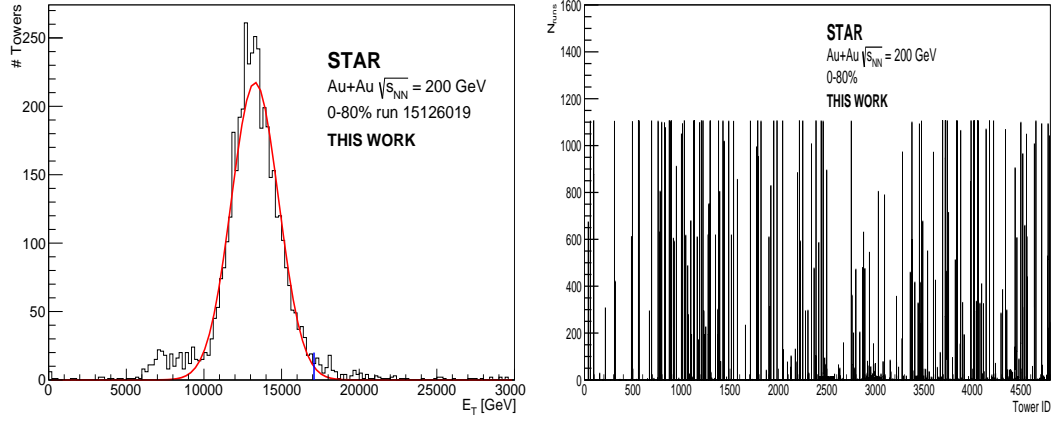
Figure 4.10: Tower ID distribution according to total deposited energy during one randomly selected run (left). The right part of figure expresses the rate of each tower in the number of physics runs, when the tower was considered to be a hot tower.

Figure 4.11 shows corrected energy spectrum of towers (left) and corrected total energy deposit of each tower in Run 14 (right). From the comparison of Figures 4.9 and 4.11 we conclude that the described method successfully excludes towers with abnormal high energy deposit and shifts E_T spectrum to lower values of energy which are closer to real ones.
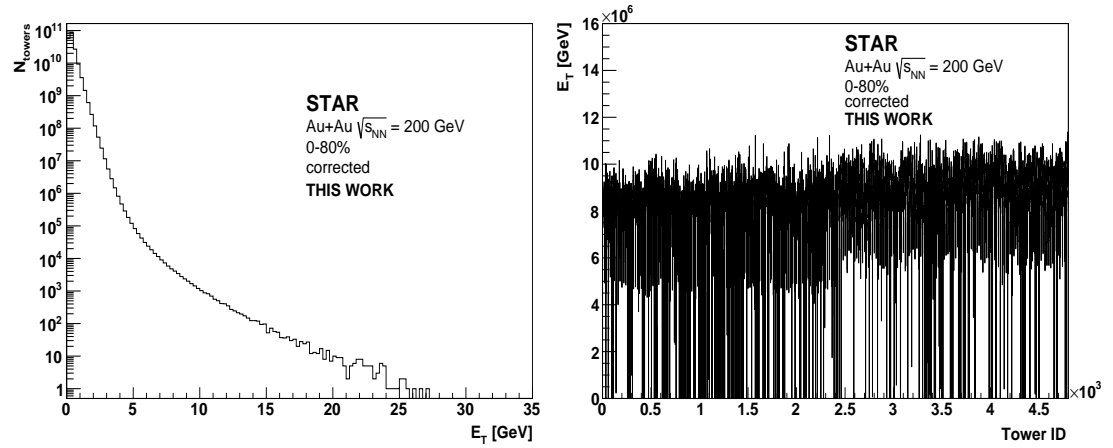
Figure 4.11: Tower E_T distribution (top) and total energy deposit in each tower (bottom) in Au+Au collisions at $\sqrt{s_{NN}} = 200$ GeV during Run 14 before (left) and after (right) exclusion of hot towers.

4.4 Jet reconstruction

Charged and full jets were reconstructed as a function of jet resolution parameter $R = 0.2, 0.3, 0.4$ as well as function of centrality in 5 centrality bins: 0-10%, 10-20%, 20-40%, 40-60%, 60-80%. But our detailed analysis is focused on 0-10% and 60-80% centrality bin, because in the future we will calculate nuclear modification factor R_{CP} that represents ratio of jet spectra in these two bins, when jet spectrum in 60-80% centrality bin is taken as a reference. Full jet reconstruction in contrast to charged jets provides a direct measurement of whole original energy of scattered partons before energy loss in the medium. We are not limited only to charged particles, but we accept also neutral component of the jet. This approach enables reconstruction of parton kinematics in unbiased way and also extends the kinematic reach of jet reconstruction in Au+Au collisions up to higher jet energies than we would achieve with charged jets.

There is a minimum p_T cut $p_T^{min} = 200$ MeV/c and maximum p_T cut $p_T^{max} = 30$ GeV/c on each jet constituent (each track or tower). Pseudorapidity interval cut $|\eta| < 1 - R$ based on the jet centroid was applied on each jet. This cut is also referred to as a fiducial cut which excludes reconstructed jets out of range of the TPC and the BEMC acceptance.

In the $\eta - \phi$ space of jets depicted in Figure 4.12 there is almost an empty sector which overlaps with the empty sector in the TPC in Figure 4.4. But on the right side of this sector, we can see small area with increased number of jets, but in track $\eta - \phi$ distribution the number of tracks is the same as an average in whole space. Higher jet number might be caused by a migration of jet centroids from the sector with fewer jets or by reconstruction of jets with small jet area A due to the sector with small number of tracks. It was considered to exclude jets reconstructed in these sectors, but no difference in jet spectra was observed. Probably sector with higher number of jets compensate the sector with fewer jets.
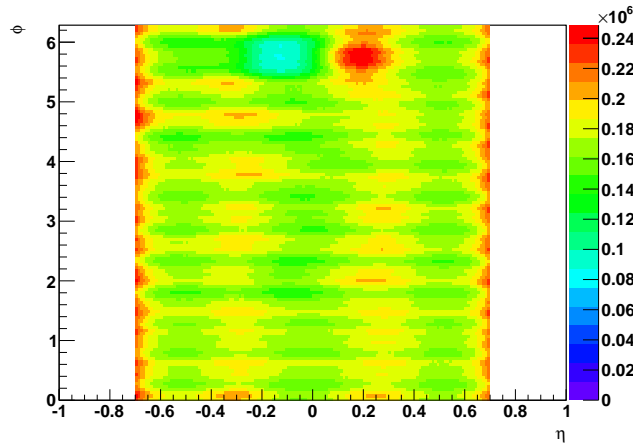
Figure 4.12: $\eta - \phi$ distribution of reconstructed charged jets with the resolution parameter $R = 0.3$ in Au+Au collisions at $\sqrt{s_{NN}} = 200$ GeV during Run 14.

4.4.1 Average background subtraction

The transverse momentum density of background ρ is estimated using jets reconstructed by the k_T-algorithm. In each central collision, two highest p_T jets reconstructed by the k_T algorithm were excluded while a in peripheral collision only one the most energetic jet is removed from the calculation of background energy density ρ to reduce the influence of true jets on the background estimate. The ρ value was then computed as a median of p_T of k_T-jets according to the following formula [46]:

$$\rho = \mathrm{median}\left(\frac{p_{T,i}}{A_i}\right),\tag{4.2}$$

where i runs over all reconstructed jets with transverse momentum $p_{T,i}$ and area of jet A_i in the event.

Figure 4.13 presents the background energy density ρ dependence on the reference multiplicity N_{ch} of a collision measured in $|\eta| < 0.5$ for charged and full jets. The shape of ρ dependence on N_{ch} for full jets is less regular than for charged jets, therefore detailed studies of background produced in full jets are required to clearly understand what we see. Our result from STAR can be compared with the result for charged jets from the ALICE experiment in Pb+Pb collisions at center of mass energy $\sqrt{s_{NN}} = 2.76$ TeV. The dependence of the background energy density ρ charged particle multiplicity N_{ch} at ALICE can be found in Figure 4.14. As we can expect higher collision energies produce larger background. Both distributions of ρ in charged jets are similar, but ours does not behave linearly.

The projection of estimated background energy of charged and full jets in Figure 4.13 for each resolution parameter R done in central collisions is presented in Figure 4.15. The estimated mean background energy of charged jets is approximately $\rho = 25$ GeV/c with $\sigma = 3$ GeV/c. Full jet background energy density is about $\rho = 63$ GeV/c with $\sigma = 9$ GeV/c. From the figure it is obvious that values of mean background energy density do not depend on the resolution parameter R. The value of background energy density in the central collision at ALICE is $\rho = 138.32 \pm 0.02$ GeV/c and $\sigma = 18.51 \pm 0.01$ GeV/c and for peripheral collisions 50-60% is $\rho = 12.05 \pm 0.01$ GeV/c and $\sigma = 3.41 \pm 0.01$ GeV/c[55]. Minimum jet constituent cut was $p_T = 150$ MeV/c. All values of the mean background energy density ρ with σ in central collisions for all resolution parameters are summarized in Table 4.2 and compared with result from the ALICE experiment.

After background energy estimation, an event-by-event correction for each jet with measured momentum $p_{T,uncorr}$ is applied. To obtain jet momentum $p_{T,corr}$ corrected for background, the median of jet background energy density ρ multiplied by the jet area A is subtracted from measured jet momentum $p_{T,uncorr}$ according to the formula:

$$p_{T,corr} = p_{T,uncorr} - A\rho.\tag{4.3}$$

4.4.2 Jet area study

Subtraction of mean background energy density is not sufficient enough to suppress combinatorial background, but by imposing reasonable cut on jet area removes jets reconstructed only from background. Figure 4.16 shows the jet area distribution versus jet p_T for charged and full jets with a resolution parameter $R = 0.2, 0.3, 0.4$
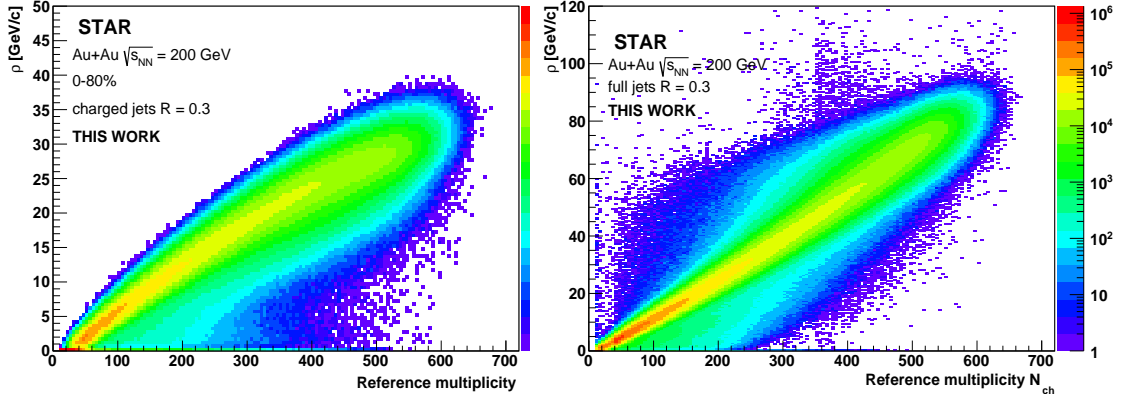
Figure 4.13: Background energy density ρ estimated from the median of charged (left) jets and full jets (right) reconstructed by the k_T-algorithm with the resolution parameter $R = 0.3$ versus reference multiplicity of charged particles N_{ch} in $|\eta| < 0.5$ in Au+Au collisions at $\sqrt{s_{NN}} = 200$ GeV.
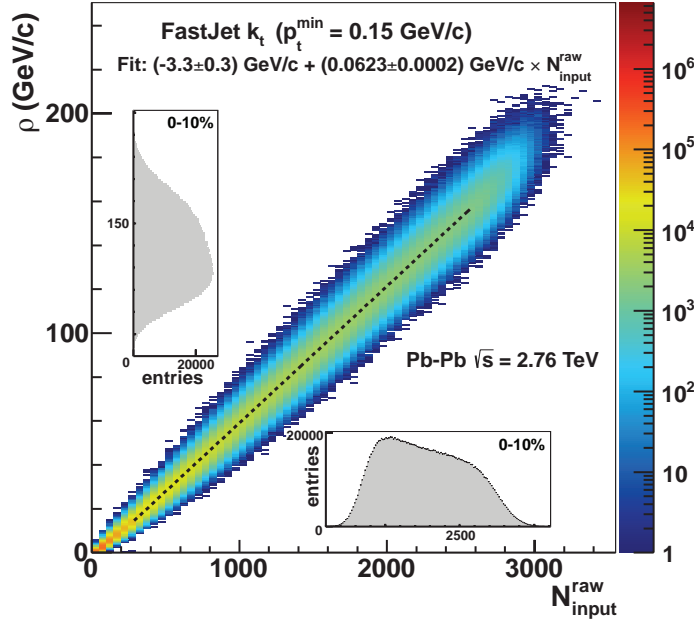
Figure 4.14: Background energy density ρ estimated from the median of charged jets reconstructed by the k_T-algorithm versus reference multiplicity of charged particles at the ALICE experiment in Pb+Pb collisions at $\sqrt{s_{NN}} = 2.76$ TeV .[55]

in central Au+Au collisions. From the figure we can see that jets reconstructed with a very low jet area do not have to be true jets, because they might comprise only from one high p_T particle or many close low p_T particles combined from background. The jet area cut should preserve true hard jets with high efficiency. A line in Figure 4.16 represents area cut on jets and only jet with area above this threshold are

Centrality	R	ρ [GeV/c]	σ [GeV/c]
full jets			
0-10%	0.2	63.2	9.1
	0.3	63.7	9.1
	0.4	63.9	9.2
charged jets			
0-10%	0.2	24.9	3.1
	0.3	25.6	3.1
	0.4	25.8	3.1
charged jets ALICE			
0-10%	0.4	138.3	18.5

Table 4.2: The mean background energy density ρ with σ for different resolution parameters R in 0-10% centrality class of Au+Au collisions at $\sqrt{s_{NN}} = 200$ GeV for full jets an charged jets. Results from STAR are compared to the mean background energy density ρ with σ and the resolution parameter $R = 0.4$ measured by the ALICE experiment in central 0-10% Pb+Pb collisions at $\sqrt{s_{NN}} = 2.76$ TeV.
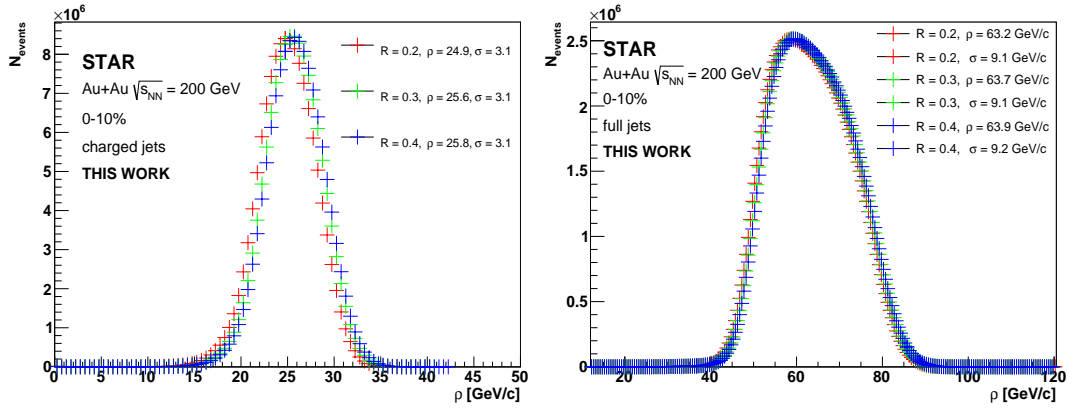
Figure 4.15: Background energy density for charged (left) and full (right) jets in 0-10% central Au+Au collisions at $\sqrt{s_{NN}} = 200$ GeV. The jet resolution parameter is $R = 0.2, 0.3, 0.4$ and the mean background energy density with σ are listed (see legend).

further accepted in the analysis. These cuts are listed in Table 4.3.

Figure 4.17 presents jet area distribution of all reconstructed full and charged jets with the resolution parameter $R = 0.2, 0.3, 0.4$ in central collisions. This figure is an area projection of the previous figure in area. The significant number of low p_T jets with small area was excluded and true high p_T jets are preserved. The red filled histogram in Figure 4.17 represents true jet area distribution of all reconstructed full and charged jets with jet $p_T > 10$ GeV/c and the resolution parameter $R = 0.2$, 0.3, 0.4 in central collisions. We can see that jet area cuts are well justified and resulting predominantly in true jets.
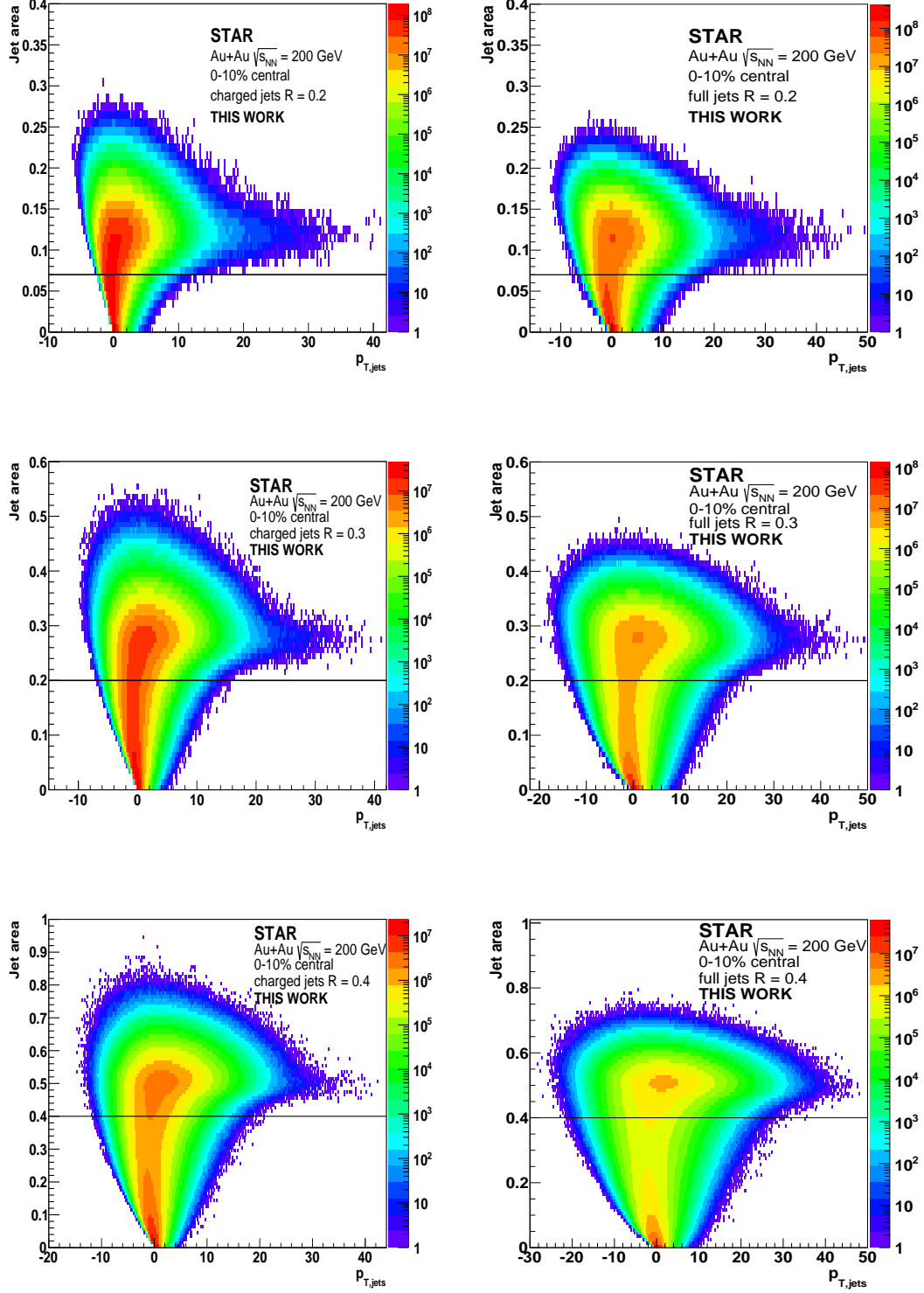
Figure 4.16: Jet area versus jet p_T for full (left) and charged (right) jets with the resolution parameter $R = 0.2$ (top),0.3 (middle), 0.4 (bottom) in central 0-10% Au+Au collisions at $\sqrt{s_{NN}} = 200$ GeV. The line represents cut on jet area.
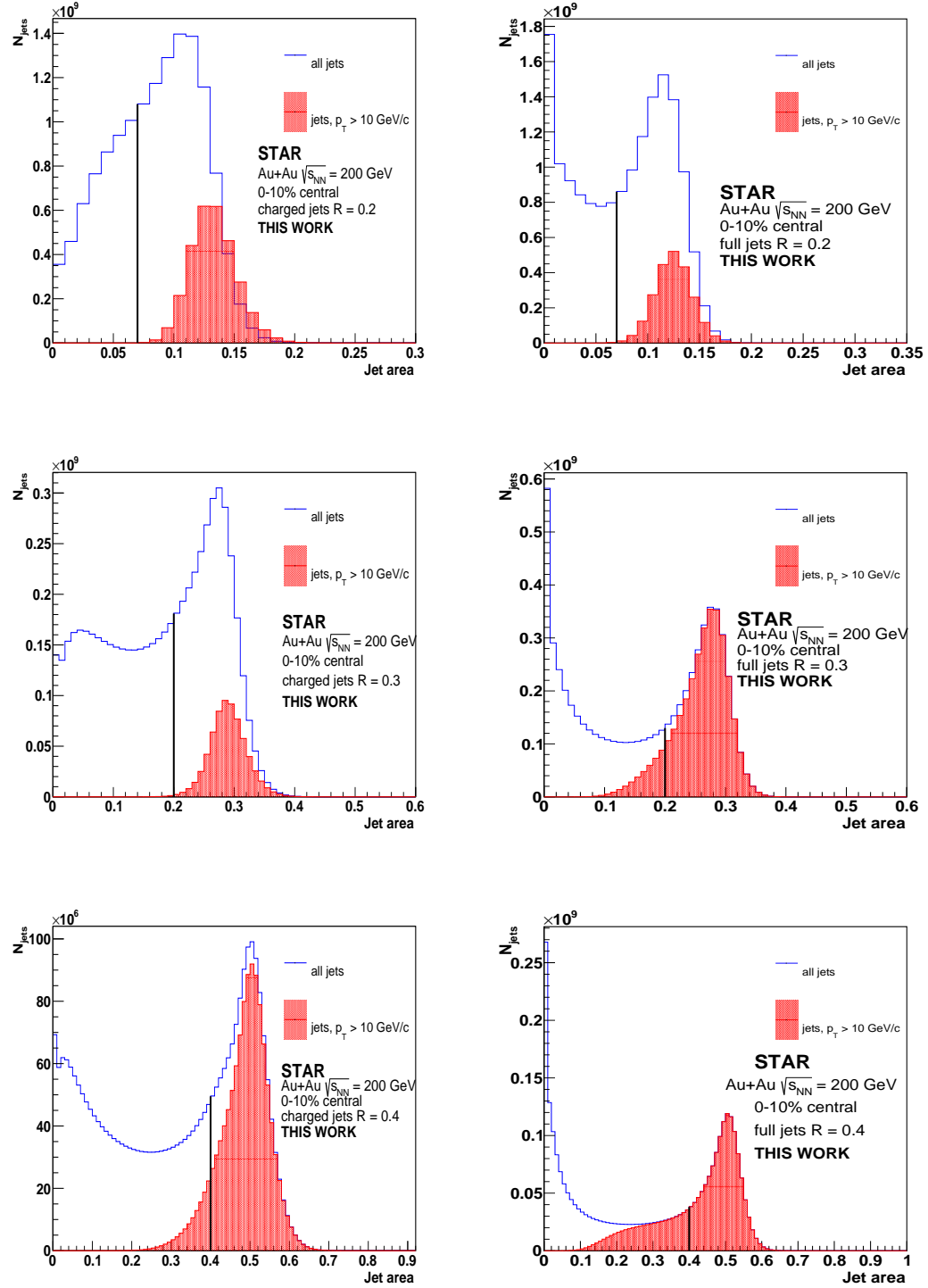
Figure 4.17: Jet area distribution for charged (left) and full (right) jets with the resolution parameter $R = 0.2$ (top),0.3 (middle), 0.4 (bottom) in central 0-10% Au+Au collisions at $\sqrt{s_{NN}} = 200$ GeV. The line represents cut on jet area. Red part of the histogram are distributions for jets with $p_T > 10$ GeV/c (jets with $p_T > 10$ GeV/c and $R = 0.2$ are scaled 100x.)

Resolution parameter R	Jet area A
R = 0.2	A > 0.07
R = 0.3	A > 0.2
R = 0.4	A > 0.4

Table 4.3: Jet area cut for used jet resolution parameter.

4.4.3 Uncorrected inclusive charged and full jet spectra

This section presents results from reconstruction of charged and full jet spectra. These jets are not yet corrected for detector effects and background fluctuations. Jets were reconstructed as a function of jet resolution parameter $R = 0.2, 0.3, 0.4$ as well as function of centrality in 5 centrality bins: 0-10%, 10-20%, 20-40%, 40-60%, 60-80%.

Figure 4.18 presents charged and full jet spectrum corrected only for the mean background energy density $< \rho >$ for three jet resolution parameters $R = 0.2, 0.3, 0.4$ reconstructed in Au+Au central and peripheral collisions at $\sqrt{s_{NN}} = 200$ GeV. As we expect, the largest kinematic reach has the jet spectrum in central collisions and $R = 0.4$. Jets with larger R clusters more particles, thus the total momentum of the jet is higher. For higher jet energies, jet spectra for different R converge to each other. Central collisions show a noticeable difference between resolution parameters but in comparison with peripheral collisions, the difference in jet spectrum between R is almost negligible.

From the comparison of charged (left) and full jet spectra (right) we can see, that full jet reconstruction in contrast to charged one increases the statistics of jets and their kinematic reach by more than 10 GeV/c.

Distributions of jets with corrected $p_{T,jet}^{corr}$ to background contribution contain also jets with negative values, because we subtract ρ - the median of jet energy density. In many jet analysis, this negative-p_T part of jet population is discarded because it is considered as unphysical. In spite of that we keep jet population with negative p_T due to their valuable information about background.

Figures 4.19 show jet spectrum with three cuts applied on the momentum of the leading hadron in a jet: $p_T^{lead.h.} \geq 0, 3, 5, 6, 7$ GeV/c with resolution parameter $R = 0.3$ in central and peripheral collisions. Cuts on the momentum of the leading hadron lead to suppression of combinatorial background and we can obtain only true high p_T jets. This is necessary for unfolding, because a large amount of soft jets and combinatorial background can lead to instability of unfolding that will not converge to the correct solutions. The cut applied on the momentum of the leading particle however introduces a bias and jet reconstruction is no more 100% collinear safe.

Figure 4.20 shows the dependence of jet spectrum on centrality of a collision. Full and charged jets are reconstructed with the resolution parameter $R = 0.3$. By decreasing of centrality of the collision (from central to peripheral) we can observe narrowing of jet spectrum. It means that in central collisions there is more hard jets than in peripheral.
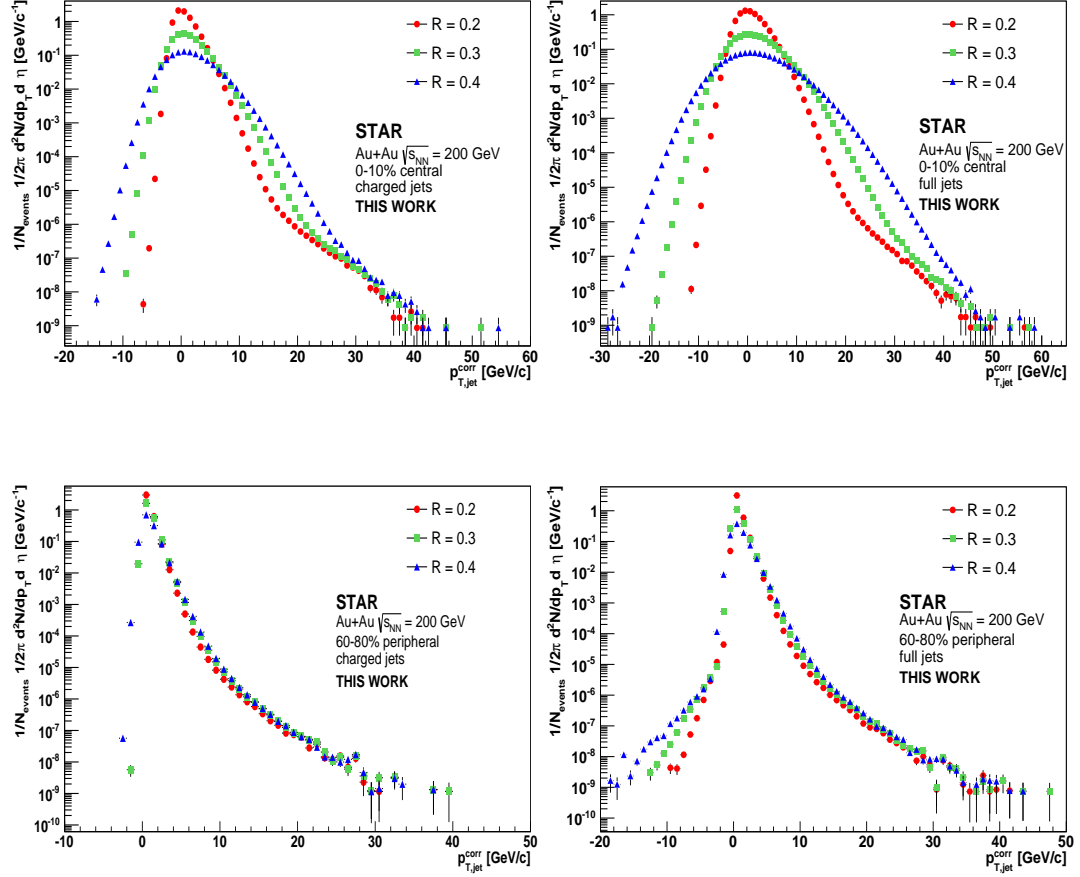
Figure 4.18: Charged (left) and fully (right) reconstructed jet spectrum corrected to background energy density ρ in central 0-10% (top) and peripheral 60-80% (bottom) Au+Au collisions at $\sqrt{s_{NN}} = 200$ GeV with three resolution parameters $R = 0.2, 0.3, 0.4$ and imposed cut on jet area according Table 4.3

Hadronic correction

Full jet reconstruction requires charged and also neutral component. Charged component represents tracks (hadrons) from the TPC and neutral component towers from the BEMC, however charged tracks are registered by the BEMC and leave there an amount of energy. To avoid double counting of track and tower of the same particle it is necessary to subtract p_T of track from p_T of towers. In order to subtract the charged particle energy deposit from the associated tower clusters, charged tracks are propagated to the BEMC clusters. If the difference between the track and the tower in $\eta - \phi$ space satisfies a condition $\Delta\eta < 0.25$ and $\Delta\phi < 0.25$ rad, the track is matched with the tower and their energy is subtracted. This is referred to as a hadronic correction and is driven by a parameter that represent a fraction of subtracted track energy. However, the energy deposition of charged particles in the BEMC can be determined only statistically, because we do not know precisely the fraction of deposited charged-particle energy. The hadronic correction parameter
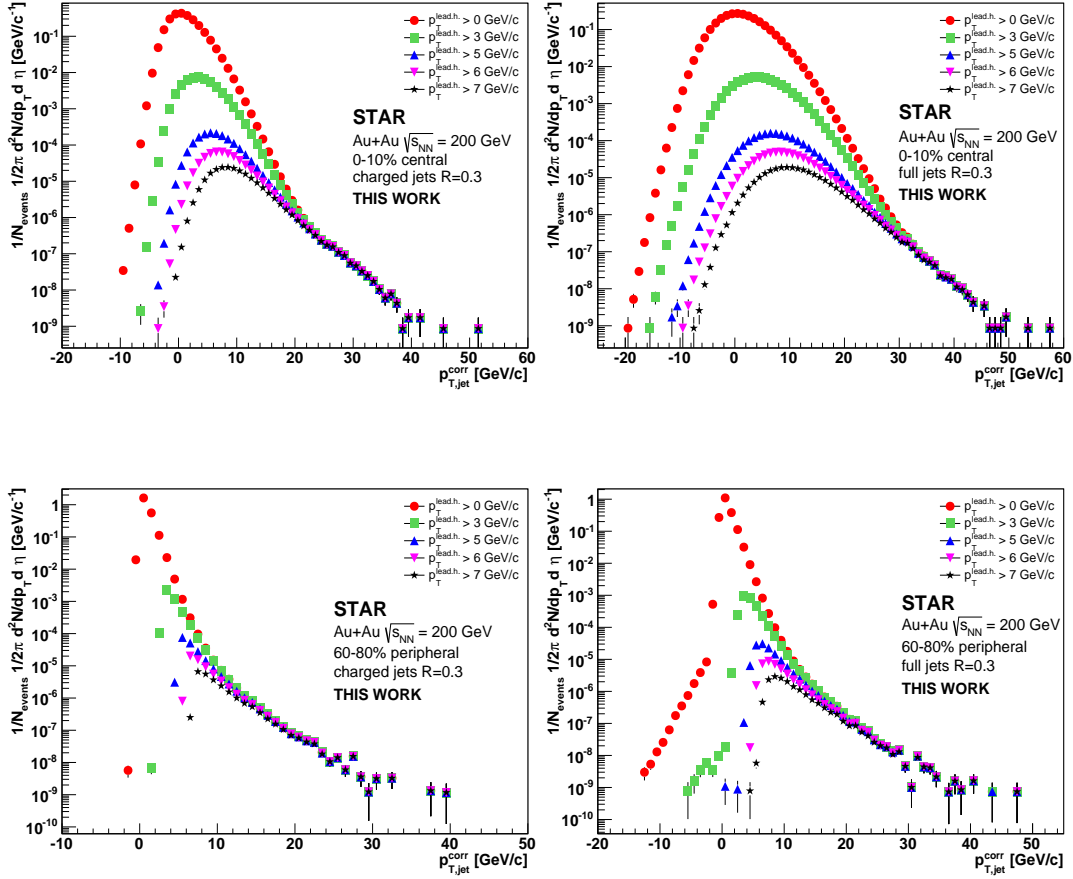
Figure 4.19: Charged (left) and fully (right) reconstructed jet spectrum corrected to background energy density ρ in Au+Au collisions at $\sqrt{s_{NN}} = 200$ GeV in 0-10% central (top), and 60-80% peripheral collisions (bottom). The resolution parameter $R = 0.3$ and p_T leading cuts $\geq 0, 3, 5, 6, 7$ GeV/c were used in this jet reconstruction.

of tower energy deposit was set to value 1.0, which means that whole fraction of charged track p_T is subtracted from deposited tower energy. If the difference between track and tower energy is less than 200 MeV, the tower with remaining energy is not accepted to the jet reconstruction. Comparison of uncorrected full jet spectra as a function of hadronic correction parameter, 0 and 1, can be seen in Figure 4.21.

It is also possible to apply minimum-ionizing particle (MIP) energy deposition correction, when energy of each charged particle deposited in BEMC is estimated from the formula:

$$E_{MIP} = (0.261 \text{GeV}/c) \frac{1 + 0.056\eta^2}{\sin(2\tan^{-1}(\eta))} \tag{4.4}$$

MIP correction was studied in full jet analysis in Run 11 and for full jets with $p_T > 15$ gave same results as hadronic correction with parameter equals to 0. We do not take MIP correction into account for now, but in the future we will take it into consideration again when more detailed analysis of full jets will take place.
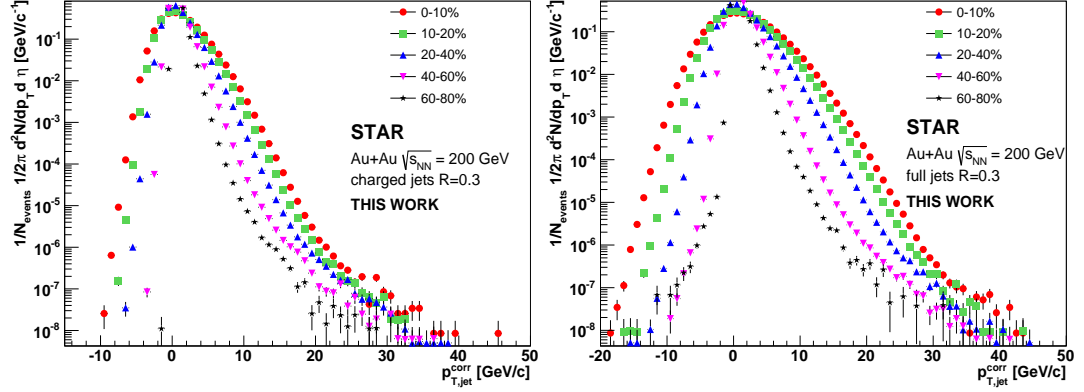
Figure 4.20: Charged (left) and fully (right) reconstructed jet spectrum corrected to background energy density ρ in Au+Au collisions at $\sqrt{s_{NN}} = 200$ GeV with the resolution parameter $R = 0.3$ for all centrality classes (see legend).
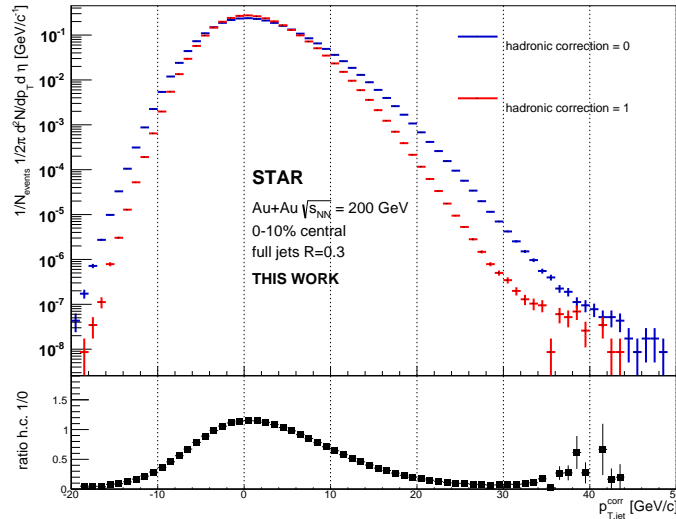
Figure 4.21: Full jet spectra for hadronic correction parameter 0 and 1 with their ratio for 0-10% central collisions and resolution parameter $R = 0.3$.

4.5 Unfolding of background fluctuations and detector effects

In general, experimental data and observables measured by any detector are usually distorted and transformed by various effects. Each measured distribution can be slightly changed due to migration effects, limited acceptance and resolution, limited statistical precision etc. Technique for obtaining true spectrum from the measured one is referred to as an unfolding or alternatively referred to as a deconvolution. It

is a complex mathematical operation that requires very good understanding of the
detector and conditions of the experiment. This information is usually encoded in
the response matrix which should satisfy condition:

$$\mathbb{A}x = y, \tag{4.5}$$

where x is the true distribution and y the measured one. A straightforward way
how to obtain x - real distribution from y - measured one would be calculation
of inverse matrix A^{-1}. Unfortunately, this matrix is usually not regular and for
singular matrices the inverse one does not exist. Therefore we should look for another
approach for deconvolution of data. In the last years several unfolding techniques
in high energy physics were developed. Commonly used methods are mainly:

- Bayesian unfolding [56]- based on Bayes's theorem to calculate reverse proba-
bility from the known probability.

- SVD unfolding[57] - based on the singular value decomposition of the response
matrix.

4.5.1 Bayes unfolding

A procedure which offers a natural way of correcting experimental distributions in
order to get best estimate of the true one is a multidimensional unfolding method
based on Bayes's theorem. Bayesian unfolding was proposed by G. D'Agostini[56].

Bayes' theorem is used to find conditional probability $P(A|B)$ of a observing
a measurement A that is caused by a given event B (B is true), when the reverse
conditional probability $P(B|A)$ is known. In other words $P(B|A)$ is the probability
of the given event to observe the measurement B. So in more detail, let us have
several independent causes $(t_i, i = 1, 2, ..., n_t)$ which can produce one possible effect
(m_j). Then we assume known initial probability of the causes $P(t_i)$ and the condi-
tional probability of the i-th cause to produce effect m_j is $P(m_j|t_i)$. Bayes' formula
is

$$P(t_i|m_j) = \frac{P(m_j|t_i)P_0(t_i)}{\sum_l^{n_t} P(m_j|t_i)P_0(t_i)} \tag{4.6}$$

In our case, we have causes $\vec{t}$, where t_i is the i-th bin of the true distribution and
$\vec{m_j}$ is a j-th value of our measured distribution. We attempt to calculate $P(t_i|m_j)$
that is the probability of observing true value t_i when we measure m_j. According to
the formula, it is necessary to know probability $P(m_j|t_i)$ that represents the response
matrix $\mathbf{R}[p_T^{true}(i), p_T^{measured}(j)] = R_{ij}$ determined in the previous section. $P_0(t_i)$ is
a prior probability of i-th bin of the true distribution to have value t_i and brings
our knowledge about true distribution to the unfolding. If we denote contents of the
bin t_i and m_i as $n(t_i)$ and $n(m_j)$ respectively, then the best estimate $\hat{n}(t_i)$ can be
calculated according formula:

$$\hat{n}(t_i) = \sum_{j=1}^{n_t} n(m_j)P(t_i|m_j) \tag{4.7}$$

From these unfolded entries it is possible to estimate the true total number of entries and the final probability of the true distribution:

$$\hat{N}_{true} = \sum_{i=1}^{n_c} \hat{n}(t_i) \qquad\qquad \hat{P}(t_i) = P(t_i|n(m_j)) = \frac{\hat{n}(t_i)}{\hat{N}_{true}} \qquad (4.8)$$

In the case when initial distribution $P_0(t_i)$ is not consistent with data, $P_0(t_i)$ will not agree with the final distribution $\hat{P}(t_i)$. The closer the initial distribution is to the true distribution, the better the agreement is. It can be shown that the distribution $\hat{P}(t_i)$ lies between $P_0(t_i)$ and the true one. This suggests to proceed iteratively, hence unfolding is performed as follows:

1. Initial distribution $P_0(t)$ is chosen form the best knowledge of the process that we study. If no information about true distribution is available, then $P_0(t_i) = 1/n_t$ is just a uniform distribution.

2. $\hat{n}(t_i)$ and $\hat{P}(t)$ is calculated.

3. χ^2 comparison between $\hat{n}(t_i)$ and $n_0(t_i)$ is made

4. $P_0(t_i)$ is replaced by $\hat{P}(t_i)$ and $n_0(t_i)$ by $\hat{n}(t_i)$ and the process starts again. If the value of χ^2 of the second iteration is small, stop the iteration, otherwise continue with step 2.

4.5.2 SVD unfolding

The second widely used unfolding method is SVD (Singular Value Decomposition) unfolding and it was proposed by Hoecker and Kartvelishvili[57]. A singular value decomposition of a real $m \times n$ matrix A means its factorization in the form:

$$A = USV^T, \qquad (4.9)$$

where U is an $m \times m$ orthogonal matrix ($UU^T = U^TU = I$), V is an $n \times n$ orthogonal matrix, while S is an $n \times m$ matrix with non-negative diagonal elements:

$$S_{ij} = 0 \text{ for } i \neq j, \quad S_{ij} \equiv s_i > 0. \qquad (4.10)$$

The numbers s_i are referred to as singular values of the matrix A and columns of U and V are singular vectors. With SVD, it is possible to easily diagonalize a linear system $Ax = y$ by introducing rotated vectors z and d and the finding the exact solution looks as follows:

$$USV^Tx = y \quad \Rightarrow \quad z \equiv V_Tx, \quad d \equiv U^Ty \qquad (4.11)$$

$$s_iz_i = d_i \quad \Rightarrow \quad z_i = \frac{d_i}{s_i} \quad \Rightarrow \quad x = Vz \qquad (4.12)$$

The correct determination of the result z_i can sometimes failed and in order overcome this problem, further steps are needed. Firstly, it can happen that singular values s_i are very small (or even zero) that enhances errors on d_i and secondly due to the errors in y, d_i is insignificant having large errors.

4.5.3   Embedding

The next step of the analysis is the study of background fluctuations because previous corrections subtract only average of background.It is necessary to find out a correction which would characterize the size of the fluctuations and adequately describe a smearing of jet p_T by soft background. We used a data driven method in which additional particles or simulated jets with defined $p_T = 1, 2, 3, 4, 5, 6, 7, 8, 10, 15, 20, 40, 90$ GeV/c are embedded into a real event and jet reconstruction is carried out again. Afterwards, embedded particles or jets are matched to real ones and p_T of the embedded object is subtracted from p_T of reconstructed jet. We calculate the quantity:

$$\delta p_T = p_{T,jet}^{corr} - p_{T,jet}^{emb}, \tag{4.13}$$

which gives a relation between corrected $p_{T,jet}^{corr}$ of reconstructed jets and $p_{T,jet}^{emb}$ of the embedded object.

Distributions of δp_T with embedded particles with several $p_T = 3, 5, 7, 10, 20, 40$ GeV/c (not all) for charged jets of the resolution parameter $R = 0.3$ for central and peripheral collisions are depicted in Figure 4.22. We can see that δp_T distributions for all depicted embedded particles has the same shape and almost overlaps each other. For small $p_T^{emb} < 5$ there is an indication that distributions are narrower than for higher p_T^{emb}. But this difference is negligible and do not show in response matrix, because of imposing cuts on leading hadron $p_T^{lead.h.} \geq 5$ GeV/c.
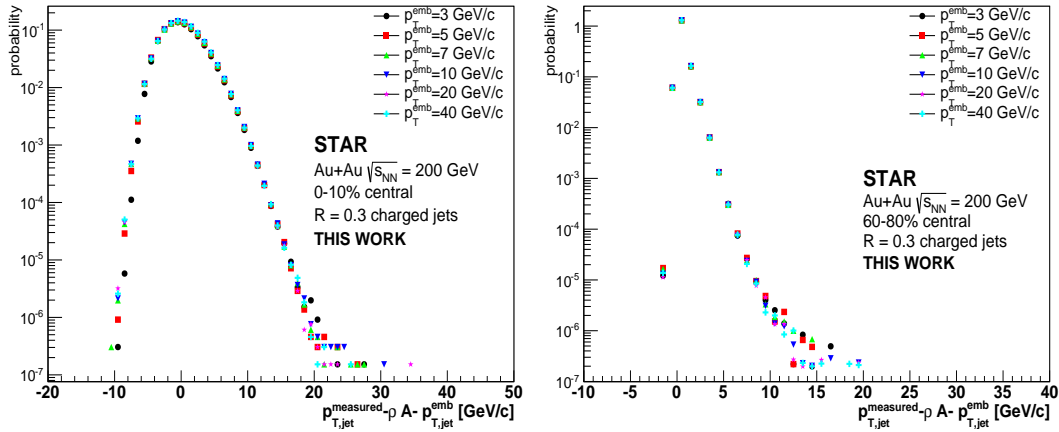
Figure 4.22: δp_T distributions for 0-10% central and 60-80% peripheral Au+Au collisions for the jet resolution parameter $R = 0.3$.

4.5.4   Background and detector response matrix

Distributions of δp_T from the previous section are further used for construction of the background response matrix in order to correct the measured jet spectrum for the smearing that occurs due to the fluctuating background. The background response matrix characterizes the size of these fluctuations and determines a probability to measure the value of $p_T^{measured}$ for a given real jet p_T^{true}. It is normalized to 1 which

means that the integral of the distribution is 1, making it a probability distribution. We have produced only several δp_T distributions for $p_{T,jet}^{true}$, however this is sufficient, because other $p_{T,jet}^{true}$ values are computed from interpolation of two closest δp_T distribution. Then centers of δp_T distributions ($\delta p_T = 0$) are placed at the diagonal of the response matrix.

The measured spectrum is also distorted by detector effects. In order to overcome this problem, a response matrix of detector effects is determined utilizing an event generator and simulation of detector conditions. The response matrix encodes all of the physics that is required to correct the measured jet spectra. It relates measured p_T of jets to true jet p_T. The detector response matrix contains also correction for the TPC tracking efficiency and track p_T smearing. These two effects were simulated in PYTHIA. From this section we work only with charged jets, because we do not have jet response matrix for the BEMC to unfold full jets. The calculation of the BEMC response matrix is beyond the thesis and will be one of the subjects of my future work.

We assume that background fluctuations and detector effects are independent of each other and both matrices are multiplied to obtain the full response matrix utilized in the unfolding procedure:

$$R_{full} = R_{\delta p_T} \times R_{det} \tag{4.14}$$

Our response matrix R_{full} has fine binning and narrow bins can eventually cause that unfolding would not work properly. Therefore the response matrix should be rebinned to coarser binning which should be comparable to the jet energy resolution. Correct rebinning also requires reweightening of the response matrix. The second reason of matrix rebinning is to make it compatible with RooUnfold software [58]. RooUnfold is a framework for unfolding and implements currently most used unfolding methods including also the Bayesian unfolding. The process of rebinning and reweightening starts with an uniform generation of random value $p_{T,jet}^{true}$. Then original matrix R_{full} is used for calculation of corresponding measured value $p_{T,jet}^{measured}$. A weight w is calculated as a probability for obtaining $p_{T,jet}^{true}$ from a prior functions used for unfolding. Used prior functions are 8 Tsalis functions with different parameters, $p_T^{-4.5}$, p_T^{-5}, $p_T^{-5.5}$ and PYTHIA generated jet distribution. They are shown in Figure 4.24.

Generation of $p_{T,jet}^{true}$ and calculation of weight is repeated N times (our statistics is 10^9) and the final response matrix R_{unf} for unfolding is the result of filling ($p_{T,jet}^{true}$, $p_{T,jet}^{measured}$, w) to 2D histogram.

Background, detector and full response matrix are depicted in Figure 4.23 for charged jets with cut of $p_T \geq 5$ GeV/c on leading hadron in central and peripheral collisions.
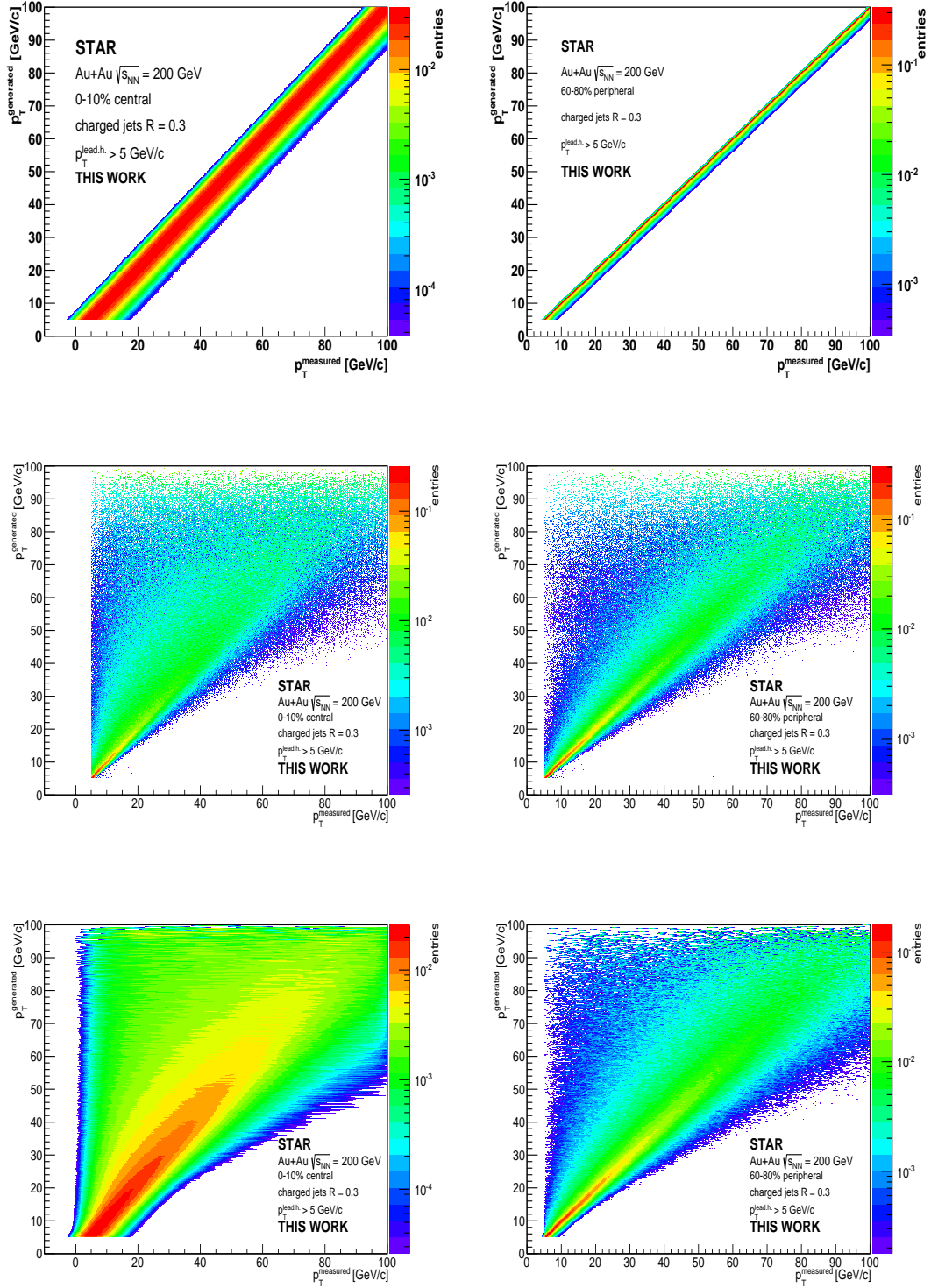
Figure 4.23: Top: Background response matrix. Middle: Detector response matrix. Bottom: Full response matrix for charged jets with cut of $p_T \geq 5$ GeV/c on leading hadron in central and peripheral collisions.
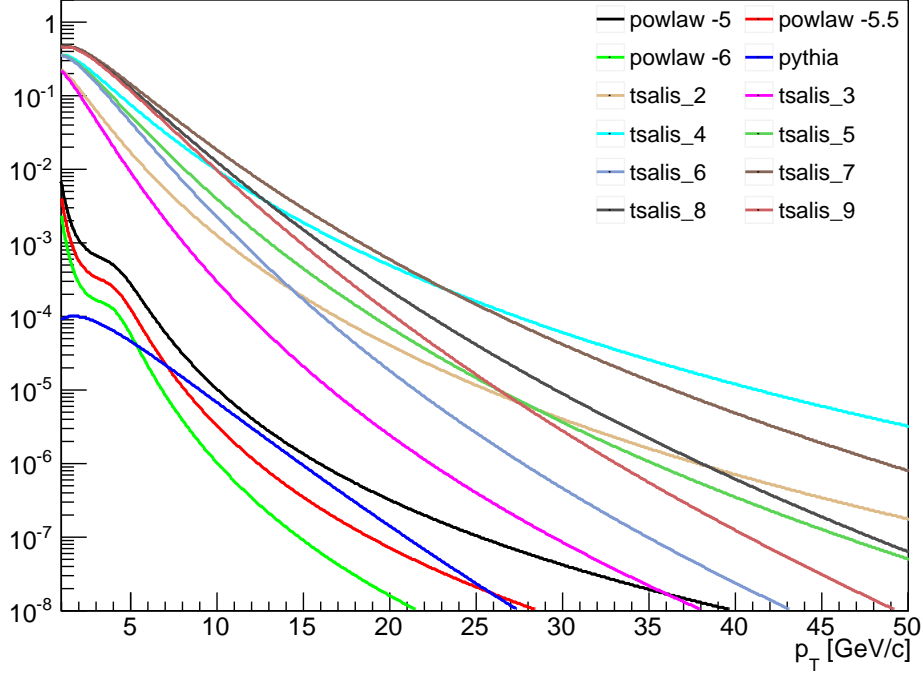
Figure 4.24: Prior functions used for unfolding and reweightening of response matrices.

4.5.5 Implementation of Bayesian unfolding

In this analysis the Bayesian unfolding method is applied on jet distribution to obtain true charged jet spectra. The most reliable iteration of unfolding was determined from a simulation done in the Toymodel [54]. The study in [54] showed that it is suitable to keep number of performing unfolding iteration as low as possible. The reasonable number of unfolding iterations is 3 or 4. In the analysis we take the 4th iteration. More iterations lead to instability of unfolding process caused by significantly increased statistical fluctuations making large oscillations of a solution around the true value. The result is obtained as an average value from solutions of all prior functions. With the increasing number of iterations to some reasonable value, solutions of all prior functions are successively closer to each other and the systematic uncertainty is decreasing. Figure 4.25 shows distributions of relative differences between individual solutions of all prior functions. The average taken from them in each bin for 6 unfolding iterations. Depicted differences between iterations were calculated using unfolded jet p_T distribution in central and peripheral collisions with the resolution parameter $R = 0.3$ and cut on leading hadron $p_T^{lead.h.} \geq 5$ GeV/c From the figure it is obvious, that solutions of individual prior functions for central collisions converge to the right one and from the 4th iteration the result and systematic uncertainties are lower and stable. For peripheral collisions, solutions for prior functions converge after second iterations and they are stable to the fourth iteration. After that solutions in two last bins oscillate more. The evolution of

unfolding is very similar for other resolution parameters or cuts on leading hadron $p_T^{lead.h.}$. Figure 4.26 presents ratios of jet distributions with $R = 0.3$ and $p_T^{lead.h.} \geq 5$ GeV/c in central collisions between iterations of unfolding for solution of all prior functions. The majority of solutions is consistent with unity in low p_T. Higher p_T bins require more iterations, but after 4 iterations they converge closer to the true solution. We do not take the last bin 30-40 GeV/c. into account due to its the large fluctuations between prior functions and large systematic uncertainty. Figure 4.27 shows ratios of jet distributions with $R = 0.3$ and $p_T^{lead.h.} \geq 5$ GeV/c in central collisions between a solution in one iteration and backfolded distribution from the following iteration for solutions of all prior functions. These ratios shows how the used unfolding method is reliable in terms of successful obtaining solutions from the previous iteration when we apply "reverse" unfolding, also called backfolding.

4.6 Results

This section presents unfolded charged jet spectra corrected for background and detector effects. Figure 4.28 shows inclusive charged jet spectra for central 0-10% (left) and peripheral 60-80% Au+Au collisions (right), for different p_T cut on leading hadron $p_T^{lead.h.} \geq 5$ (top), 6 (middle) and 7 (bottom) GeVc and 3 different jet resolution parameters $R = 0.2, 0.3, 0.4$.

The results incorporate two types of uncertainties: statistical and systematic. The statistical uncertainty of each bin was determined as a square root of entries ($\sqrt{N}$) in each bin. Systematic uncertainty of the result was calculated by subtracting of all solutions of prior functions x_i from their average $\bar{x}$ for each bin. Then differences were summed up in quadrature, divided by their count N and from the resulting value the square root was extracted according to formula:

$$\sigma = \sqrt{\frac{\sum_{i=1}^{N}(x_i - \bar{x})^2}{N}} \tag{4.15}$$

The result can be influenced by other sources of systematic uncertainties, for example tracking efficiency that is estimated to be $\pm 5\%$, track cuts, correction for v_2, ρ calculation, hadron ratios, fragmentation model, jet energy scale...
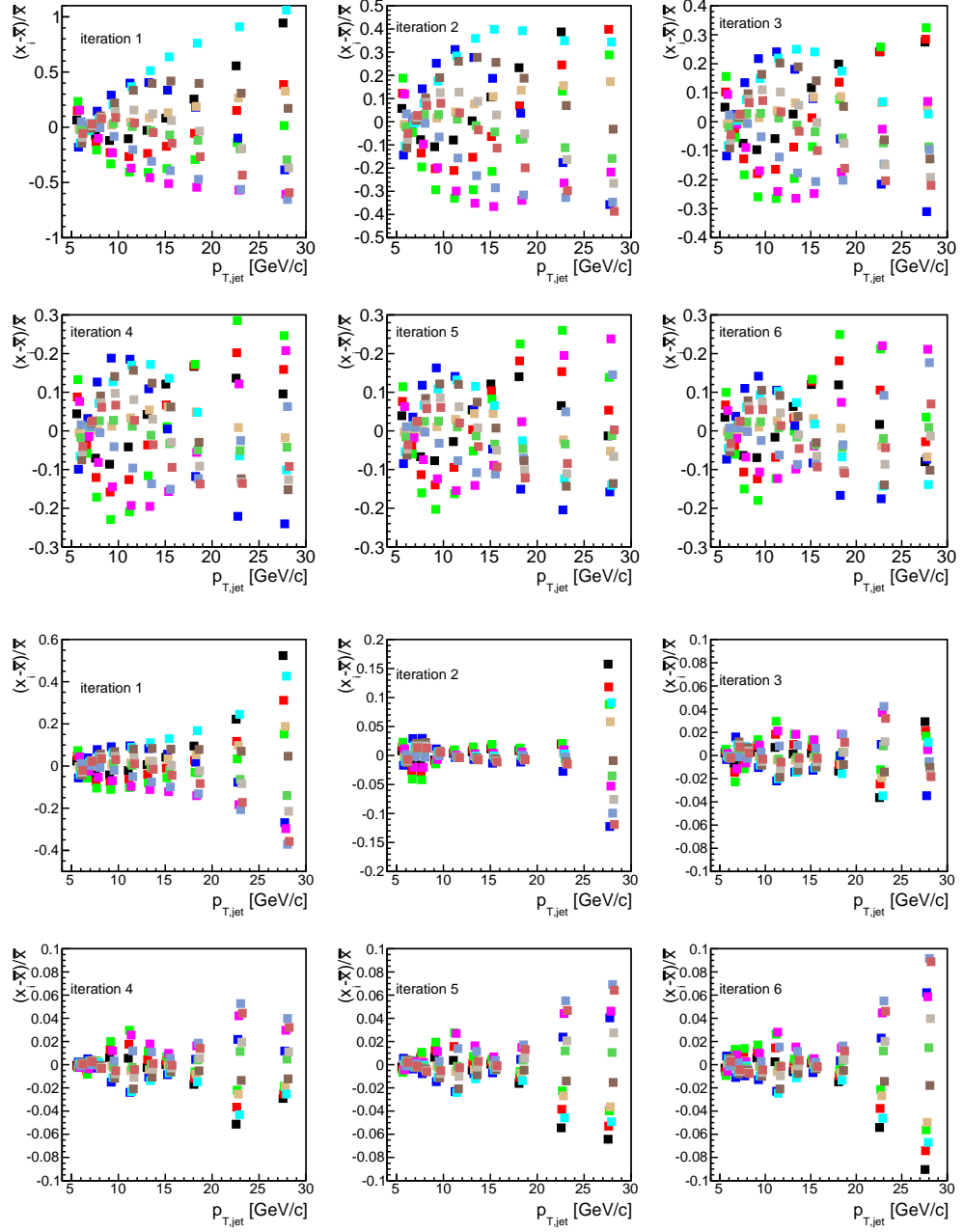
Figure 4.25: Distributions of relative differences between individual solutions for each prior function x_i and average of them $\bar{x}$ for 6 unfolding iterations. This is done for unfolded jet distribution in central (top 2 lines) and peripheral (bottom 2 lines) collisions, resolution parameter $R = 0.3$ and cut on leading hadron $p_T^{lead.h.} \geq 5$ GeV$/$(c).
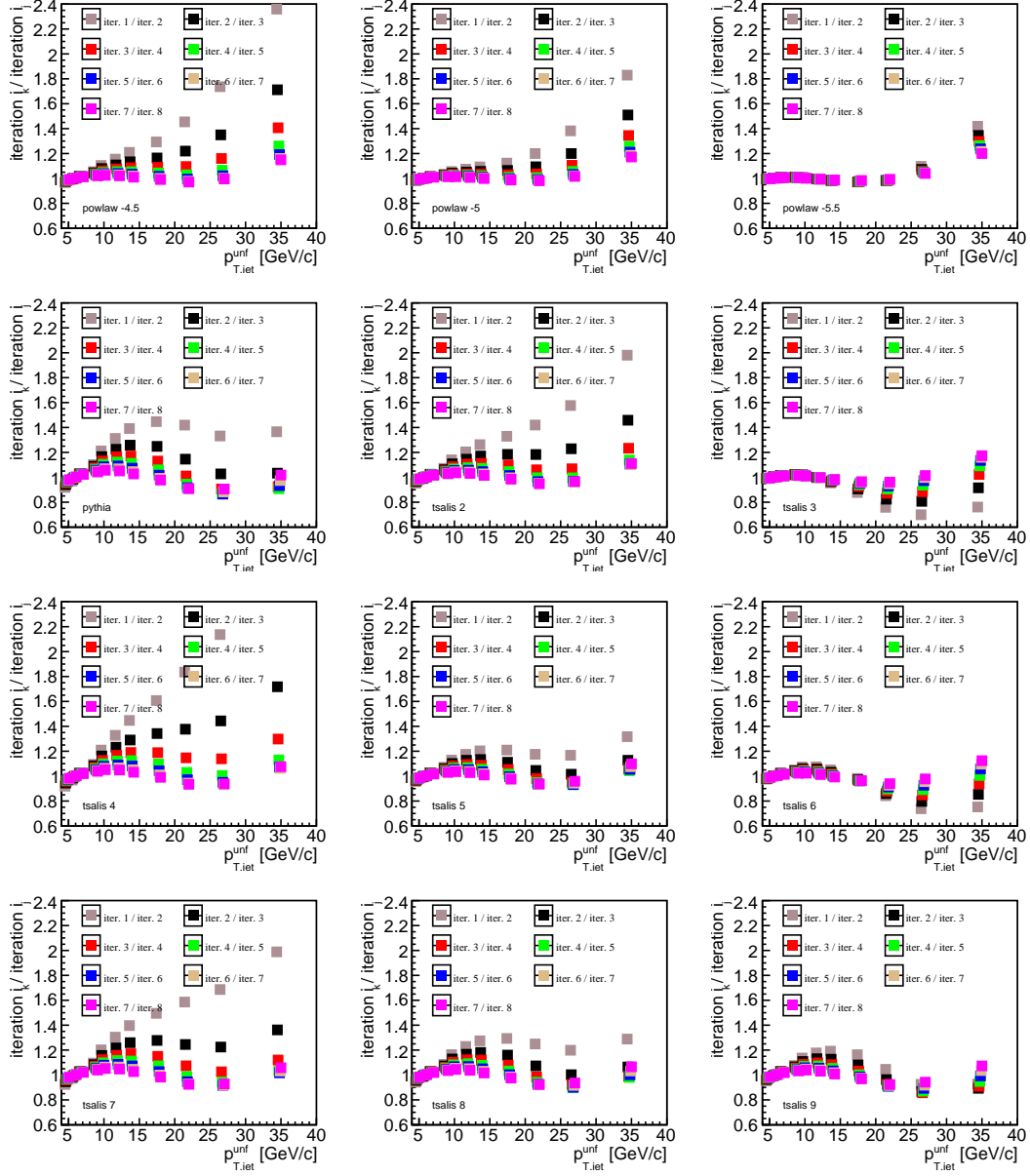
Figure 4.26: Ratios of jet distributions with $R = 0.3$ and $p_T^{lead.h.} \geq 5$ GeV/(c) in central collisions between 7 pairs of subsequent iterations of unfolding for solutions of all prior functions .
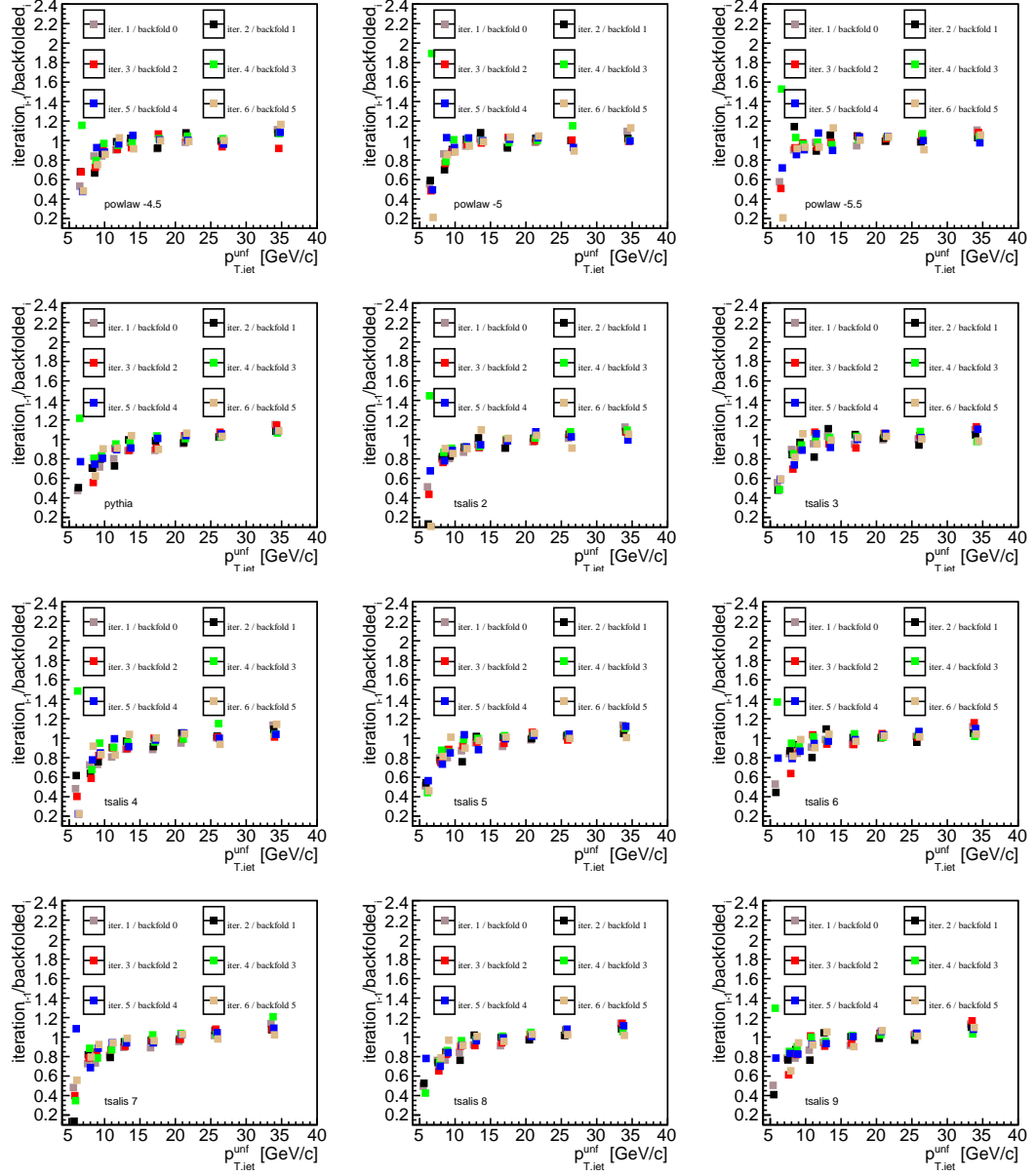
Figure 4.27: Ratios of jet distributions with $R = 0.3$ and $p_T^{lead.h.} \geq 5$ GeV/(c) in central collisions between an iteration and backfolded distribution from the following iteration for solutions of all prior functions.
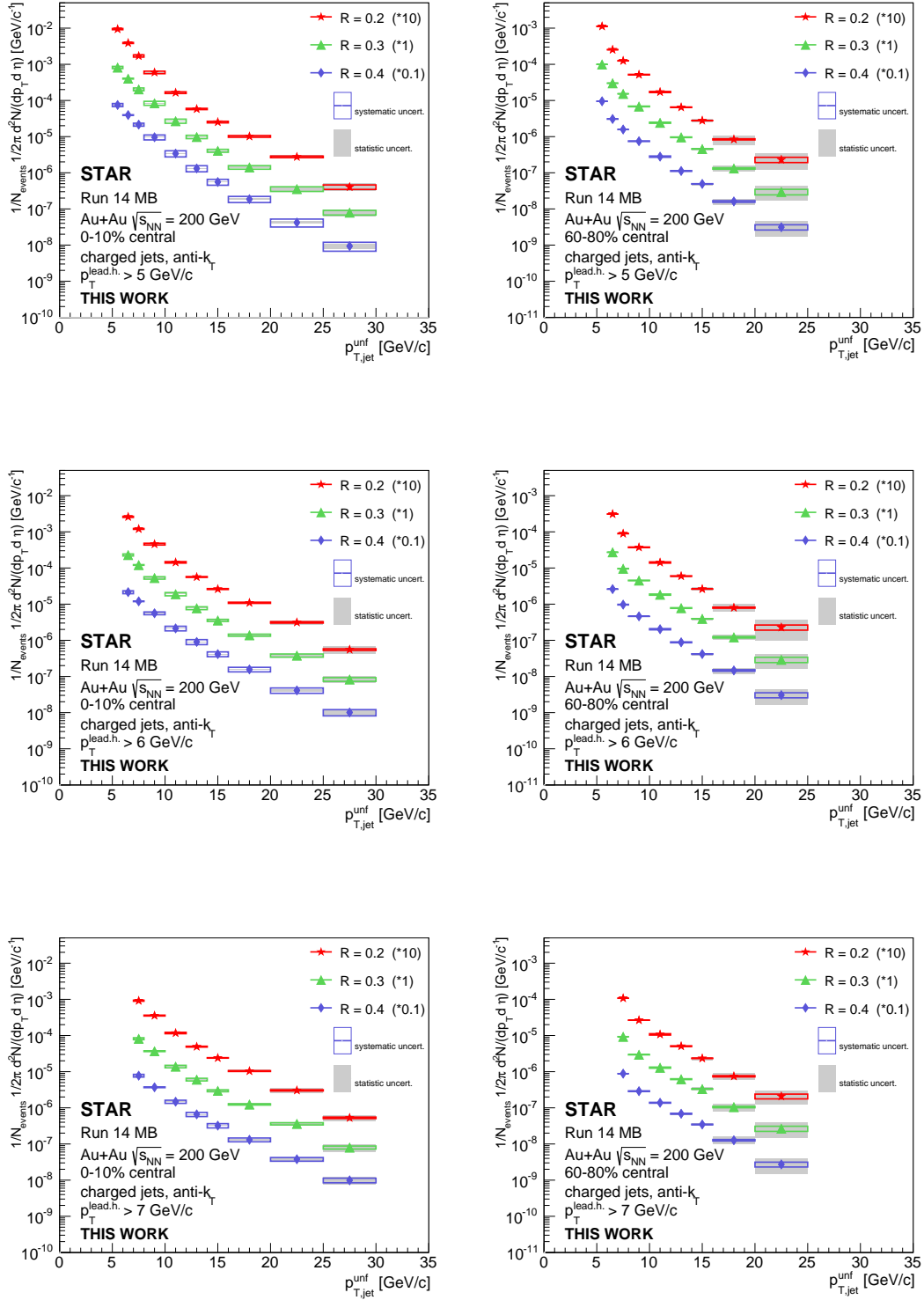
Figure 4.28: Unfolded charged jet spectra for central 0-10% (left) and peripheral 60-80% (right) Au+Au collisions, for p_T cut on leading hadron $p_T^{lead.h.} \geq 5$ (top), 6 (middle) and 7 (bottom) GeVc and 3 different jet resolution parameters $R = 0.2$, 0.3, 0.4.

Summary and Outlook

Experiments at RHIC and at the LHC are utilized for research of quark-gluon plasma which is a new state of hot and dense strongly interacting nuclear matter consisting of free partons. QGP is theoretically predicted by Quantum Chromodynamics and exists at extremely high temperature and density. QGP is supposed to be formed in ultra-relativistic heavy-ion collision which is a dynamical process with large energy transfer and lasts only few femtoseconds. During hard scattering, partons of incoming nuclei undergo fragmentation and hadronisation resulting in jets, collimated sprays of hadrons.

Due to elastic and inelastic interactions of hard partons with QGP the energy of partons is reduced in comparison with p+p collisions. It means that jets might be quenched and modified by medium and this phenomenon is referred to as a jet quenching. Jet quenching provides one of the key signatures of the QGP formation and its study helps in the research of the strong interaction.

Jet-finding algorithms are used for jet reconstruction and their main goal is to cluster a set of charged tracks and energy deposited in towers into jets. The algorithm selects a set of particles, which are typically emitted close to each other in an angle and combines their momenta to form the momentum of a jet. Jet resembles kinematic properties of the original parton. Therefore jet reconstruction allows to access early stages of the collision. Jet reconstruction is successful in p+p collisions, while in the heavy-ion collision environment is more complicated due to the large fluctuating background.

Full jet reconstruction, in contrast to charged one, provides a direct measurement of whole original energy of scattered partons before energy loss in the medium. We are not limited only to charged particles, but we accept also neutral component of the jet. This approach enables reconstruction of parton kinematics in unbiased way and also extends the kinematic reach of jet reconstruction in Au+Au collisions up to higher jet energies.

One of the experiments that is utilized for exploration of the behavior and properties of the strongly interacting nuclear matter is STAR, located at RHIC in Brookhaven National Laboratory. The STAR experiment consists of several different types of subdetectors and the most important detectors for our jet analysis are Time Projection Chamber for charged particles and Barrel Electromagnetic Calorimeter for neutral energy deposited in towers.

The main part of the diploma thesis presents results of charged and full jet reconstruction in Au+Au collisions at $\sqrt{s_{NN}} = 200$ GeV collected in RHIC Run 14 by the STAR detector. First, suitable events were selected and cuts on charged tracks were applied. Subsequently the study of data quality assurance, response of the BEMC

and its time stability was performed. Hot towers which are towers with excessive energy deposit were excluded from the jet analysis to avoid jet reconstruction with abnormal high energy. Then the sequential recombination algorithm anti-k_T was applied on data as a function of the centrality as well as the resolution parameter R and p_T cuts on the leading parton of the jet to create uncorrected jet spectra. This was followed by background subtraction, the study of its influence on jet spectra and the study of jet area cut.

The analysis then continues by several subsequent procedures which lead to the obtaining of true jet spectra. The next step is the computation of δp_T which is the difference in transverse momentum between reconstructed and simulated jet embedded to real event: $\delta p_T = p_{T,jet}^{corr} - p_{T,jet}^{emb}$. Embedding of single particles with defined p_T into real events helps to obtain the response matrix which describes effects of fluctuating background. This matrix is then multiplied by the matrix containing information about detector effects. The used detector matrix is valid for Run 11, but we assume that performance of the TPC in Run 14 is the same. The final response matrix gives the probability to measure the true value of jet momentum. After that, the Bayesian unfolding of measured spectra corrected only to mean background energy takes place. Finally unfolded charged jet spectra for central and peripheral collisions with the resolution parameter $R = 0.2, 0.3, 0.4$ and cut on $p_T^{lead.h} \geq 5, 6, 7$ GeV/c of the leading hadron in jet are presented in Section 4.6 with the first estimate of systematic uncertainties originating from the uncertainty in prior distributions used in the unfolding procedure.

The presented results of unfolded jet spectra in Au+Au collisions are only the first step in a long and complex analysis procedure which is far beyond the scope of a diploma thesis and which requires a detailed understanding of many sources of systematic uncertainties. I will continue with the analysis described in this thesis during my Ph.D. study. The main object of the analysis in the future will be reconstruction and thorough correction of full and charged jets spectra in Run 14 for background and detector effects. This will result in computation of the nuclear modification factors R_{AA} and R_{CP} of charged and fully reconstructed jets and our results will be compared with several theoretical models. Further analysis will require more detailed studies on detector efficiencies and systematics errors. One of the first step will be performing the study of TPC tracking efficiency and the efficiency of the BEMC in Run 14 to obtain real response matrix of detectors. Unfolding procedure will be optimized and performed again utilizing two unfolding methods: the Bayesian and SVD. The analysis also requires detailed study of influence of the HFT in tracking and optimization of track cuts in order to find out the source of the difference between primary and global tracks. For full jet it will be also necessary to perform the study of mean background energy density and the most correct method and value of the hadronic correction parameter to avoid double counting of tracks in calorimeter towers. Finally analysis will conclude with the proper determination and reduction of all relevant sources of systematic uncertainties, for example tracking efficiency, tracks cuts, correction for v_2, ρ calculation, hadron ratios, fragmentation models, and jet energy scale.

Bibliography

[1] K. A. Olive, et al. (Particle Data Group). Review of Particle Physics. Chin. Phys. C 38 (2014) 090001. doi:10.1088/1674-1137/38/9/090001.

[2] K. Yagi et al., *Quark-gluon plasma*, Cambridge University Press, 2005.

[3] J. Adams *et al.* [STAR Collaboration], Experimental and theoretical challenges in the search for the quark gluon plasma: The STAR Collaboration's critical assessment of the evidence from RHIC collisions, Nucl. Phys. A **757** (2005) 102 doi:10.1016/j.nuclphysa.2005.03.085 [nucl-ex/0501009].

[4] The Phases of QCD, http://www.bnl.gov/today/body_pics/2010/07/phases-of-qcd-350px.jpg [online 28.3.2017]

[5] Sarkar, Satz, Sinha, *The Physics of the Quark-Gluon Plasma*, Springer, 2009

[6] C. Nonaka and M. Asakawa, Modeling a Realistic Dynamical Model for High Energy Heavy Ion Collisions, PTEP **2012** (2012) 01A208 [arXiv:1204.4795 [nucl-th]].

[7] R. Stock, Relativistic Nucleus-Nucleus Collisions and the QCD Matter Phase Diagram, arXiv: 0807.1610v1 (2008).

[8] M. Kliemant, R. Sahoo, T. Schuster and R. Stock, Global Properties of Nucleus-Nucleus Collisions, Lect. Notes Phys. **785** (2010) 23 [arXiv:0809.2482 [nucl-ex]].

[9] M. L. Miller, K. Reygers, S. J. Sanders and P. Steinberg, Glauber modeling in high energy nuclear collisions, Ann. Rev. Nucl. Part. Sci. **57** (2007) 205 [nucl-ex/0701025].

[10] J. Adam *et al.* [ALICE Collaboration], Measurement of charged jet production cross sections and nuclear modification in p-Pb collisions at $\sqrt{s_{NN}} = 5.02$ TeV, arXiv:1503.00681.

[11] M. Shao [STAR Collaboration], Cronin effect at RHIC, AIP Conf. Proc. **828** (2006) 49.

[12] J. Adams *et al.* [STAR Collaboration], Evidence from d + Au measurements for final state suppression of high p(T) hadrons in Au+Au collisions at RHIC, Phys. Rev. Lett. **91** (2003) 072304 [nucl-ex/0306024].

[13] J. Adam *et al.* [ALICE Collaboration], Centrality dependence of the nuclear modification factor of charged pions, kaons, and protons in Pb-Pb collisions at $\sqrt{s_{\mathrm{NN}}}$ = 2.76 TeV, Phys. Rev. C **93** (2016) no.3, 034913 doi:10.1103/PhysRevC.93.034913 [arXiv:1506.07287 [nucl-ex]].

[14] B. Abelev *et al.* [ALICE Collaboration], Measurement of charged jet suppression in Pb-Pb collisions at $\sqrt{s_{NN}}$ = 2.76 TeV, JHEP **1403** (2014) 013 doi:10.1007/JHEP03(2014)013 [arXiv:1311.0633 [nucl-ex]].

[15] Probing the perfect liquid with the star grid. http://www.interactions.org/sgtw/2006/1025/star_grid_more.html, 2001. [online 2.4.2017]

[16] K. Redlich and A. Tounsi, Strangeness enhancement in heavy ion collisions, hep-ph/0105201.

[17] T. Matsui and H. Satz, J/ψ Suppression by Quark-Gluon Plasma Formation, Phys. Lett. B 178, 416 (1986).

[18] C. Y. Wong, Introduction to high-energy heavy ion collisions, Singapore, Singapore: World Scientific (1994) 516 p

[19] A. Andronic, P. Braun-Munzinger, K. Redlich and J. Stachel, Statistical hadronization of charm in heavy ion collisions at SPS, RHIC and LHC, Phys. Lett. B 571, 36 (2003)

[20] G. Odyniec, The RHIC Beam Energy Scan program in STAR and what's next ..., J. Phys. Conf. Ser. **455** (2013) 012037.

[21] D. Barton *et al.* [BNL], Electron Beam Ion Source Pre-Injector Project, Conceptual Design Report, https://www.bnl.gov/cad/accelerator/docs/pdf/EBISDesignReportl.pdf [online 24.3.2017]

[22] K. Kajimoto, A Large Area Time of Flight Detector for the STAR Experiment at RHIC, Ph.D thesis; U. of Texas at Austin (2009).

[23] BRAHMS experiment, http://www4.rcf.bnl.gov/brahms/WWW/overview.html [online 27.4.2017]

[24] A. Accardi *et al.*, Electron Ion Collider: The Next QCD Frontier : Understanding the glue that binds us all, Eur. Phys. J. A **52** (2016) no.9, 268 doi:10.1140/epja/i2016-16268-9 [arXiv:1212.1701 [nucl-ex]].

[25] M. J. Tannenbaum, Highlights from BNL-RHIC, Subnucl. Ser. **50** (2014) 347 [arXiv:1302.1833 [nucl-ex]].

[26] K. H. Ackermann *et al.* [STAR Collaboration], STAR detector overview, Nucl. Instrum. Meth. A **499** (2003) 624.

[27] O. Rusňáková, Measurements of non-photonic electrons in STAR, Hot Quarks 2014 presentation, 2014

[28] M. Anderson, J. Berkovitz, W. Betts et.al, The STAR Time Projection Chamber: A Unique Tool for Studying High Multiplicity Events at RHIC, 2003 arXiv:nucl-ex/0301015v1

[29] M. Shao, O. Y. Barannikova, X. Dong, Y. Fisyak, L. Ruan, P. Sorensen and Z. Xu, Extensive particle identification with TPC and TOF at the STAR experiment, Nucl. Instrum. Meth. A **558** (2006) 419 [nucl-ex/0505026].

[30] M. Beddo *et al.* [STAR Collaboration], The STAR barrel electromagnetic calorimeter, Nucl. Instrum. Meth. A **499** (2003) 725.

[31] C. Yang *et al.*, Calibration and performance of the STAR Muon Telescope Detector using cosmic rays, Nucl. Instrum. Meth. A **762** (2014) 1 [arXiv:1402.1078 [physics.ins-det]].

[32] A Brief Introduction to the STAR Heavy Flavor Tracker http://rnc.lbl.gov/ jhthomas/public/HeavyFlavorTracker/ [online 12.3.2017]

[33] F.S. Bieser et al, The STAR Trigger, https://www.star.bnl.gov/public/tpc/ NimPapers/trigger/trigger_nim.pdf [online 13.3.2017]

[34] Matteo Cacciari and Gavin P. Salam. Jet clustering in particle physics, via a dynamic nearest neighbour graph implemented with CGAL. 2006 http://www.lpthe.jussieu.fr/ salam/repository/docs/kt-cgta-v2.pdf [online 8.3.2017]

[35] D. d'Enterria, Jet quenching, arXiv:0902.2011v2, 2009

[36] X. N. Wang, Why the observed jet quenching at RHIC is due to parton energy loss, Phys. Lett. B **579** (2004) 299 [nucl-th/0307036]. alebo

[37] G. Aad et al. (ATLAS Collaboration), Observation of a Centrality Dependent Dijet Asymmetry in Lead-Lead Collisions at $\sqrt{s_{NN}} = 2.76$ TeV with the ATLAS Detector at the LHC Phys. Rev. Lett. 105

[38] Jet quenching, http://www.ellipsix.net/uploads/_9tb/atlas-jetquenching.png [online 28.3.2017]

[39] G. C. Blazey et al., Run II jet physics, hep-ex/0005012

[40] E. Bruna, ALICE/ATLAS/CMS Production and quenching of heavy flavours: pp, pA, AA comparisons" presentation on BEAUTY 2013.

[41] M. Cacciari and G. P. Salam, Dispelling the N^3 myth for the k_t jet-finder, Phys. Lett. B **641** (2006) 57 [hep-ph/0512210].

[42] G. P. Salam and G. Soyez, A Practical Seedless Infrared-Safe Cone jet algorithm, JHEP **0705** (2007) 086 [arXiv:0704.0292 [hep-ph]].

[43] M. Cacciari, G. P. Salam and G. Soyez, The Anti-k(t) jet clustering algorithm, JHEP **0804** (2008) 063 [arXiv:0802.1189 [hep-ph]].

[44] G. P. Salam, Towards Jetography, Eur. Phys. J. C **67** (2010) 637 [arXiv:0906.1833 [hep-ph]].

[45] M. Cacciari, G. P. Salam and G. Soyez, The Catchment Area of Jets, JHEP **0804** (2008) 005 [arXiv:0802.1188 [hep-ph]].

[46] M. Cacciari, G. P. Salam and G. Soyez, FastJet user manual, Eur. Phys. J. C **72** (2012) 1896 [arXiv:1111.6097 [hep-ph]].

[47] H. Caines [STAR Collaboration], Jet and Underlying Event Measurements in P+P Collisions at RHIC, Int. J. Mod. Phys. E **20** (2011) 1578 [arXiv:1011.4614 [nucl-ex]].

[48] G. Soyez, Jet areas as a tool for background subtraction, arXiv:0905.2851 [hep-ph].

[49] M. Ploskon [STAR Collaboration], Inclusive cross section and correlations of fully reconstructed jets in $\sqrt{s_{NN}} = 200$ GEV Au+Au and p+p collisions, Nucl. Phys. A **830** (2009) 255C [arXiv:0908.1799 [nucl-ex]].

[50] J. Adam *et al.* [ALICE Collaboration], Measurement of jet quenching with semi-inclusive hadron-jet distributions in central Pb-Pb collisions at $\sqrt{\mathbf{s_{NN}}} = 2.76$ TeV, arXiv:1506.03984 [nucl-ex].

[51] P. M. Jacobs *et al.* [STAR Collaboration], Measurements of jet quenching with semi-inclusive charged jet distributions in $Au + Au$ collisions at $\sqrt{s_{NN}}$=200 GeV, arXiv:1512.08784 [nucl-ex].

[52] J. Rusňák [STAR Collaboration], Charged jet reconstruction in Au+Au collisions at $\sqrt{s_{NN}} = 200$ GeV at RHIC, arXiv:1412.2111 [hep-ex].

[53] J. Adam *et al.* [ALICE Collaboration], Phys. Lett. B **746** (2015) 1 doi:10.1016/j.physletb.2015.04.039 [arXiv:1502.01689 [nucl-ex]].

[54] J. Rusňák [STAR Collaboration], private communication.

[55] B. Abelev *et al.* [ALICE Collaboration], Measurement of Event Background Fluctuations for Charged Particle Jet Reconstruction in Pb-Pb collisions at $\sqrt{s_{NN}} = 2.76$ TeV, JHEP **1203** (2012) 053 [arXiv:1201.2423 [hep-ex]].

[56] G. D'Agostini, Improved iterative Bayesian unfolding, arXiv:1010.0632

[57] A. Hocker and V. Kartvelishvili, SVD approach to data unfolding, Nucl. Instrum. Meth. A **372** (1996) 469 doi:10.1016/0168-9002(95)01478-0 [hep-ph/9509307].

[58] Tim Adye, in Proceedings of the PHYSTAT 2011 Workshop on Statistical Issues Related to Discovery Claims in Search Experiments and Unfolding, CERN, Geneva, Switzerland, 17-20 January 2011, edited by H.B. Prosper and L. Lyons, CERN-2011-006, pp. 313-318.